

Sebastian Haugland Moss

Remote Sensing Data and Hydraulic Modelling of Nea

Master's thesis in Civil and Environmental Engineering

Supervisor: Knut Alfredsen

June 2019

Sebastian Haugland Moss

Remote Sensing Data and Hydraulic Modelling of Nea

Master's thesis in Civil and Environmental Engineering
Supervisor: Knut Alfredsen
June 2019

Norwegian University of Science and Technology
Faculty of Engineering
Department of Civil and Environmental Engineering



MASTEROPPGÅVE I VASSDRAGSTEKNIKK

Student: Sebastian Haugland Moss

Tittel: Fjernmålte data og hydraulisk modellering av Nea

1. Bakgrunn

I forskningssenteret CEDREN vart det utvikla ei handbok for miljødesign i regulerte laksevassdrag so mi dag er brukt som grunnlag for analyse og tiltak i samband med miljøvurderingar i regulerte vassdrag. Dette arbeidet vert vidareført i senteret HydroCen med mål om å utvide prinsippet med miljødesign til andre artar og innlandsvassdrag. I samband med dette er det sett i gang eit arbeid som skal bidra med forskning for å nå målet om ein utvida metode for miljødesign òg i vassdrag med andre artar enn laks. Eit av verkemidla som kan vurderast i samband med miljødesign er tiltak i vassdraget med tanke på utbetring av habitat og lette vandring av fisk.

Nea er elvestrekninga frå Vessingsjøen til Selbusjøen, og er regulert gjennom fleire magasin og kraftverk. Strekninga frå Heggsetdammen til utløpet av nedre Nea kraftverk har fråført vatn og er sterkt påverka av reguleringa. I samband at elva vart regulert vart det bygd ei rekke med tersklar på denne strekninga. I dag er det fleire spørsmål rundt funksjonen til tersklane og Statkraft og forskarar i HydroCen har starta eit arbeid for å vurdere dette som ein del av prosjektet for å utvide miljødesignmetoda.

Denne hovudoppgåva er hovudsakleg knytt til vurderinga av tiltak rundt tersklane i Nea, og er i hovudsak retta mot bruk av fjernmålte data og hydraulisk modellering.

2. Hovudpunkt i arbeidet

Arbeidet er eit sjølvstendig arbeid der kandidaten skal planlegge, førebu og gjennomføre det som er innhaldet i oppgåva. Arbeidet bygger på prosjektoppgåva som vart gjennomført i 2018.

Oppgåva skal innehalde, men ikkje nødvendigvis vere avgrensa til spørsmåla som er lista opp her:

- 1 Gjere ei vurdering av data som er tilgjengelege for Nea, og då spesielt data frå grøn LiDAR samla inn sommaren 2018, med tanke på å sette opp ein hydraulisk modell for elvestrekninga. Finst det grunnlag for å modellere heile strekninga (1D, 2D) eller må vi konsentrere arbeidet til spesielle område i elva.
- 2 Med utgangspunkt i funn frå 1) skal det etablerast ein eller fleire modellar for strekninga.
 - a. Det skal lagast ein 2D hydraulisk modell for strekninga med «elv i elva» som vart målt inn med drone i prosjektoppgåva hausten 2018. Korleis ein koplar saman dronedata med LiDAR skal vere ei vurdering i dette arbeidet.
 - b. Om mogleg skal det lagast ein modell for strekninga frå Heggsetdammen til Selbusjøen.

- c. Det skal lagast ein eller fleire modellar for viktige tersklar på strekninga med tanke på å simulere kva effekt fjerning eller justering av tersklane har på strømningsstilhøve og habitat i elva.
- 3 Det skal gjerast ei vurdering om ytterlegare feltdata er naudsynt, og i tilfelle samle inn desse sein vinteren eller våren 2019.
- 4 Som ein del av vurderinga av bruk av fjernmåling som datainnsamling skal det gjerast droneinnmåling av ei strekning i Sokna vinteren 2019 med tanke på iskartlegging. Med utgangspunkt i data frå drona, skal DEM og ortofotomosaikkar lagast.
- 5 Rapportering av resultat frå prosjektet i form av ei masteroppgåve. I samband med rapporteringa er det viktig å levere alle modellar og data digitalt med tanke på vidareføring av arbeidet i prosjektet.

3. Rettleiing

Professor Knut Alfredsen vil vere hovudrettleiar for oppgåva. Stipendiat Håkon Sundt vil fungere som rettleiar for arbeidet i Nea.

Diskusjon med og bidrag frå kollegaer og medarbeidarar på NTNU, SINTEF og eventuelt andre er tilrådd. Bidrag som nyttast i oppgåva skal alltid refererast til på rett vis.

Arbeidet som vert gjort i samband med oppgåva er ein del av eit utdanningsløp og student og rettleiarar har fridom til å ta inn avgrensingar og føresetnader som kan oppfattast som urealistiske eller uvanlege i ein kommersiell samanheng.

4. Rapportformat, referansar og erklæring

Oppgåva skal skrivast i eit tekstbehandlingsprogram slik at figurar, tabellar, foto osv. får god rapportkvalitet. Rapporten skal innehalde eit samandrag, ei innhaldsliste, ei litteraturliste og opplysningar om andre relevante referansar og kjelder. Oppgåva skal leverast i B5-format som .pdf i Inspira/DAIM og trykkast i tre eksemplar som sendast direkte frå trykkeri til faglærer/institutt. Samandraget skal ikkje gå over meir enn 450 ord og skal vere eigna for elektronisk rapportering.

Kandidaten skal presentere oppgåva i slutten av semesteret. Tidspunkt for presentasjonen vil verte kunngjort seinare.

Innleveringsfrist er 11. juni 2019

Trondheim, 14. januar 2019

Knut Alfredsen
Professor
Institutt for bygg og miljøteknikk
NTNU

ABSTRACT

Access to technologies like drones and laser measurements provide new tools for obtaining accurate spatial data for mapping and analysis of river systems. Airborne Light Detection and Ranging (LiDAR) Bathymetry is a remote sensing technique for mapping underwater topography in shallow water bodies and provide detailed models of river bathymetry.

Datasets from two Airborne LiDAR Bathymetry (ALB) surveys is the foundation for a two-dimensional hydraulic model created in HEC-RAS 5.0 for the river Nea (34 km long) in Norway. The main goal of the thesis is to evaluate how proposed modifications to some of the weirs in Nea will influence hydraulic conditions in the river. The hydraulic model is created with LiDAR data surveyed in 2018 and 2019 with a bathymetric point density of 1.72 pts/m² and 7.47 pts/m², respectively.

The model is calibrated against a measured water surface in the LiDAR data. The calibration process included changing the Manning's roughness coefficient of 90 polygons with sizes ranging from 54 m² to 712,369 m². The standard deviation between simulated and measured water surface elevations is ± 8 cm, which corresponds to the accuracy of LiDAR measurements and natural fluctuations of the water.

Hydraulic modelling show that lowering small sections on nine of the weirs in Nea will reduce the water-covered area by 9.3% in the upstream weir-pools for the environmental flow in this area. The water-covered area is better maintained in simulations with higher discharges, with a 2.5% reduction seen at 10 m³/s. The average velocity in the river is maintained at lower discharges and reduced from 0.58 m/s to 0.57 m/s at 10 m³/s. Lowering sections on a weir will concentrate the flow over the weir and increase velocity in the immediate upstream areas.

The study has also evaluated drones and Structure from Motion (SfM) software as a method for mapping river ice. This included four topographic surveys of a 200-meter reach in Sokna, Norway in the period November 2018 to April 2019. The surveys provided data on the ice cover at different stages of formation and the break-up with associated ice jams. The reconstructed Digital Elevation Models (DEM) have an absolute accuracy on the centimetre-level, with the highest observed combined Root Mean Square Error (RMSE) of 7.7 cm. Through this method, data on ice thickness, spatial distribution and volume can be extracted without accessing the river ice.

SAMMENDRAG

Tilgang til teknologi som droner og lasermålinger gir nye verktøy for å tilegne seg nøyaktig geometridata for kartlegging og analyse av elvesystemer. Batymetrisk LiDAR (Light Detection and Ranging) er en fjernmålingsmetode som trenger gjennom vannoverflaten og kartlegger bunnforhold og kan brukes til å lage detaljerte terrengmodeller.

Innsamlet data fra to flyvninger med batymetrisk LiDAR er grunnlaget for en todimensjonal hydraulisk modell laget i HEC-RAS 5.0 for elven Nea (34 km lang) i Norge. Hovedmålet for denne oppgaven er å evaluere hvordan foreslåtte modifikasjoner på terskler i Nea vil påvirke hydrauliske forhold i elven. Den hydrauliske modellen er laget med LiDAR data samlet inn i 2018 og 2019 med en batymetrisk punkttetthet på henholdsvis 1.72 pkt/m² og 7.47 pkt/m².

Modellen er kalibrert mot en vannoverflate målt med LiDAR. Kalibreringsprosessen inkluderte å endre Mannings ruheffisient på 90 polygoner med varierende størrelser fra 54 m² til 712,369 m². Standardavvikene mellom simulerte og målte vannoverflatehøyder er ± 8 cm, som samsvarer med nøyaktigheten til målinger med LiDAR og naturlige variasjoner i vannet.

Hydraulisk modellering viser at å senke mindre partier på ni av tersklene i Nea vil redusere det vanndekkede arealet med 9.3% i oppstrøms terskelbasseng for en vannføring som tilsvarer pålagt minstevannføring i dette området. Det vanndekkede arealet er bedre opprettholdt i simuleringer med høyere vannføring, og viser en reduksjon på 2.5% for 10 m³/s. Den gjennomsnittlige hastigheten i elven er vedlikeholdt ved lavere vannføringer og redusert fra 0.58 m/s til 0.57 m/s ved 10 m³/s. Å senke et av parti på en terskel vil konsentrere strømmingen over dammen og øke hastigheten i de nærliggende områdene og over terskelen.

Dette studiet har også evaluert droner og Structure from Motion (SfM) programvare som en metode for å kartlegge is i elver. Arbeidet inkluderte fire topografiske undersøkelser av en 200 meter strekning i Sokna, Norge i perioden November 2018 til April 2019. Undersøkelsene ble brukt til å kartlegge utviklingen av isdekket ved ulike stadier gjennom vinteren. De rekonstruerte høydemodellene fra innsamlet data har en absolutt nøyaktighet på centimeternivå, med en høyest observert RMSE (Root Mean Square Average) på 7.7 cm. Ved bruk av denne metoden kan informasjon om isens tykkelse, overflateareal og volum innhentes, og krever ikke tilgang til isen for å gjennomføres.

PREFACE

This thesis is the culmination of a Master's Degree in Hydraulic Engineering at the Norwegian University of Science and Technology. The work has been supervised by Professor Knut Alfredsen and Håkon Sundt. The study is linked to HydroCen's project 4.3 and Håkon Sundt's research on digital tools for mapping and analyses of river systems.

I have taken great pleasure working on this thesis and the interest I have seen coming from scientific communities and experts in the field has been truly motivating. First, I would like to thank my supervisor Knut Alfredsen. You have facilitated all the field work in this study and provided useful guidance along the way.

I would also like to thank my co-supervisor Håkon Sundt. Your experience in handling comprehensive LiDAR datasets and your local knowledge of the study area have improved the hydraulic model created in this study.

I declare that the work I have submitted is my own and that received information or help has been acknowledged or referenced.

TABLE OF CONTENTS

Abstract	iii
Sammendrag	v
Preface	vii
table of contents	ix
List of Figures	xi
List of tables	xv
Abbreviations	xvii
1 Introduction	1
1.1 Background	1
1.2 Objective	2
2 Remote Sensing and Hydraulic Modelling	3
2.1 Airborne LiDAR	3
2.2 UAV Photogrammetry	5
2.3 Environmental Design in Nea	6
2.4 River ice	12
3 Material and Methods.....	14
3.1 Study Sites.....	14
3.2 LiDAR Data	17
3.3 UAV Photogrammetry	24
3.4 Ground Surveying	26
3.5 Hydraulic Modelling	27
3.6 Mapping River Ice.....	32
4 Results	35
4.1 LiDAR Data Assessment	35
4.2 Hydraulic Modeling of Nea.....	39
4.3 Mapping River Ice in Sokna.....	50

5	Discussion	55
5.1	LiDAR Data Assessment	55
5.2	Hydraulic Modelling of Nea	56
5.3	Mapping River Ice.....	60
6	Conclusion.....	61
	References	63
	Appendices	65

LIST OF FIGURES

Figure 1: The three channels in the Optech Titan sensor.....	4
Figure 2: Map showing the regulation in Nea.....	8
Figure 3: Recorded discharge at the gauge station Kulset bru.....	8
Figure 4: Recorded water level at the gauge station Kulset bru.....	9
Figure 5: Visualization of proposed measure on a weir in Nea..	10
Figure 6: Map of the 34 km long study area in Nea.....	15
Figure 7: Map of the studied area in Sokna and surrounding topography.	16
Figure 8: Weather statistics for Sokna the last year.	17
Figure 9: Terrain model after manipulating LAS point heights in ArcMap.	20
Figure 10: Terrain model after interpolating between two cross sections in HEC-RAS.	21
Figure 11: Terrain model after applying a surface constraint.	22
Figure 12: Calibration raster.	31
Figure 13: The two areas of interest marked in Figure 8.	32
Figure 14: Orthophotomosaics and DEM reconstructed from for Sokna.	33
Figure 15: Elevation residuals for compared LiDAR derived DEM	36
Figure 16: Measured Z values of check points in group 3 and 4	37
Figure 17: Measured Z values of check points in group 2 and 5.	38
Figure 18: Measured Z values of check points in group 1 and 6	38
Figure 19: Measured Z values of check points in group 7	38
Figure 20: Distribution of velocities for a flow of 1.5 m ³ /s.	43
Figure 21: Distribution of velocities for a flow of 5 m ³ /s.	43
Figure 22: Distribution of velocities for a flow of 10 m ³ /s.	44
Figure 23: Distribution of depth for a flow of 1.5 m ³ /s.....	45
Figure 24: Distribution of depth for a flow of 5 m ³ /s.....	46
Figure 25: Distribution of depth for a flow of 10 m ³ /s.....	46

Figure 26: Orthomosaic and DEM from UAV for the artificial channel.	47
Figure 27: Elevation differences (m) comparing the reference and UAV.	48
Figure 28: Water depth (m) from simulations in artificial channel on UAV.	49
Figure 29: Water depth (m) from simulations in artificial channel on LiDAR.	50
Figure 30: Orthophotos from the four UAV surveys in Sokna	51
Figure 31: Orthophoto from the March survey data showing three cross sections.	52
Figure 32: Profile graphs for cross-section C-C'.	53
Figure 33: Profile graph for cross-section C-C' from the national DTM.	53
Figure 34: Map of Nea showing the locations of weir 1-20.	i
Figure 35: Map of Nea showing the locations of weir 21-32.	ii
Figure 36: Terrain model with weir measures for weir 6 and weir 9.	iii
Figure 37: Terrain model with weir measures for weir 21 and weir 22.	iii
Figure 38: Terrain model with weir measures for weir 23.	iv
Figure 39: Terrain model with weir measures for weir 24.	iv
Figure 40: Terrain model with weir measures for weir 27 and weir 38	v
Figure 41: Terrain model with weir measures for weir 29 and weir 32	v
Figure 42: LiDAR point coverage on weir 6.	vi
Figure 43: LiDAR point coverage on weir 9.	vii
Figure 44: LiDAR point coverage on weir 22.	viii
Figure 45: LiDAR point coverage on weir 23.	ix
Figure 46: LiDAR point coverage on weir 24.	x
Figure 47: LiDAR point coverage on weir 27.	xi
Figure 48: LiDAR point coverage on weir 28.	xii
Figure 49: LiDAR point coverage on weir 29.	xiii
Figure 50: LiDAR point coverage on weir 32.	xiv
Figure 51: Map of the modeled reach in Nea	xv
Figure 52: Check point locations in area 1.	xvi

Figure 53: Check point locations in area 2.....	xvii
Figure 54: Check point locations in area 3.....	xviii
Figure 55: Check point locations in area 4.....	xix
Figure 56: Map of all the weirs modelled with measures and the upstream weir-reservoir. .	xxii
Figure 57: Simulation results as depth map for weir 32 at 1.5 m ³ /s.	xxiii
Figure 58: Simulation results as depth map for weir 32 at 5 m ³ /s.	xxiii
Figure 59: Simulation results as depth map for weir 32 at 10 m ³ /s.	xxiv
Figure 60: Simulation results as velocity map for weir 32 at 1.5 m ³ /s.	xxiv
Figure 61: Simulation results as velocity map for weir 32 at 5 m ³ /s.	xxv
Figure 62: Simulation results as velocity map for weir 32 at 10 m ³ /s.	xxv
Figure 63: Simulation results as depth map for weir 27, 28 and 29 at 1.5 m ³ /s.....	xxvi
Figure 64: Simulation results as depth map for weir 27, 28 and 29 at 5 m ³ /s.....	xxvi
Figure 65: Simulation results as depth map for weir 27, 28 and 29 at 10 m ³ /s.....	xxvii
Figure 66: Simulation results as velocity map for weir 27, 28 and 29 at 1.5 m ³ /s.....	xxvii
Figure 67: Simulation results as velocity map for weir 27, 28 and 29 at 5 m ³ /s.....	xxviii
Figure 68: Simulation results as velocity map for weir 27, 28 and 29 at 10 m ³ /s.....	xxviii
Figure 69: Simulation results as depth map for weir 23 and 24 at 1.5 m ³ /s.....	xxix
Figure 70: Simulation results as depth map for weir 23 and 24 at 5 m ³ /s.....	xxx
Figure 71: Simulation results as depth map for weir 23 and 24 at 10 m ³ /s.....	xxxi
Figure 72: Simulation results as depth map for weir 21 and 22 at 1.5 m ³ /s.....	xxxii
Figure 73: Simulation results as depth map for weir 21 and 22 at 5 m ³ /s.....	xxxii
Figure 74: Simulation results as depth map for weir 21 and 22 at 10 m ³ /s.....	xxxiii
Figure 75: Simulation results as velocity map for weir 21 and 22 at 1.5 m ³ /s.....	xxxiii
Figure 76: Simulation results as velocity map for weir 21 and 22 at 5 m ³ /s.....	xxxiv
Figure 77: Simulation results as velocity map for weir 21 and 22 at 10 m ³ /s.....	xxxiv
Figure 78: Simulation results as depth map for weir 6 and 9 at 1.5 m ³ /s.....	xxxv
Figure 79: Simulation results as depth map for weir 6 and 9 at 5 m ³ /s.....	xxxvi

Figure 80: Simulation results as depth map for weir 6 and 9 at 10 m ³ /s.....	xxxvii
Figure 81: Simulation results as velocity map weir 6 and 9 at 1.5 m ³ /s.	xxxviii
Figure 82: Simulation results as velocity map weir 6 and 9 at 5 m ³ /s.	xxxix
Figure 83: Simulation results as velocity map for weir 6 and 9 at 10 m ³ /s.....	xl
Figure 84: Profile graphs for cross-section A-A'	xlviii
Figure 85: Profile graphs for cross-section B-B'	xl ix
Figure 86: Profile graphs for cross-section C-C'	l

LIST OF TABLES

Table 1: List of proposed measures on weirs in lower Nea	11
Table 2: Point spacing and point density in the channel area	35
Table 3: Vertical accuracy of LiDAR (check points under water and on ground).	36
Table 4: Vertical accuracy of LiDAR (check points on grass and asphalt).	37
Table 5: Results from the calibration process.	39
Table 6: Water-covered area	40
Table 7: Difference in water-covered area shown as percentage increase.....	40
Table 8: The difference in water-covered area.....	41
Table 9: Average velocity (m/s) in the weir-pool upstream.....	42
Table 10: Average depth (m) in the weir-pool upstream of each weir	45
Table 11: The accuracy in models reconstructed from UAV	47
Table 12: Root mean square error of the UAV	51
Table 13: Surface area and volume of the river ice in Sokna.	52

ABBREVIATIONS

ALB	Airborne LiDAR Bathymetry
ArcGIS	GIS software suite developed by ESRI
ArcMap	GIS software in ArcGIS software suite
ASPRS	American Society of Photogrammetry & Remote Sensing
CEDREN	Centre for Environmental Design of Renewable Energy
DEM	Digital Elevation Model
DTM	Digital Terrain Model
GIS	Geographic Information System
GNSS	Global Navigation Satellite System
GPS	Global Positioning System
GUI	Graphical User Interface
HEC-RAS	The Hydrologic Engineering Center – River Analysis System
HydroCen	Norwegian Research Centre for Hydropower-Technology
LAS	File format for transferring LiDAR data standardized by ASPRS
LiDAR	Light Detection and Ranging
N-CAA	The Norwegian Civil Aviation Authority
NTNU	Norwegian University of Technology and Science
NVE	Norwegian Water Resource and Energy Directorate
RTK	Real-Time Kinematic
SfM	Structure from Motion
UAV	Unmanned Aerial Vehicle
USACE	US Army Corps of Engineers

1 INTRODUCTION

1.1 Background

The natural topography in Norway makes hydro power production a viable option to meet the demand in the power market. Nearly half of Europe's water storage capacity is in Norway, which has allowed us to build the foundation of our electricity demands around hydro power production. Most of the main sites suitable for hydropower production in Norway have already been developed, shifting the focus to small hydropower projects (< 10 MW). NVE (Norwegian Water Resource and Energy Directorate) investigated the small hydropower potential and found that 25 TWh can be realised with an investment cost less than 3 NOK/kWh (NVE, 2006). Developing new hydro power projects in rivers and streams can change the environmental conditions for those that live in and use the water. The experience and knowledge gained over many years of hydropower development in Norway are now being used to mitigate damages to the river ecology through environmental design.

Rivers regulated by hydro power production has its natural flow regimes disrupted caused by the manoeuvring of the power production. Frequent changes in the rivers can change the environment in and around the river, affecting those who live in- and use the water resource. The environmental design concepts explained by Forseth & Harby (2013) for regulated salmonoid rivers is the foundation we use to mitigate damages to river ecology from hydropower production today. Researchers in HydroCen (Norwegian Research Centre for Hydropower-Technology) now aims to expand existing environmental design concepts to new species with innovative technology and digital tools for mapping and analysis of river systems.

Weirs are often built in regulated rivers to reduce the effect hydropeaking have on the river hydromorphology. In the 1970s it was common to construct weirs in regulated rivers to maintain water-covered areas for aesthetic reasons. Today there is a shift towards improving the conditions for biological communities and the general biodiversity and constructed weirs are being questioned as to their effect on environmental conditions.

River ice is a critical part in the cryosphere that can change the river geomorphology, ecology, hydraulic conditions and winter water supply. River ice in regulated rivers can damage critical infrastructure such as roads, dams and intakes, and reduce or cut off available water for power production. Accurate data on river ice is important to understand the river ice processes and the

effect it can have on other systems. Traditional methods for monitoring and mapping river ice requires accessing the ice for ground-based measurements or low-resolution satellite images. Ground-based field work on ice can be dangerous and time-consuming, and satellite images is not always available or does not provide enough detail on smaller river systems, making these methods ineffective. Topographic surveys carried out with drones equipped with high quality cameras coupled with Structure from Motion (SfM) software provides a new approach for mapping ice formations in smaller rivers.

1.2 Objective

This thesis will use remote sensing data from surveys using Light Detection and Ranging (LiDAR) and Unmanned Aerial Vehicle to reconstruct the topography and bathymetry of two rivers in Norway. In Nea, Digital Elevation Models (DEM) reconstructed from LiDAR data and UAV acquired images is the foundation for hydraulic modelling of measures on strategic weirs in Nea. Four UAV topographic surveys in Sokna provide data on the river ice as it develops, used for mapping and analyses on formation and break-up of river ice. This study will evaluate the available bathymetric data collected by Airborne LiDAR Bathymetry (ALB) in Nea for hydraulic modelling of environmental design.

- Evaluate available remote sensing data for Nea in 2018 and 2019 for hydraulic modelling.
- Reconstruct river bathymetry from data available in Nea.
- Hydraulic modelling based remote sensing data to investigate the hydraulic effects of modifications on strategic weirs in River Nea.
- Create a hydraulic model in HEC-RAS of a 500-meter artificial channel in Nea.
- Obtain data with UAV topographic surveys for mapping river ice in Sokna by reconstructing DEM and orthomosaic from the optical remote sensing data with Structure from Motion software.

2 REMOTE SENSING AND HYDRAULIC MODELLING

2.1 Airborne LiDAR

Airborne laserscanning, often referred to as LiDAR (Light Detection and Ranging) is a remote sensing method capable of mapping large areas by plane or helicopter. The data is collected by a LiDAR sensor mounted under the aircraft that emit pulses of light towards the ground. When the pulse reaches the surface beneath (e.g. ground, vegetation or building) it reflects back to the aircraft where the sensor detects the returning beam. The sensor measures the time between emitting the pulse and the reflected beam returning to the aircraft. Knowing the beam's travel time makes it possible to convert time into distance. Close scattered measurements of the distance to the ground while maintaining a relative even flying altitude throughout the survey, makes it possible to calculate elevation difference on the surface. The aircraft is equipped with Global Navigation Satellite System (GNSS) used to georeference the points measured on the surface with a precision on the decimeter level. A more accurate approach to georeference LiDAR data is to include Ground Control Points (GCP) from independent sources, typically measured with high-accuracy GNSS equipment on the ground. LiDAR point-clouds are typically delivered with a point density of 20-50 pts/m². Surveying conditions and data processing by the surveyor are important to obtain quality LiDAR data. High-resolution terrain models can be reconstructed from LiDAR point-point clouds, creating a model of the current conditions in the survey area.

Airborne LiDAR Bathymetry (ALB), or 'green' LiDAR, is a method for mapping underwater topography in rivers, lakes and reservoirs. Bathymetric data is useful when studying hydraulic and environmental processes, sediment transport and flood risk. ALB is a method of active remote sensing for mapping underwater topography in shallow water (< 10 m) in addition to the surrounding terrain. In contrast to the traditional over-water LiDAR sensor's single Near-Infrared (NIR) light beam, the green LiDAR uses a multispectral sensor emitting beams of light with different wavelengths. This includes a NIR channel for ground and water-surface detection, as well as a beam in the visible green light spectrum (495-570 nm). Surfaces like concrete or asphalt strongly reflect the NIR light but absorb visible green light, while green light can penetrate water-surface and reflect off the riverbed (Optech, 2015). This allows the multispectral sensor to map bathymetry with the green channel while the surface-detecting NIR

channels map the water surface and surrounding terrain. Figure 1 illustrates the three channels in a multispectral LiDAR sensor and their reflection off different surfaces.

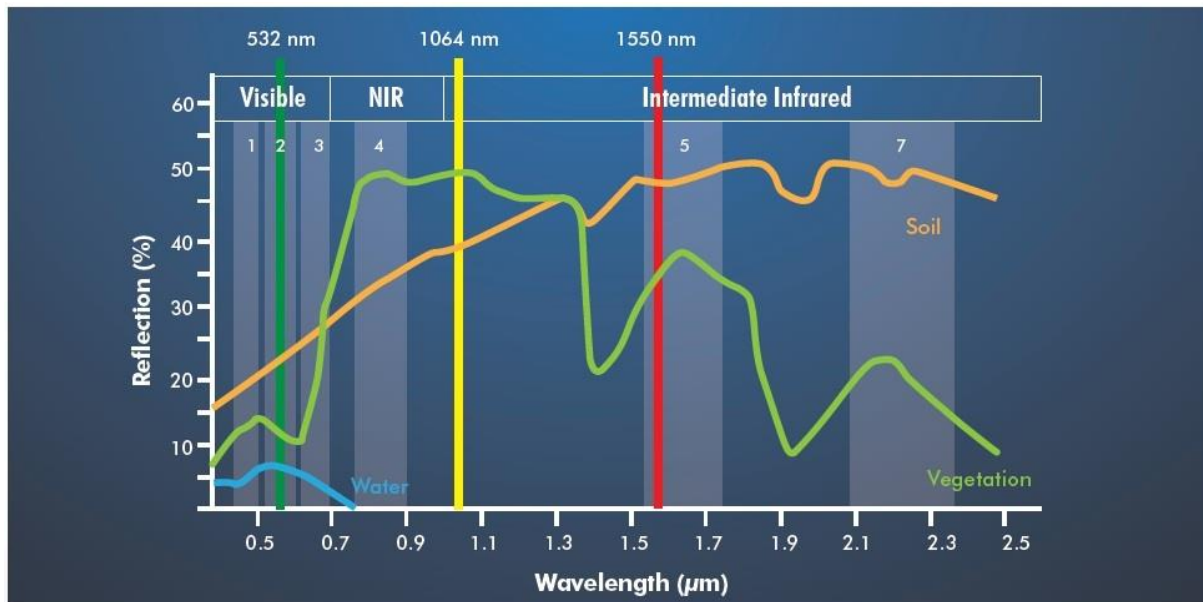


Figure 1: The three channels in the Optech Titan sensor, showing the green light and the two NIR channels. The reflection on water surface, soil and vegetation is shown as a percentage on the vertical axis (Optech, 2015).

Topo-bathymetric LiDAR operates under the same principles as traditional LiDAR on over-water surfaces. When the emitted green LiDAR beam penetrates a water surface the process gets more complex. As light moves through the water column two important processes occur. When the light reaches the water surface it will bend (refract) according to Snell's law, effectively obscuring the actual reflection point on the riverbed if not corrected for. The mitigation speed of light in water is different than in the air. To map the underwater topography corrections are made for refraction and increased travel time of light in the water.

Conditions in the water can affect the penetration depth of LiDAR pulses due to absorption or scattering of light. A study conducted by Kartverket (2014) presents dark bottom structures or dark underwater vegetation as the most influencing factor when considering penetration depth and point density. The results of their study show that their LiDAR surveys obtained an average point density of 20-40 pts/m² in shallow waters. The post-processing conducted by the supplier is an important element to the quality of the LiDAR point-cloud. The process includes removal of false echoes, correcting for the refraction of the water surface and point classification.

LiDAR data is typically delivered as a set of LAZ-files, a compressed format of the LAS-file. LAS is a format developed for fast and efficient storage and transfer of large point-clouds of LiDAR data. The format is standardized by the American Society of Photogrammetry & Remote Sensing (ASPRS) and includes the spatial location of measured points as well as the intensity of each return. All recorded data is stored as points with xyzi-values (xyz-coordinates and intensity value). LiDAR data were originally supplied in the ASCII-format. This format has weaknesses in the form of performance (require significantly more processing-power for larger sized files) as well as the inability to store additional information, like the intensity value. ASPRS states that the purpose of standardizing the LAS file format is to maintain an efficient and available file-format for both hardware and software to read and write (ASPRS, 2019)

2.2 UAV Photogrammetry

2.2.1 Operating UAV topographic survey

UAV topographic surveys are a low-cost optical remote sensing method for acquiring high-resolution aerial images of a study area. UAVs equipped with a quality camera is an increasingly seen optical remote sensing method in environmental studies including river habitat conditions, erosion and substrate studies. In the cryospheric community, the method is seen in the study of glaciers, snow accumulation and river ice. UAV surveys provide aerial images that can be processed with SfM software to reconstruct 3D surface, orthomosaics and DEM of a project area.

The Norwegian Civil Aviation Authority (N-CAA) regulates the use of UAVs through the Regulation for Civilian aircraft A 7-1 (Regulation for Unmanned Aircrafts) and the Aviation Act. N-CAA have also created a set of simple guidelines when flying UAVs without a license. The guidelines will reduce the risk of accidents occurring due to human errors and system failures, maintain privacy rights and ensure drones do not interact with air-traffic. Guidelines for drones in leisure activities is summarized as:

1. The drone should always be kept within your line of sight and operated in a mindful and considerate manner. Never fly near accident sites.
2. Never fly closer than 5 km from airports unless you have explicit clearance to do so.
3. Never fly higher than 120 meters from the ground (120 m AGL).
4. Never fly over military facilities or sporting events. Keep a distance of 150 meters to people, buildings and traffic (road, sea, air).
5. Be considerate of others privacy. Take note of the rules concerning photos and films of other people.

The UAV surveys in this study were conducted in accordance to the guidelines set by N-CAA to ensure safe operation.

2.2.2 Photogrammetric processing

Agisoft Photoscan is a 3D reconstruction software based on SfM and multi-view stereo (MVS) algorithms developed by the Russian company Agisoft LCC. Photoscan provide advanced image-based modeling solutions to reconstruct 3D surface, orthomosaic and DEM from photographs. It can process RGB, NIR, thermal and multispectral images and include tools to analyze the reconstructed model. Photogrammetric processing of images in Photoscan includes image alignment and 3D model reconstruction from point-cloud.

The general workflow to build 3D surface, DEM and orthomosaic in Photoscan includes four stages (Agisoft, 2016). The first is camera alignment, a process of identifying and matching corresponding features in photographs to generate a network of ‘tie points’ which is further processed through ‘bundle adjustment’ optimization to determine point coordinates and camera locations. The result is a sparse point cloud and a set of estimated camera positions in a local reference frame and arbitrary scale. This process is referred to as ‘direct’ bundle adjustment before including GCPs. GCPs are points with known coordinates used to convert the arbitrary scale and local reference system to real-world scales and coordinate system. (e.g., a projected UTM, easting and northing, and height). The second stage uses the estimated camera positions of each image to build a dense point. The dense point cloud can be classified in Photoscan or in other GIS applications. The third stage is building a surface from the point cloud, as a mesh or DEM. The DEM can be reconstructed with particular point classes if classified in the previous step. The last stage generates an orthophotomosaic projected on a surface (DEM or mesh model). The workflow used in this study to reconstruct DEMs and orthophotos can be seen in chapter 3.3.

2.3 Environmental Design in Nea

2.3.1 Current conditions

Nea is a river connecting Vessingsjøen to Selbusjøen, originating in the mountains of Sylane it drains mountainous- and forested areas in Tydal and Selbu south of Trondheim. The river is regulated through several magazines and power plants and is probably the most important river for recruitment of brown trout (*Salmo trutta*) to Lake Selbusjøen (Bjølstad, O.K.H, 2015). The lower 25 km of River Nea (see Figure 2) from Heggsetdam to the outlet of Nedre Nea in

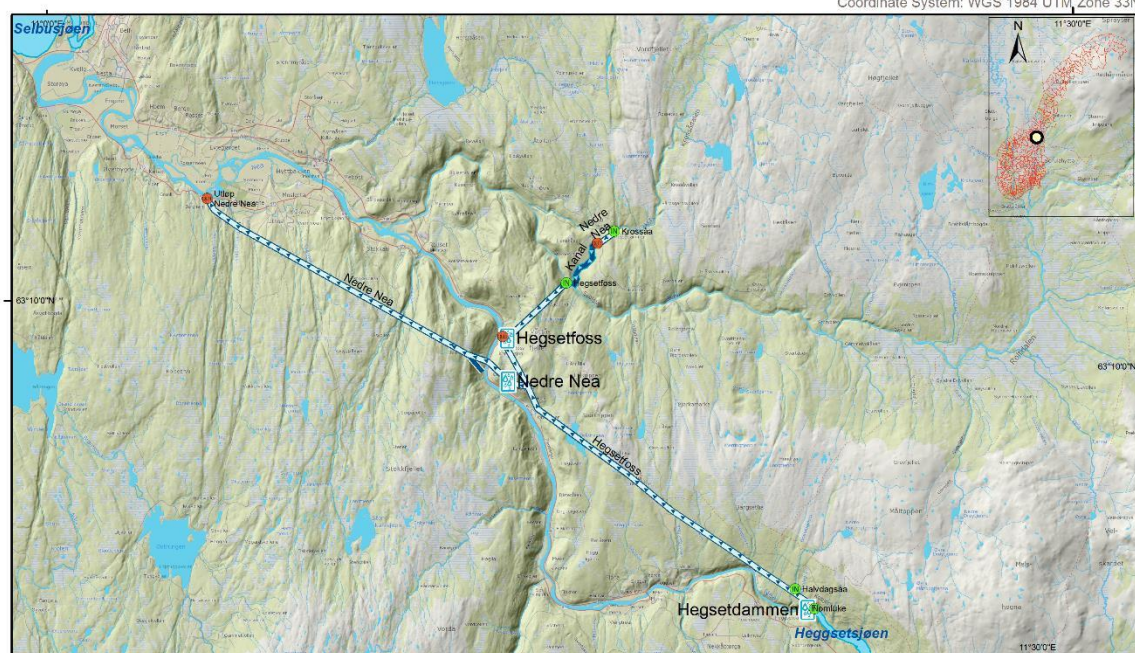
Bogstadhølen is heavily affected by regulations in River Nea and have had its flow greatly reduced. There is a minimum flow requirement of 1.5 m³/s during summer (1 May to 31 September), controlled by a gauge located at Tuset bru near Flora, 3 km downstream of Heggsetdam. However, during winter season the power company is not required to maintain a minimum flow in the river (NVE, 2006).

The constructed weirs in Nea changed the river from having long riffles and naturally occurring pools, to primarily consist of slow flowing reservoirs without any riffles between many of the weirs. This has increased the overall water-covered area in periods of low flow but has decreased the effective spawning- and habitat areas located in riffles. The weirs have created good conditions for the minnow species (*Phoxinus phoxinus*), first recorded in River Nea in 1974 (NVE, 2006). Two studies on the fish community in Nea using net and electrofishing carried out in 2003 and 2004 describes a decreasing brown trout population (Arnekleiv et al., 2006). This can be caused by a combination of reduced flow in the river and increased contest from the minnow species.

A 2013 study in Nea identified potential spawning and habitat areas for the brown trout species in Nea (Bjølstad et al., 2014). The study estimated that 27% of the area between the outlet of Nedre Nea and Heggsetdam is considered good habitat areas for brown trout. Potential spawning areas were registered in areas dominated by substrate diameters of 2-7 cm (fine gravel) and water velocity in the range of 0.2-1 m/s (moderate riffle).

2.3.2 Operations in Nea

The discharge in Nea is affected by the operations of Nedre Nea power plant. The outlet of Nedre Nea power plant is located near Bogstadhølen, as seen on the map of River Nea in Figure 2. The power plant operates with a significant start- and stop frequency during all seasons, causing frequent and fast variations in discharge and drying of river areas upstream of the outlet (Bjølstad et al., 2014). previous studies have shown that the rapidly varied flow events due to daily- and weekly operations of Nedre Nea power plant dry up areas in the river, potentially causing fish death due to stranding (Arnekleiv et al. 2006). Figure 3 and Figure 4 show the daily discharge and water levels recorded at Kulset bru in the period 1 January 1993 to 11 March 2019.



Title: Oversiktskart av reguleringene i Nea elv

0 1 2 3
km
Scale 1: 100 000

Legend

- Inntak
- Utlep
- Hydropower plant
- Tunnel
- Rør
- Sjøkt
- Kanal
- Tverslag/Andre

Figure 2: Map showing the regulation in Nea between Hegsetdam and Selbusjøen. The location of Nedre Nea power plant and Hegsetfoss power plant is shown, along with the location of their outlets.

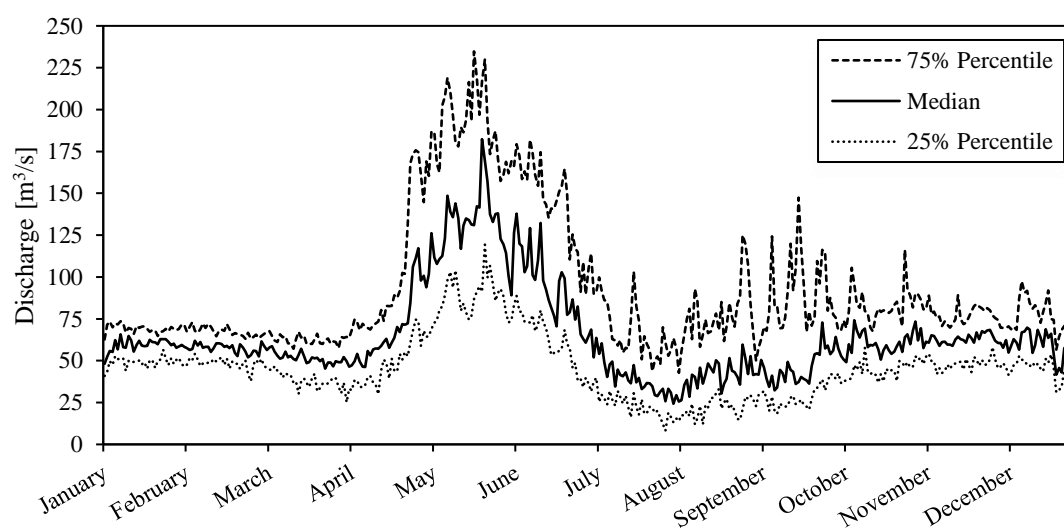


Figure 3: Recorded discharge at the gauge station Kulset bru (nr. 123.34.0). The discharge is based on daily recordings in the period from 1 January 1993 to 11 March 2019. (Data available from NVE).

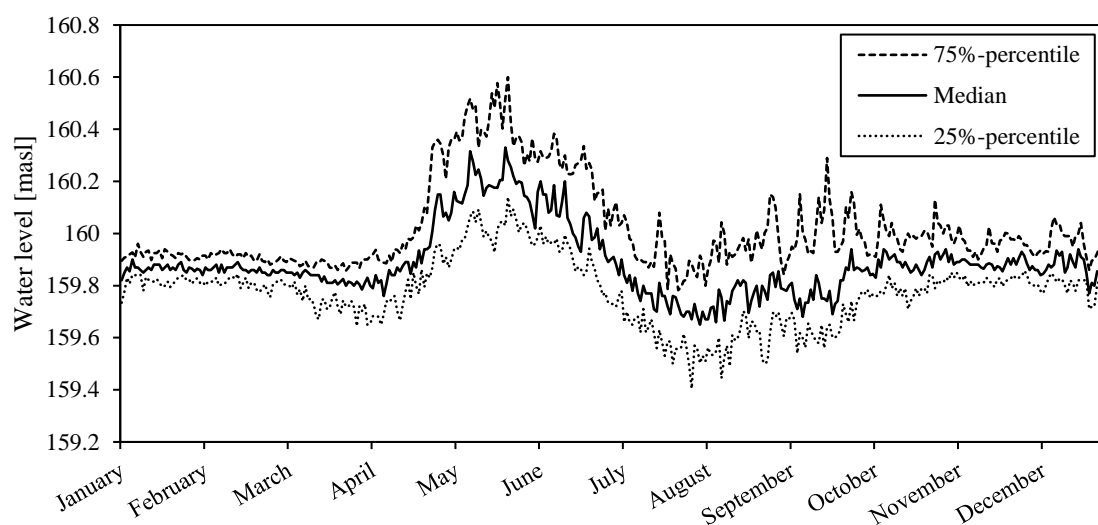


Figure 4: Recorded water level at the gauge station Kulset bru (nr. 123.34.0). The water level is based on daily recordings in the period from 1 January 1993 to 11 March 2019. (Data available from NVE)

Variations in discharge caused by operations of hydropower production with water being stored and released in order to meet market demand is often termed as hydropeaking. These flow regulations can create frequent and rapid flow events in regulated rivers with significant variations in flow velocity, water depth, water temperature, wetted area and sediment transport. The study of hydropeaking is of interest to many researchers and industry participants due to its potential to change river hydromorphology. These changes can lead to degradation of habitats and the physical conditions in local ecosystems, directly affecting the biological communities in and around the river. EnviPEAK is a collaboration of researchers, previously part of CEDREN (Centre for Environmental Design of Renewable Energy) have conducted research of the topic over several years. The work includes a study of environmental impacts due to hydropeaking caused by variations in hydropower production and propose mitigation measures to combat consequences of hydropeaking. Their research provides a tool for researchers and industry to assess the degree and classify the effect hydropeaking in a regulated river (Bakken et al., 2016).

2.3.3 Environmental design

There are several proposed measures to improve habitat conditions for the brown trout species in Nea. The measures include modification and stabilization of weirs, creating artificial channels and increasing depth in weir-reservoirs. The aim of these measures is to reduce

migration barriers, improve hydraulic conditions (i.e. velocity and depth) and create more areas considered as deep ($>1.5\text{m}$). The measures should also increase flow velocity in the river to create more potential spawning areas for brown trout (Bjølstad et al., 2014). The hydraulic model in this study investigates the hydraulic effects of planed weir modification measures.

The weirs in Nea were originally constructed to maintain water-covered areas for esthetic reasons. Weirs in rivers acts as a barrier to the flow, creating weir-reservoirs with slow-flowing water. Previous studies have shown that weirs can have a negative effect on fish communities in regulated rivers. Weirs also reduce the velocity due to areas in the river becoming pools. The weirs in Nea are probably a barrier for fish-migration and have reduced the available spawning areas for brown trout.

The measures modeled in this study have been proposed as to facilitate fish-migration and improve habitat conditions for brown trout in River Nea. The modifications of weirs are based on the principle of lowering one or more small sections in order to concentrate flow over the weir to ease fish-migration (Bjølstad et al., 2014). Modifications on one of the weirs is visualized in Figure 5 and a list of the measures included in the model can be seen in Table 1.



Figure 5: Visualization of proposed measure on a weir in Nea. Rocks in a 2 m section at the center is removed, lowering the section relative to the existing weir (Bjølstad et al., 2014).

A map of Nea (from the outlet of Nedre Nea to Heggsetdam) can be seen in appendix A. The map includes the location and index (1-33) for all the weirs in lower Nea.

Table 1: List of proposed measures on weirs in lower Nea with the location shown as coordinates for each weir and a description of the measure.

Weir	X (m)	Y (m)	Description	ΔZ (m)
6	607431	7009380	Lower 2 m section at the center.	0.4
9	608137	7008960	Left side: lower 10 m section. Right side: lower 2 m section.	0.5
21	612825	7004420	Lower 2 m section at the center.	0.5
22	613217	7004060	Lower 2 m section at the center.	0.5
23	613580	7003420	Lower 2 m section at the center.	0.5
24	613904	7002640	Lower 2 m section at the center.	0.5
27	614308	6999630	Lower 2 m section at the center.	0.5
28	614679	6999520	Left side: lower 2 m section. Right side: lower 2 m section.	0.5
29	615050	6999540	Lower 2 m section at the center.	0.5
32	616576	7000120	Lower 2 m section at the center.	0.5

From the outlet of Nedre Nea power plant up to Heggsetdammen 27% of the total area is estimated as good habitat areas for young trout in the river. However, the areas are not evenly spread out in the river. The area between the outlet of Nedre Nea up to weir 5 have few and small habitat areas. This is also seen in the area between weir 17 and weir 24, and in particular the area from weir 26 and 32. (Bjølstad et al., 2014). Many of the weirs modelled with measures are located in these areas and can potentially increase habitat areas for brown trout.

2.3.4 Hydraulic modelling

The hydraulic model is created in the Hydrologic Engineering Center's (HEC) River Analysis System (RAS) software developed by the US Army Corps of Engineers (USACE). HEC-RAS can perform one- and two-dimensional hydraulic analysis on river systems, channels and floodplains. HEC-RAS version 5.0 contains hydraulic analysis components capable of computing steady flow water surface profiles (1D) and unsteady flow simulations (1D and 2D). The software also includes modules for analyses on sediment transport, water quality and hydraulic design (USACE, 2016a). The hydraulic modelling in this thesis uses HEC-RAS 5.0.7 released in March 2019.

RAS Mapper is a built-in GIS tool in HEC-RAS providing a graphical interface for viewing results and tools to build a model. Importing and exporting shapefiles and rasters from RAS Mapper makes it compatible with GIS software to analyze simulation results. It is possible to draw full 2D geometries including 2D flow area perimeters, break lines, boundary conditions and when generating 2D mesh with the addition of manually placed computation points to correct for errors in the mesh as well as computing 2D flow area hydraulic tables.

The “Managing Results Map” tool in RAS Mapper is useful for exporting simulation results for more advanced analysis in external GIS software like ArcMap. The tool lets the user create a map containing simulation results as rasters for a specified unsteady profile (time in simulation), overlaid on a specified terrain. It is possible to export a range of different results, including depth, velocity, water surface elevation and inundation boundary. The latter two is useful in the calibration process where importing water surface elevation in ArcMap providing a toolbox for analysis with a range of raster math operations. Another option is to export results as profile lines with profiles imported to RAS Mapper or drawn directly in the GUI. The profiles can be cross sections showing changes in flow over time and WSE, depths or velocities at specified times in the simulation, or longitudinal profiles showing the water surface over the terrain. This allows for analysis of smaller areas in greater detail as well as changes over larger distances.

2.4 River ice

River ice is an important part of the cryosphere, having an impact on the global climate, surface energy and riparian ecology (Chu & Lindenschmidt, 2016). In cold climates, processes linked to river ice (e.g. ice jamming, flooding) can threaten critical infrastructure and influence in-stream hydraulics affecting hydropower production. Physically monitoring and mapping river ice can be a challenging task due to poor accessibility and potentially large survey areas. Active optical remote sensing with UAV can provide a low-cost, efficient and safe environment when studying the formation and break-up of river ice. This includes passive remote sensing methods for large rivers using satellite imagery and active remote sensing methods for smaller rivers by UAV acquired images at lower altitudes for a more detailed study on ice process dynamics.

River hydraulics plays and a significant role in the formation, development and break-up of river ice (Stickler et al. 2010). Ice cover formation is initiated by the cooling of water and turbulence in the water keeps the water temperature relatively uniform throughout the flow depth and width of the river channel. When the water becomes super-cooled ($T_{\text{water}} < 0^{\circ}\text{C}$) tiny ice particles (frazil ice) starts to form and due to their small size (a few mm in diameter) they are easily kept in suspension by turbulence in the water. Along riverbanks and around islands/protrusions the flow velocity gets reduced and turbulence is negligible, these are areas where ice particles start to form an ice cover. The super-cooled state of frazil particles makes them adhesive, causing them to accumulate and grow in size. Eventually reaching a size where the buoyant forces dominates over turbulence in the water, causing them to float to the surface. The floating ice continues downstream and may collide with each other or the ice that have started to form along the riverbanks, increasing the surface area of the ice formation. Another

process in which ice forms is located at the bottom of the river, where frazil ice gets deposited forming ‘anchor ice’ on the riverbed. With increased accumulation of anchor ice follows development of anchor ice dams, locations where the anchor ice reaches all the way to the surface. Solar radiation can reach the anchor ice raising its temperature sufficiently for it to break free from the river bottom and float to the surface. This phenomenon is often seen in steep rivers with fast flowing water, whereas the surface ice often forms in slow-flow areas in pools or along banks.

The break-up of river ice can occur slowly where the ice gradually melts or in a fast manner where the river ice breaks-up suddenly due to increased stream runoff (e.g. a combined rainfall-snowmelt runoff event) or an upstream ice jam release. Sudden river ice break-up is termed dynamic break-up and can potentially cause damage to infrastructure in or around the stream (roads, pillars, dams). Dynamic break-ups are often initiated by rising water levels in the river due to snowmelt runoff. The increased flow discharge causes stress on the ice cover which then can start to form cracks, causing parts of it to break free from the ice cover. Drifting ice can be constrained by smaller intersections in the river or by stronger, still remaining ice cover, causing an event known as ‘ice jam’. The build-up of floating ice can create an obstacle for the flow causing upstream water levels to increase. Rising water levels and continued accumulation of floating ice will increase forces on the ice jam, eventually causing it to collapse. The collapse will cause the ice jam to grow in thickness as ice sheets are pressed over each other in order to withstand the increased stresses. There can be many small ice jam break-ups occurring along the river during an ice run. This can cause a cascading effect potentially creating huge ice jams capable of causing damage to nearby structures or terrain due to forces on impact or flooding events.

Studying dynamic ice processes is of interest due to the many ways it can influence the river system and its surroundings. As previously mentioned, mapping of river ice with ground surveying methods can be dangerous and near-impossible to achieve with a scale and detail desired. Optical remote sensing data from satellites does not always give results with high accuracy or detail. UAV surveyed photographs in addition to processing with SfM software can provide a low-cost and effective method of mapping dynamic ice processes which are important to many ice assessments (Alfredsen et al. 2018), while maintaining safety requirements throughout the survey.

3 MATERIAL AND METHODS

The focus of this study is to use remote sensing data from LiDAR and UAV surveys to reconstruct digital models of the survey areas used for hydraulic simulations in Nea and mapping river ice in Sokna. The remote sensing data collected from these survey methods provides detailed data of the current geometries which can be used to investigate actual physical processes. Hydraulic modelling based on the current terrain model is used to investigate the hydraulic effects of planned modifications to some of the weirs in Nea. Analysis on the river ice in Sokna includes calculations of surface area and volume as the ice cover develops and locate areas where ice processes are likely to occur. Two airborne LiDAR surveys have been conducted in Nea, the first on 27 July 2018 and another on 18 April 2019, providing bathymetric data in lower Nea between Heggsetdam and Selbusjø. A 500-meter artificial channel seen in Figure 6 is included in the LiDAR data and have been surveyed with UAV on 11 September 2018. The optical remote sensing data from Sokna is used to reconstruct DEMs for mapping and analysis of river ice. Four UAV topographic surveys were conducted in the period November 2018 to April 2019.

This chapter includes a closer description of the study sites and the methods used to achieve the objectives in each study site. The methods put forward in this section includes a method for reconstructing a digital terrain model from LiDAR data with a description of constraints applied to the interpolation process in areas with low coverage and remove model artefacts. This chapter present three approaches for editing terrain data used to implement weir measures in the model. The methods used to assess the LiDAR data quality is described including the process for obtaining control points with ground-based GNSS measurements used to evaluate the vertical accuracy and georeference UAV and LiDAR models. The hydraulic model created in HEC-RAS is also described in this chapter, including model setup, simulation parameters and calibration process.

3.1 Study Sites

3.1.1 Nea

Nea is characterized by wide sections and some narrow riffles in the upper areas. Most of the river area has slow flowing water with some short and long riffles in between. Periods of low flow prior to the weirs being constructed would dry up large areas in the river. The weirs

mitigate this effect to some extent by increasing water depth and wetted area in slow flowing weir-reservoirs. The catchment area of Lower Nea is estimated to 2,081 km² and the average slope is 9.2 m/km.

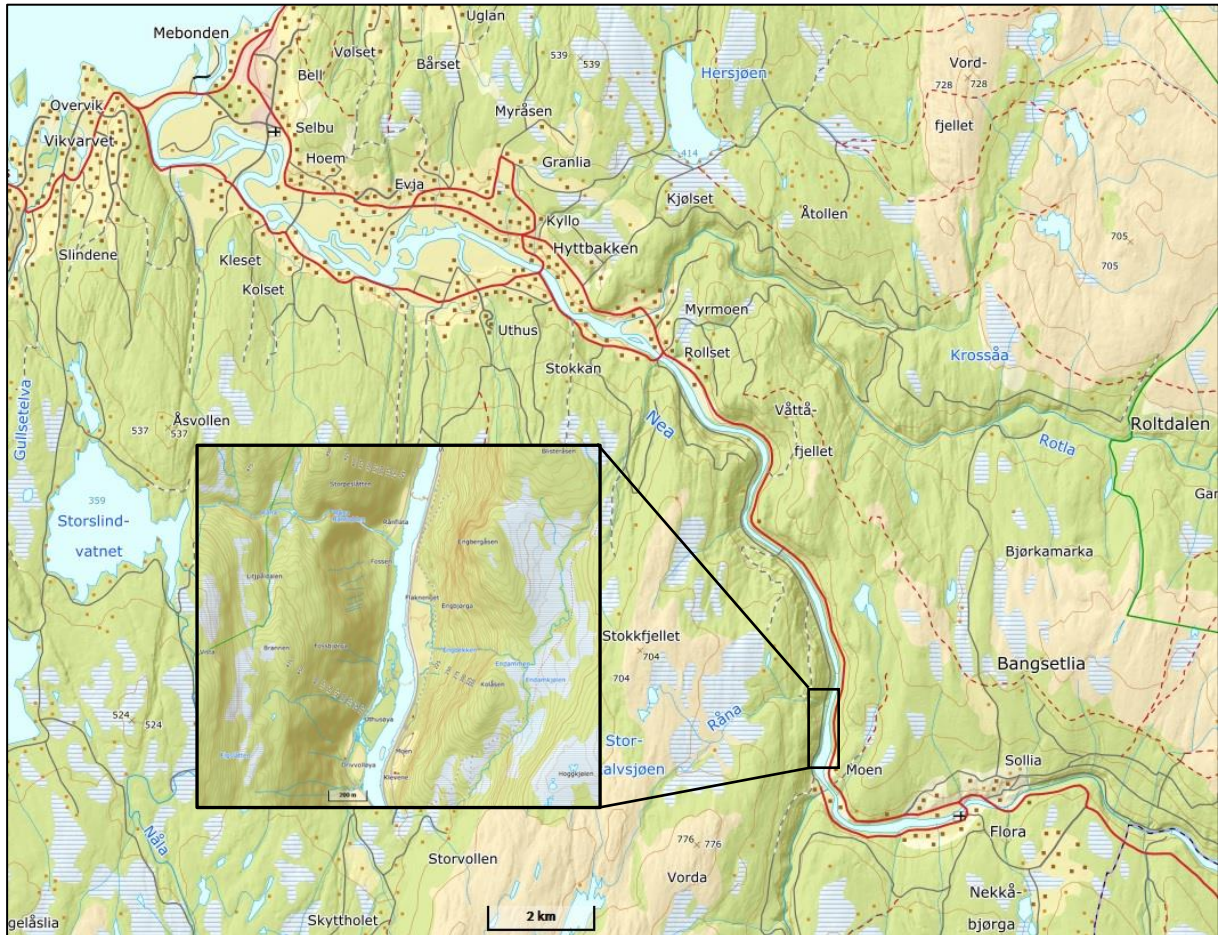


Figure 6: Map of the 34 km long study area in Nea surveyed by LiDAR. The artificial channel surveyed with UAV is shown in focus.

The artificial channel seen in Figure 6 have been surveyed with UAV and differential GNSS on 11 September 2018 in sparsely clouded conditions and low wind speeds (0-2 m/s). The survey captured 691 aerial photographs of the study area with flying altitudes of 20-80 m. The effective flying time for this survey was 27 minutes (time of start: 11:15, end: 11:42). The survey included 12 markers to be used as GCPs, spread around the survey area and captured in the aerial photographs. Unfortunately, the differential GNSS equipment was unable to measure the position of each marker due to outdated firmware in the controller, effectively rendering the GCPs accuracy equal to the drone's GNSS accuracy. The study area was surveyed again on 9 October 2018 to collect GCPs for the model reconstructed from the previously collected data.

The GCPs were measured on road markings, crash-barrier posts and large rocks, objects which were unlikely to have changed position since the UAV survey and would be easily identified in the UAV data.

3.1.2 Sokna

Sokna is a tributary to Gaula located south of Midtre Gauldal in Norway. The catchment area of Sokna is estimated to 539 km² with a mean winter flow of 2.5 m³/s and a mean gradient of 1.7%. The study site is a 150 m sections (N 62°58'40.87119", E 10°13'25.9259") seen in Figure 7 and is a steep river with a bed consisting of large cobbles and boulders. Fast flowing riffles and short pools characterize this study site which has an average width of 5 meters.

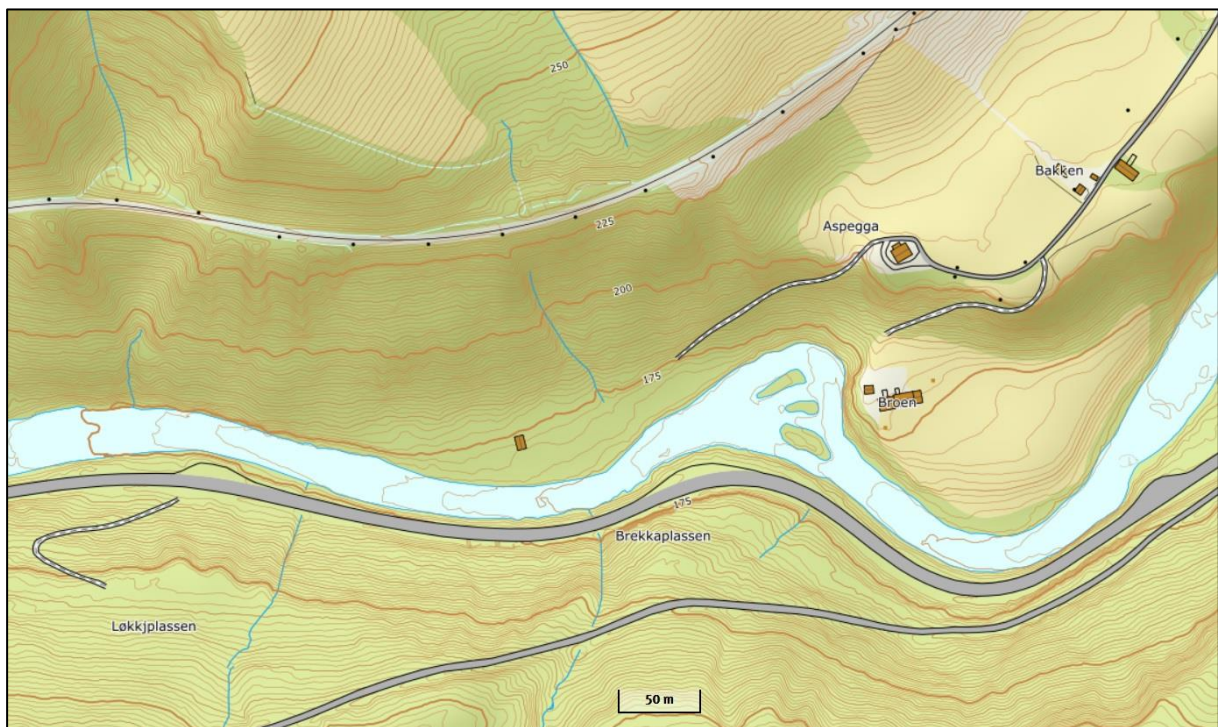


Figure 7: Map of the studied area in Sokna and surrounding topography.

Four topographic UAV surveys of Sokna in the period from November 2018 to April 2019 provides optical remote sensing data for the developing ice, in addition to a completely ice-free geometry captured by the November 2018 survey. The four surveys included 10 evenly spaced markers measured with differential GNSS to provide GCPs to georeference the data.

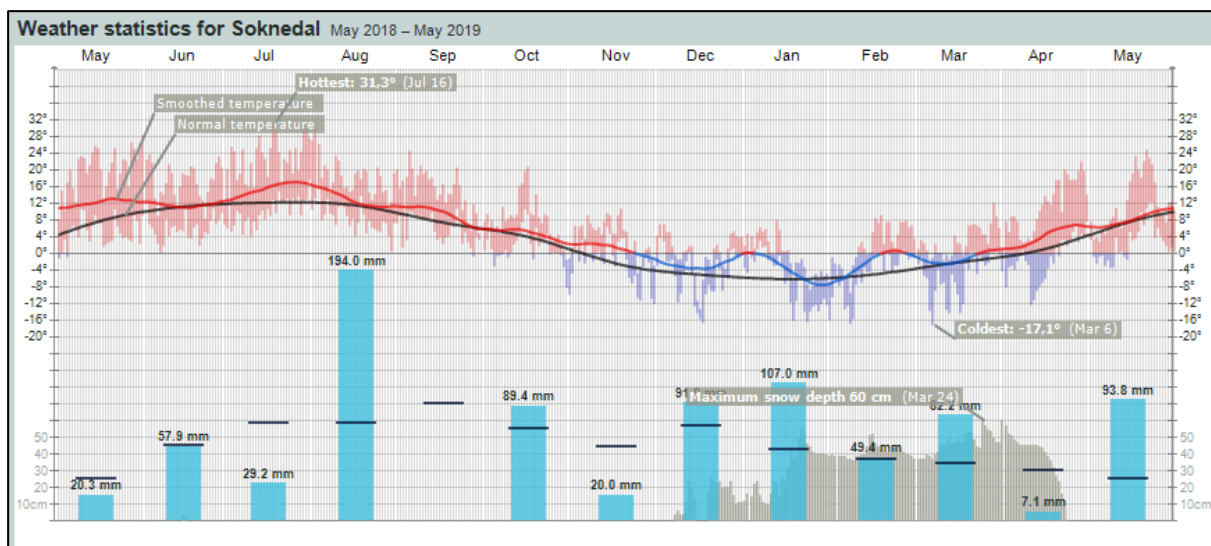


Figure 8: Weather statistics for Sokna the last year (May 2018 to May 2019) recorded at Soknedal observation station. The black line in the upper graph shows the normal temperature and the red/blue line the recorded temperature. The graph shows that the average temperature is higher than the expected normal this last winter (yr.no, 2019).

The weather statistics for Sokna over the recent year can be seen in Figure 8. The weather conditions are an important factor to consider when investigating river ice development and dynamic ice processes. Wind, temperature and precipitation must be considered when planning UAV topographic surveys for mapping a developing ice cover and ice run events. The weather statistics for Sokna show a mild winter, with an average temperature higher than the expected normal for all but the last week in January.

3.2 LiDAR Data

The LiDAR data used in this study is comprised of two datasets obtained from separate ALB surveys in Nea. The Norwegian geodata company Terratec surveyed the data with the multispectral Opec Titan sensor. Terratec is a supplier of accurate geodata with experience in mapping river bathymetries. The first dataset was surveyed on 27 July 2018 and delivered in January 2019. The gauge at Kulset bru recorded a discharge of 32.35 m³/s downstream of Nedre Nea outlet. Heggsetfoss power plant not in operation this day and a minimum flow scenario assumed in the upstream area based on visual observations. The data was uploaded to a FTP-server accessible with username and password and included 61 LAZ files containing point-clouds, orthophotos from the survey and two shapefiles containing polylines and polygons representing the water surface boundary. The second dataset were surveyed on 18 April 2019 while with ice present in the river. Ice is problematic for LiDAR surveys and areas in the river

with ice cover requires manual processing by the supplier. The 2019 LiDAR data was delivered in May 2019 and did not include polyline features of the water surface boundary.

The suppliers processing of LiDAR data includes a process to georeference the LiDAR point cloud and require control points with known locations from independent sources spread out over the survey area. 221 GCPs were surveyed with differential GNSS and supplied to Terratec as four profiles across the river and four evenly spread 4x4 squares with a point spacing of 1 meter.

The software suite LAStools developed by Rapidlasso GmbH is used to decompress the supplied LAZ files from Terratec to a LAS format. The LAStools software suite is the fastest and most memory efficient solution for processing LiDAR data with a simple GUI (Rapidlasso, 2019). LAStools is compatible with most of the recognized GIS software including ArcGIS used in this study. The LAS files are loaded into ArcMap for analyses and processing.

3.2.1 Terrain model

The basis for the hydraulic modelling in this work is a LiDAR derived DEM of the river bathymetry. A combination of 2018 and 2019 LiDAR point-clouds is used to reconstruct a DEM in ArcMap. The combined data still show areas with no LiDAR data on the riverbed. Areas with no data create artefacts in the model due to interpolation across large distance. A method to mitigate this is found by adding break lines with height values to the LAS datasets to constrain the interpolation. The riverbed elevation in these areas is assumed from satellite images and orthophotos from the survey, introducing a potential source of error to the model.

Break lines were added to the LAS datasets as surface constraints in the form of a shapefile containing polylines. A value field for the assumed elevation of each break line were added to the attribute table and the polylines were drawn into the areas with few or no LiDAR points and the assumed elevation added to the new “Height” field for each feature. The shapefile containing break lines were then added to the LAS dataset as a “Surface Constraint” with the added field set as “Height value” and selecting “Hard line” as the constraint type.

A functional surface is reconstructed for each LAS dataset as a raster in the TIFF-format in ArcMap using the tool “LAS Dataset to Raster”. The interpolation type “Triangulation” is used to rasterize the LiDAR data due to the surface constraints put on source data requiring a triangulated interpolation to constrain the model. The interpolation method ‘Natural Neighbor’ was used in this process. Thinning of LiDAR points were done by ‘Window Size’ using ‘Closest to Mean’ as the point selection method and the rasters created with a sampling value of 0.5 m.

3.2.2 Editing terrain data

Finding a method for editing terrain data in order to implement measures on weirs to the model has been an important task for this thesis. The method should create precise changes in the specified locations and provide reproducible results. Three approaches for implementing the weir measures to the terrain model have been found and evaluated for this purpose. A description of each method is seen in the following, as well as the results they produce in the terrain model.

Implementing the planned measure on the weirs in Nea requires a DEM reconstructed from measured data, except in areas with modelled weir measures. The elevation of terrain points in these locations does not correspond with the elevation of measured LiDAR points in these areas. The following procedure describe a process for implementing the weir measures using ArcMap and las2tex included in the LAsTools software suite. The first step is to create a shapefile and draw a polygon of the area on a weir representing the section to lower. One shapefile and with a single polygon for each of the measures is created. The ‘Extract LAS’ tool is used to extract the xyzi-values of all points inside the polygon area. The LAS dataset containing the points is used as input and the polygon feature in the shapefile set as ‘Extraction Boundary’. The output of this process is a LAS file containing xyzi-values for all points in the section to be lowered. The next step uses the software ‘las2txt’ to convert the LAS file to a .txt file. The LAS files is loaded to the software with the projection set to ETRS89 UTM 32 N with NN2000. “Process all files” were selected and the option to “merge files into one” checked, merging the 2018 LAS file and 2019 LAS file into a single file. Set the Output folder and desired output filename chosen and run the program. This will convert input LAS files to .txt files containing all extracted points and their xyzi-values. Importing the .txt file to MS Excel The extracted LAS points were imported to MS Excel and the z-coordinate of all the points reduced by the ΔZ value corresponding to the measure as seen in Table 1. The software ‘txt2las’ will convert the .txt file with lowered elevations into a LAS file with the terrain data for each weir measure included. Adding the modified LAS points to the LAS dataset and reconstructing DEM as previously described will build a model of the weir measure as seen in Figure 9.

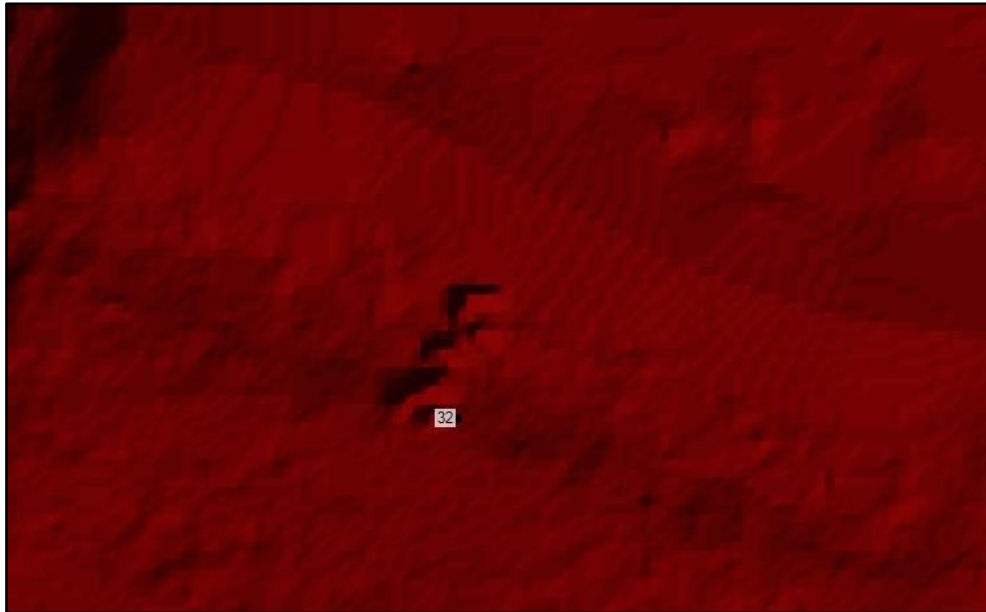


Figure 9: Terrain model after implementing the measure on weir 32 by manipulating LAS point heights in ArcMap.

The second approach to implement measures on weirs to the model uses HEC-RAS to edit the terrain layer. This step requires a terrain layer in RAS Mapper built from the original DEMs. Cross-sections are drawn on each side of the weir, representing the total length of section to be lowered in the flow direction. The stations and elevation of terrain points can be edited in each of the cross-sections in the “View/edit Geometry” window. After adding the measure to each of the cross sections RAS Mapper is used to ‘Compute XS Interpolation Surface’ for the ‘Interpolation Surface’ geometry. A 1D geometry is required in both the cross-sections to compute the interpolation surface. The terrain model is created through linear interpolation between the cross-sections and can be exported in the TIFF-format by selecting ‘Create Terrain Geo TIFF from XS’s (channel only)’ in the ‘Export Layer’ menu of the geometry of the cross-sections. The terrain model obtained from this approach can be seen in Figure 10. A problem seen when interpolating between cross-sections is removal of ‘good’ terrain data found on the weir.

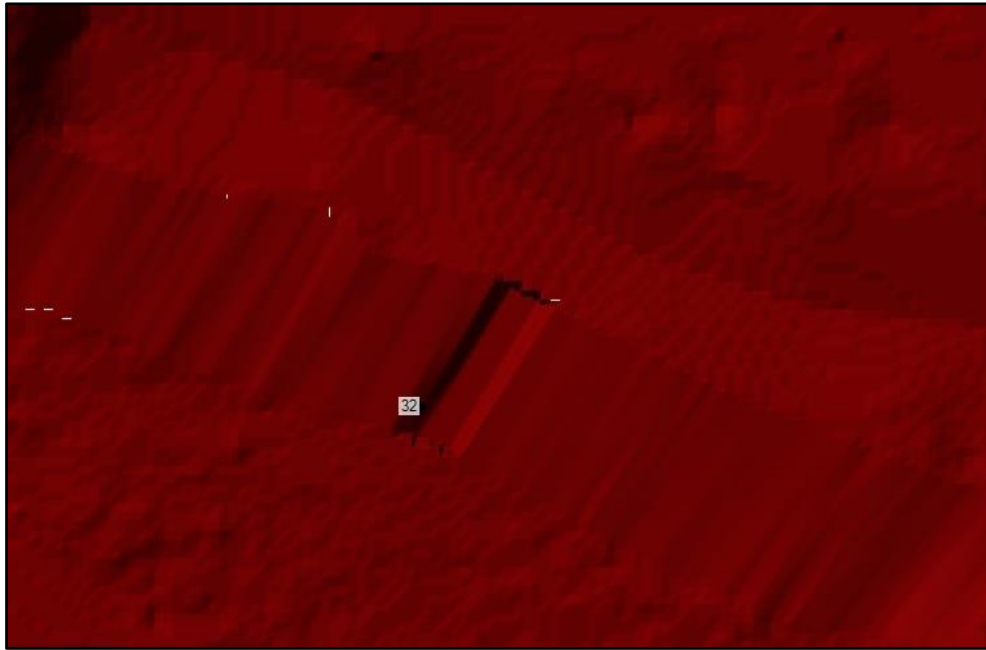


Figure 10: Terrain model after implementing the measure on weir 32 by interpolating between two cross sections in HEC-RAS.

Editing the source data with triangulation interpolation does not provide a predictable methodology of terrain modification. Another method is to reconstruct the raster surface from the original LiDAR point-cloud with a polygon surface constraint setting the height of the model in the location of a measure. A shapefile with a polygon of the lowered area is drawn in ArcMap and the elevation of the lowered section added as to a 'Height' field. The shapefile is added to the LAS dataset as a surface constraint with 'Height Source' set to the added field for elevation and the 'Surface Feature Type' set as 'Hard Replace'. Reconstructing a raster surface from the LiDAR point-cloud with surface constraint included results in a terrain model with a lowered section on the weir, as seen in Figure 11.

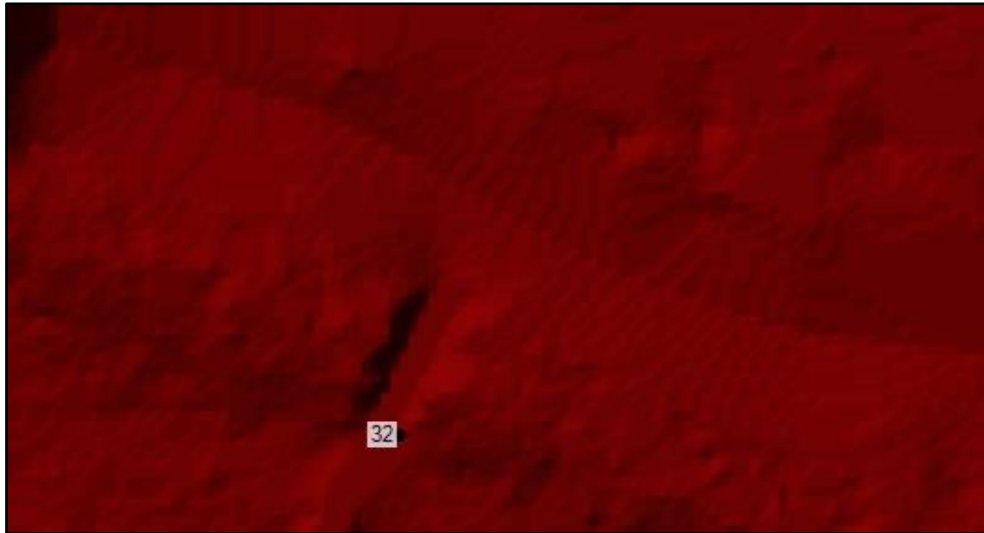


Figure 11: Terrain model after implementing the measure on weir 32 by applying a surface constraint to the LAS dataset in ArcMap.

Methods described in this chapter will generate a terrain model with a lowered section on the weir. To implement measures on the weirs in this study the DEMs were reconstructed from the original LiDAR data using a polygon surface constraint with a set height value to lower sections on the weirs. This method did not change the surrounding terrain like XS interpolation do, changes to the section area or height lowered are added to the shapefile more efficiently than the first approach. The terrain model for each modified weir using polygon surface constraint described here, can be seen in appendix A.

3.2.3 Quality assessment

The quality assessment of available LiDAR from Nea includes evaluation of absolute vertical accuracy and bathymetric coverage of LiDAR points on the riverbed. The American Society for Photogrammetry and Remote Sensing offer guidelines to assess the absolute vertical accuracy in a LiDAR dataset, described in the Positional Accuracy Standards for Digital Geospatial Data (2014). The American standard do not include bathymetric LiDAR points, referring to water-bodies in survey areas as ‘acceptable data voids’ to be excluded from the accuracy assessment.

The ASPRS standard specifies accuracy and placement requirements for control points and checkpoints for LiDAR data. Checkpoints are used to evaluate vertical accuracy in a dataset and have the highest accuracy requirements the two ground measurements. Checkpoints from independent sources should be three times more accurate than the LiDAR data being evaluated. The standard also specifies that no less than 20 checkpoints can be used to evaluate vertical

accuracy in LiDAR data. ASPRS recommends 100 static vertical checkpoints for the first 2,500 km² in a study site. The checkpoints should be spread out over the survey area include all types of terrain seen in the survey area. The control- and checkpoints used in this study are measured with differential GNSS with an accuracy of 1-3 cm in the vertical direction. Vertical accuracy in LiDAR data is typically on the decimeter level.

The absolute vertical accuracy of the LiDAR data is a measure of the accuracy relative to real-world coordinates and is evaluated by comparing checkpoint elevations with elevations in the LiDAR data. The vertical accuracy is evaluated by comparing checkpoint elevations with elevations in the LiDAR derived DEM at the same locations. The vertical accuracy assessment is based on 171 check points. The checkpoint to DEM comparison is achieved by extracting elevations in of the DEM where the checkpoints are located. The spatial analyst tool ‘Extract Multi Values to Point’ is used to find elevations of the DEM at each checkpoint location. The tool extracts the DEM values to a shapefile with DEM values for each checkpoint in the attribute table.

The ASPRS standard do not include specific requirements when evaluate the bathymetric coverage of a LiDAR survey. The Lidar base specification developed in the U.S. Geological Survey (USGS) National Geospatial Program (NGP) describes the spatial distribution in over-water LiDAR points in terms of Nominal Point Spacing (NPS) and Nominal Point Density (NPD), and defines a ‘data void’ as an area greater than, or equal to $(4 \times \text{NPS})^2$ (Heidemann, 2018). Point spacing and point density are familiar terms used to describe the spatial distribution of LiDAR points and will be used in this thesis as a measure of the bathymetric coverage.

The bathymetric coverage is found in ArcMap by creating a shapefile and drawing a polygon feature of the channel area. A second shapefile is used to draw polygons over large islands and terrain in the channel area. The shapefile supplied by Terratec containing polygons cover some of the over-water terrain seen in the channel. Orthophotos and raster from the measured water surface are helpful when locating remaining terrain areas in the channel. The analysis tool “Erase” with the channel area polygon set as input and the terrain polygons as erase features removes terrain polygons from the channel boundary. The area of the channel can be estimated with the “Calculate Geometry..” found in the attribute table. The data management tool “LAS Point Statistics by Area” adds a column to the attribute table with the selected statistical value as output. With LAS dataset as input, the channel area polygon as input polygons and “Point Count” the desired output property the tool will find all the points located inside the channel area, giving an estimate of the bathymetric LiDAR points. The statistics for the 2018 and 2019

were calculated separately in order to get an estimate of the bathymetric coverage for each survey and to avoid areas with overlapping LiDAR points. Point density is calculated as points per square meter (pts/m²) and point spacing is the average distance between points.

3.2.4 Additional data

The LiDAR data from Nea was georeferenced with 221 GCPs surveyed during a field trip to Nea on 9 October 2018. The 221 GCPs used to georeference the LiDAR data is no longer an independent source and will not serve the purpose of a checkpoint for accuracy assessment. During the October field trip 16 GCPs were measured and used to georeference the UAV survey data. The UAV model's GCPs is still considered as an independent source to the LiDAR data and can be used as checkpoints. However, positional standards state that in no case should accuracy be based on less than 20 checkpoints, recommending 100 static vertical checkpoints for areas up to 2,500 km² (ASPRS, 2014).

The need for additional survey data in Nea were evaluated based on the number of available checkpoints and their concentrated locations not meeting the requirements for checkpoints. Additional data were collected during a survey in Nea on 3 June 2019 collecting 171 checkpoints to the LiDAR data.

3.3 UAV Photogrammetry

3.3.1 Image acquisition

The aerial images is acquired using a DJI Phantom 3 Professional drone and its built-in 4K resolution camera Sony EXMOR 1/2.3" mounted on a three-axial gimbal. Phantom 3 Professional is a quadcopter with a built-in GNSS that allows for auto-stabilization under normal wind conditions for flying. The drone uses a dual satellite positioning system, combining GPS and GLONASS, obtaining an accuracy of ± 0.1 m (VPS+GPS) or ± 0.5 m (GPS) vertically and ± 1.5 m horizontally. The GNSS accuracy level allows the drone to auto-stabilize in-flight and enables the drone to follow a pre-planned flight route but the accuracy level is not sufficient to georeference the DEM or orthophotomosaics. UAV topographic surveys often include GNSS measurements of GCPs to georeference the survey data

The Phantom 3 Professional weighs 1280 g with the battery and propellers included. It is capable of vertical speeds up to 5 m/s ascent and 3 m/s descent. In perfect flying conditions the drone may reach a maximum speed of 16 m/s and a flying altitude of 6000 m. DJI Phantom 3 Professional and its camera has a specified operating temperature range of 0°C to 40°C and is

able to fly at wind-speeds up to 10 m/s. Three of the surveys carried out in this work were conducted at temperatures as low as -7°C. This reduced the flying time of the drone from the specified approximation of 23 minutes, down to 12-15 minutes. Flying the drone in cold weather conditions is not ideal as the controller may regularly warn of cold battery temperatures and signal transmission errors. Cold temperatures can affect the camera and snow-covered areas can introduce variable lighting conditions reducing the quality of the photographs.

The DJI FC300X camera has 12.4 M effective pixels and the camera lens a field of view of 94° 20 mm (35 mm format equivalent) f/2.8, focus at ∞ . The ISO range for photographs is 100 – 1600, the shutter speed ranges from 8 s to 1/8000 s and the maximum image size is set to 4000x3000. The camera of Phantom 3 Professionals is mounted on a gimbal that allows for a change in pitch from - 90° to + 30°, as well as 3-axis stabilization with an angular control accuracy of $\pm 0.02^\circ$.

All the flights were conducted using the DJI remote controller connected to an Apple iPad with the DJI GO application running. As previously mentioned, the built-in GNSS system of DJI Phantom 3 Professional allows for pre-planned flight routes. However, due to drone-flight regulations, the small size of the study area and picture quality requirements the drone was manually controlled from the ground. To ensure good data for the SfM processing the pictures were captured at a planar view with a minimum forward overlap of 20 %. The pictures were stored on a SD-memory card in the drone along with the respective EXIF data and GPS position associated with the image.

3.3.2 Photogrammetric processing

The general workflow used in Photoscan to build 3D surface, DEM and orthophotomosaic include the following steps:

1. Import your photos
2. Manually sift through and remove images that are obvious ‘outliers’ (e.g., images taken prior to take-off)
3. Convert GPS coordinates of the geotagged images (WGS84) to the desired coordinate system (matching the GCPs). Note that altitude information stored in the EXIF data of images acquired with DJI Phantom 3 is the relative altitude from its take-off location, not the absolute world altitude. There are scripts available online for transforming relative altitude to absolute.
4. Estimate image quality, include images with a quality index above 0.7-0.8.
5. Align photos (quality: high, pair selection: generic, key point limit: 40,000, tie point limit: 4,000, adaptive camera model fitting: no)
6. Import your GCPs and check points.

7. Identify and link markers to images. The “Filter by markers” option is useful in this process. After placing all the markers press the “Update” button in the reference pane.
8. Uncheck all images in the reference pane. Assuming a sufficient number of GCPs (10 or more), uncheck 20-30% of the GCPs. The unchecked points will now be used as checkpoints to measure the actual accuracy of the model.
9. Clean sparse point cloud with ‘Gradual selection’, remove all points with a reprojection error greater than 0.5. Manually delete obvious outliers.
10. Adjust the bounding box to fit the data.
11. Re-align sparse point cloud.
12. Optimize camera alignment.
13. Build dense point cloud (quality: high, depth filtering: aggressive, calculate point colors)
14. Build mesh (source data: dense cloud, surface type: height field (2.5D), face count: high, interpolation: enabled) Note: not needed if the desired result is a DEM and/or orthophotograph.
15. Build texture (mapping mode: adaptive orthophoto, blending mode: mosaic, texture size: 2048, enable hole filling). Note: not needed if the desired result is a DEM and/or orthophotograph.
16. Build DEM (set the coordinate system and vertical datum, source data: dense cloud, interpolation: enabled)
17. Build orthomosaic (surface: DEM, blending mode: mosaic, enable hole filling)

3.4 Ground Surveying

The GCPs and post-processing control points were measured on the ground during the UAV survey, ensuring that every marker placed were captured in the aerial images. The markers used is custom-made square of red tarpaulin sheets with a size of 0.25 x 0.25 m with a high-contrast (black/white) circle area in the center, allowing for precise identification of the measuring device placement on the marker in the post-processing process. The GCPs were surveyed using a Leica Viva GS15 GNSS smart antenna connected through Bluetooth to a Leica CS15 controller. The accuracy of Leica Viva Differential GNSS is 1-2 cm in the XY direction and 1.5-3 cm in the Z direction.

Real-Time Kinematic (RTK) differential GNSS uses a method of relative positioning to enhance the precision of the position data derived from satellite-based positioning systems. The method is based on a network of base stations with known positions to build a Virtual Reference Station (VRS) (and estimated rover position). The position relative to connected satellites is calculated with correctional data supplied by the network control center. RTK requires a minimum of 5 satellites with elevations over the horizon to obtain an accuracy of below 5 cm. The rover will use the VRS as it were a nearby physical base station, eliminating the need for

the user to set up one prior to surveying. The Norwegian Mapping Authority operates the RTK network CPOS with close to 180 base stations spread out across the country. The GNSS equipment connects to the CPOS server through an internet connection or GSM/4G services.

The GNSS equipment used to measure the ground points in this study recorded z-coordinates in the NN54 vertical datum, while the LiDAR and UAV models uses NN2000. This required conversion of the z-coordinate of each point from NN54 datum to NN 2000 before using them as check points or control points. The relative difference between these datums are found for nearby reference marks in the online map service from the Norwegian Mapping Authority. The two closest reference marks in Nea have a relative difference of 0.186 m and 0.197 m going from NN54 to NN2000. GCPs measured in Nea are converted to NN2000 by adding the average relative difference of 0.1915 m to the z-coordinate. The two closest reference marks to Sokna have a relative difference between NN54 and NN2000 of 0.102 m and 0.123 m. The average difference of 0.1125 m is added to these measurements to convert them from NN54 to NN2000.

3.5 Hydraulic Modelling

3.5.1 Model setup

Choosing the model setup is based on the data available for the underlying terrain. The LiDAR data provides a detailed terrain model which cannot be fully utilize the one-dimensional approach of interpolating between cross-sections cannot fully utilize. A two-dimensional modeling approach will be advantageous in areas where the river system is highly braided or the direction of flow changes abruptly e.g. around bends where a significant amount of super elevation is bound to occur. A two-dimensional model will also produce better results in applications that require fine detailed results of hydraulic components in the flow around or over objects like weirs (USACE, 2016b). A constant value flow hydrograph is used as an upstream boundary condition for the unsteady flow simulation. The hydraulic simulations in this work is done with a two-dimensional model solving the diffusive wave equations, a setup based on the available terrain data and the model's purpose of studying changes in hydraulic conditions around the weirs.

3.5.2 Parameters

Building a two-dimensional model in HEC-RAS is a process that requires several steps. A terrain layer is created in HEC-RAS from the DEM, and the geometries drawn or imported in RAS Mapper. Creating the terrain layer requires a projection to be set for the model. The

hydraulic model is projected in the same projection as the LiDAR data, i.e. ETRS89+NN2000. The rasters created in ArcMap were set as input for the terrain layer and the precision set to 1/32 with the option to 'Create Stitches' checked. It is not desirable to create the terrain as a single raster file of the large survey area, unchecking the option to 'Merge Inputs to Single Raster'. An overlapping region around the intersection of raster 5 and 4 resulted in an unnatural artefact, effectively walling of the channel area going from raster 5 to 4. This was combated by changing the priority of the rasters, ensuring higher priority for raster 5 in the list of inputs.

The geometries include a flow area perimeter, break lines, cross sections and boundary condition lines. The two-dimensional flow area constructs a computational mesh with a set cell size and computation points in each cell. The flow area perimeter and cross sections were manually drawn in RAS Mapper, and the break lines included a combination of imported and manually drawn polylines. Break lines is placed inside the flow area perimeter to align the cell faces in the direction of the break line. HEC-RAS 5.0 User's manual recommends the user to add break lines in any location acting as a barrier or otherwise controls the direction of the flow (USACE, 2016a)

Break lines were added to the model by importing polyline features from a shapefile supplied by Terratec. The shapefile contained a total of 240 polylines features representing the water surface boundary measured in the 2018 LiDAR survey. Break lines were manually drawn perpendicular to the direction of flow, upstream and downstream of each weir. The flow area mesh cell size is set to 5 m. A finer grid with cell sizes of 1, 2 and 2.5 m, and a courser grid with cell sizes of 10 m have been tested and the decision of cell sizes of 5x5 meter was based on the required computational time and stability in the simulations. The default Manning's n value in the mesh were set to $0.03 \text{ s/m}^{1/3}$. The final mesh contained 204 561 cells and the computational time for a full simulation run estimated to 9-12 hours. The geometry was completed after drawing the boundary condition lines, specifying the upstream and downstream boundary condition type as external and connecting it to the flow area.

The unsteady flow simulations require an unsteady flow data file with the type of each boundary condition specified. The upstream boundary condition at Heggsetdam is a constant flow hydrograph for the three flow scenarios $1.5 \text{ m}^3/\text{s}$, $5 \text{ m}^3/\text{s}$ and $10 \text{ m}^3/\text{s}$, with a data time interval of 15 minutes. The downstream boundary condition is a normal depth value of 0.0027, equal to the measured slope where Nea enters Selbusjøen. At the downstream end of the artificial channel a measured slope of 0.0033 was used as downstream boundary conditions. The unsteady flow analysis ran three independent programs during the simulation, the geometry

preprocessor to ensure the geometry's hydraulic table is updated, the unsteady flow simulation and the post processor. The simulations use an adaptive time step based on the courant condition with an initial computation interval of 1 minute. A maximum Courant number of 3 and a minimum Courant number of 0.5 ensures model stability. The minimum number of steps before doubling, the maximum doubling of base time step and the maximum number of halving time steps were all set to 4. This set of options ensured model stability while keeping the computational time within reasonable boundaries, with the adaptive timestep reaching a value of 2.344 seconds with up to four iterations. The total travel time of the water through the model have been calculated to 55 hours. The simulation time window was set to an arbitrary future date and lasting for 55 hours.

3.5.3 Calibration

Calibration of the hydraulic model revolved around changing the roughness at different locations along the river, trying to match the measured water surface elevations to the simulated. The LiDAR survey on 27 July 2018 mapped the water surface elevations in the 34 km reach of Nea, during the survey the flow is assumed to be $1.5 \text{ m}^3/\text{s}$ between Heggsetdam and Bogstadhølen. The flow area's default Manning's n value of $0.03 \text{ s/m}^{1/3}$ is used as an initial assumption. To change the roughness in an area a polygon containing a different Manning's n value is added to the model. Two different approaches for doing this have been tested. The first revolves around creating a Manning's n region SHP file in ArcMap. The second approach uses the built-in capabilities in RAS Mapper to create the same SHP file containing polygon features. The two approaches yield identical results, and due to the many 'trial and error' simulations and modification of the Manning's regions the approach using only RAS Mapper was used to create the Manning's n raster.

The method first used in the calibration process requires a shapefile containing polygon regions created in ArcMap, projected in the same reference system as the model. A value field is added to the attribute table containing Manning's n values for each polygon region. Next, the map layer "Manning's n Layer" is created in RAS Mapper by selecting "Add New Manning's n Layer ..." and setting the shapefile containing polygon features with "Geometries" as the import extent. In this approach, modifications to the Manning's n layer are first added to the shapefile with ArcMap before creating a new Manning's n layer in RAS Mapper.

The next approach does not require ArcMap when applying changes to the Manning's n layer when calibrating. Polygon features containing Manning's n regions can be created directly in

RAS Mapper. A “Manning’s n Polygon Layer” is created in RAS Mapper and polygon regions containing the Manning’s n value are drawn directly into RAS Mapper. After drawing all polygon regions, the “Stop Editing” function will invoke a dialog prompting to create a “Manning’s n Value Layer”. This layer is a raster with fixed cell size in the TIFF format containing all the polygon regions and their Manning’s n value. This approach to generate a raster with Manning’s n values do not require importing and exporting features between ArcMap and HEC-RAS.

The process is initiated by creating a “Manning’s n Polygon Layer” in the RAS Mapper. Completing a drawing makes a dialog appear asking the user to specify the Manning’s n value for the newly added polygon, either an existing value already used or a new region with a different Manning’s n value. This layer is stored as a shapefile containing the drawn in polygon features. Creating a raster with the Manning’s n values is done by “Add New Manning’s n Layer...”. The shapefile with polygons is selected as input and the already set Manning’s n values appears for each region. The model of Nea used six Manning’s n regions with values of: 0.006, 0.01, 0.018, 0.045, 0.06 and 0.08 s/m^{1/3}. Considering the default Manning’s n value of 0.03 s/m^{1/3} in the flow area, the model effectively used seven different Manning’s n values. The raster was created with a cell size of 0.25x0.25 meters.

The initial Manning’s n layer is associated to the geometry before starting the simulation. After completing the simulation, the calculated water surface was visually compared to the LiDAR water surface in RAS Mapper. This is an efficient method of finding areas with large differences in water surface elevation. After locating regions with elevation differences larger than 0.1 meter, the Manning’s n value of the polygon in that area would be changed in the shapefile in RAS Mapper, or a new polygon region would be added to replace the default value of 0.03 s/m^{1/3}. Then the updated Manning’s n value raster must be created and associated to the geometry, before continuing the calibration process. A more comprehensive and detailed analyses of the difference between measured and simulated water surface can be done by exporting a map result of the simulated water surface and importing it to ArcMap. In ArcMap the ‘Raster Calculation’ tool ‘Minus’ can be used to subtract the simulated water surface elevations from the measured LiDAR water surface elevations. This will produce a raster containing the residuals, which can then be classified into the desired ranges, showing areas with successful calibration and areas with errors exceeding the set boundaries. Figure 12 show the final raster containing the residuals after completing the calibration process for this

hydraulic model. The boundaries of accepted errors are colored with black for easy identification of areas where the calibration was successful.

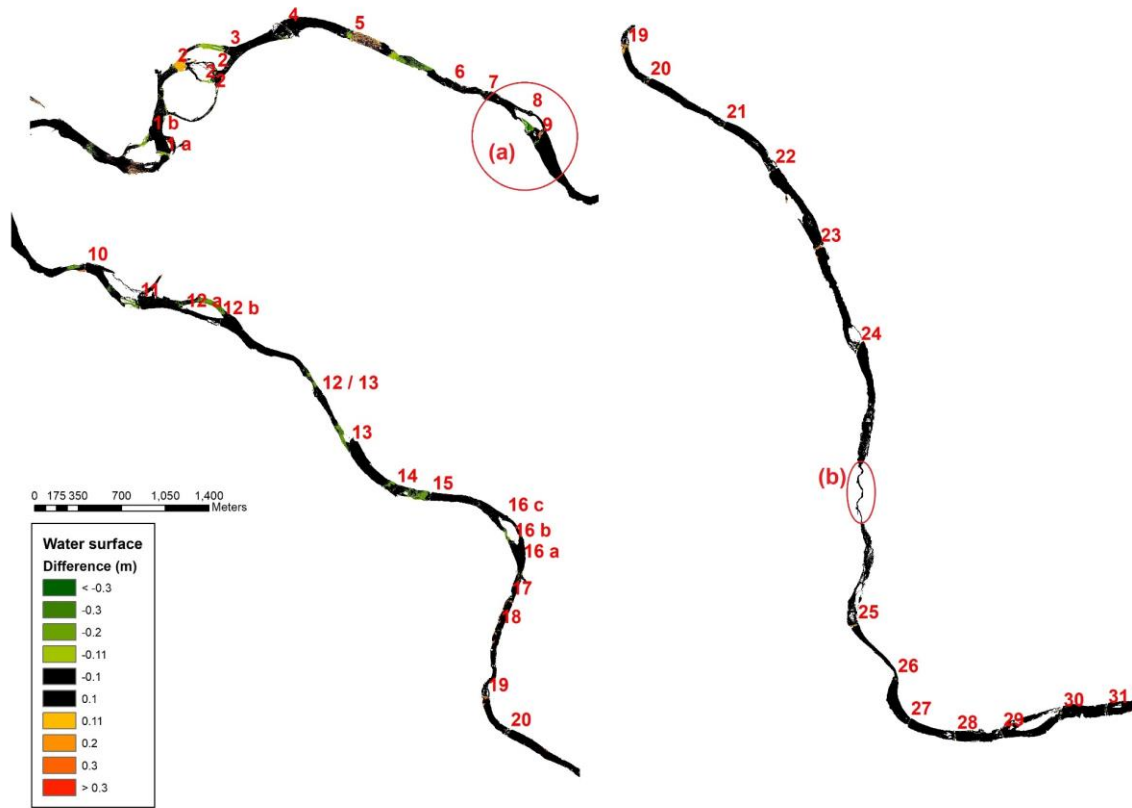


Figure 12: Calibration raster showing the difference between measured and simulated water surface. The black color represents areas where the difference is within the accepted boundary of ± 0.1 m. Two areas of interest are outlined where (a) is a problematic area around weir 9 and (b) show the calibrated LiDAR model of the artificial channel.

There were some problematic areas in the calibration process. Most of these areas were located on, or nearby a weir, indicating that the simulated flow over the weir was not completely accurate, some of these areas required a Manning's n value lower than $0.006 \text{ s/m}^{1/3}$ to come within the accepted boundary of error. A decision was made to keep the minimum Manning's value and accept that some of these areas did not accurately describe the actual flow events occurring in the river. Figure 13 show two areas of interest in the calibration raster. The left figure (a) shows the overrepresented errors downstream of weir 9, particularly in an artificial channel created just downstream of weir 9. This area was not successfully calibrated, containing cells with a difference in water surface up to 0.5 meters. The cause of this is not known, as the measured water surface in this area appears to be correct. However, due to the area's location downstream of Heggsetfoss power plant and the junction with Rotla, it is possible that the flow

over weir 9 is increased relative to the upstream river. The figure (b) shows the successful calibration of the LiDAR model at the location of the artificial channel also surveyed by UAV.

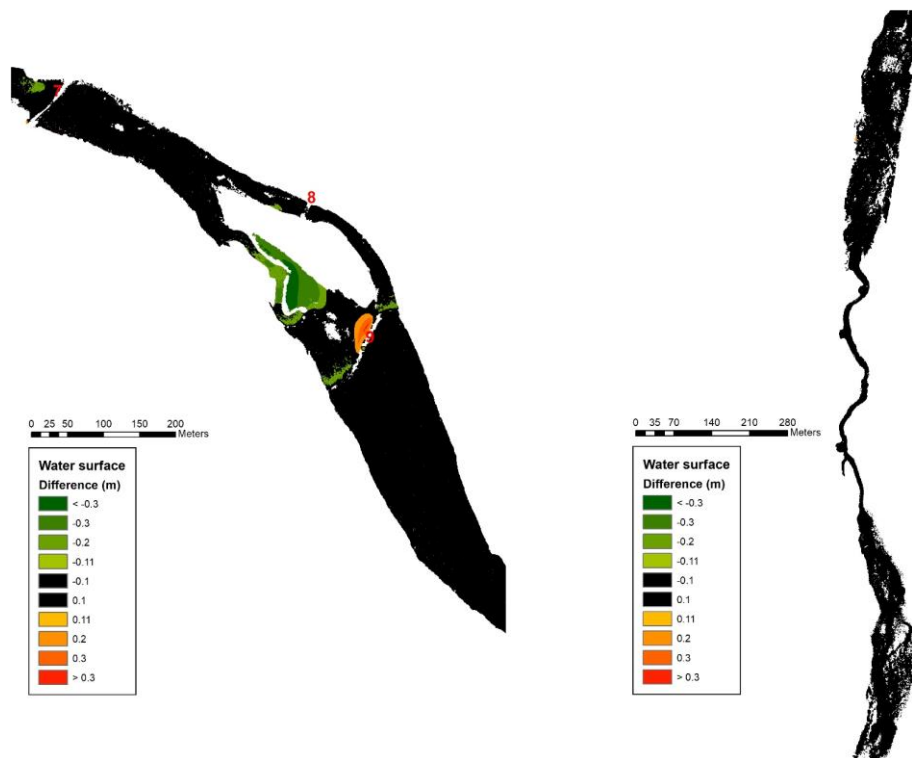


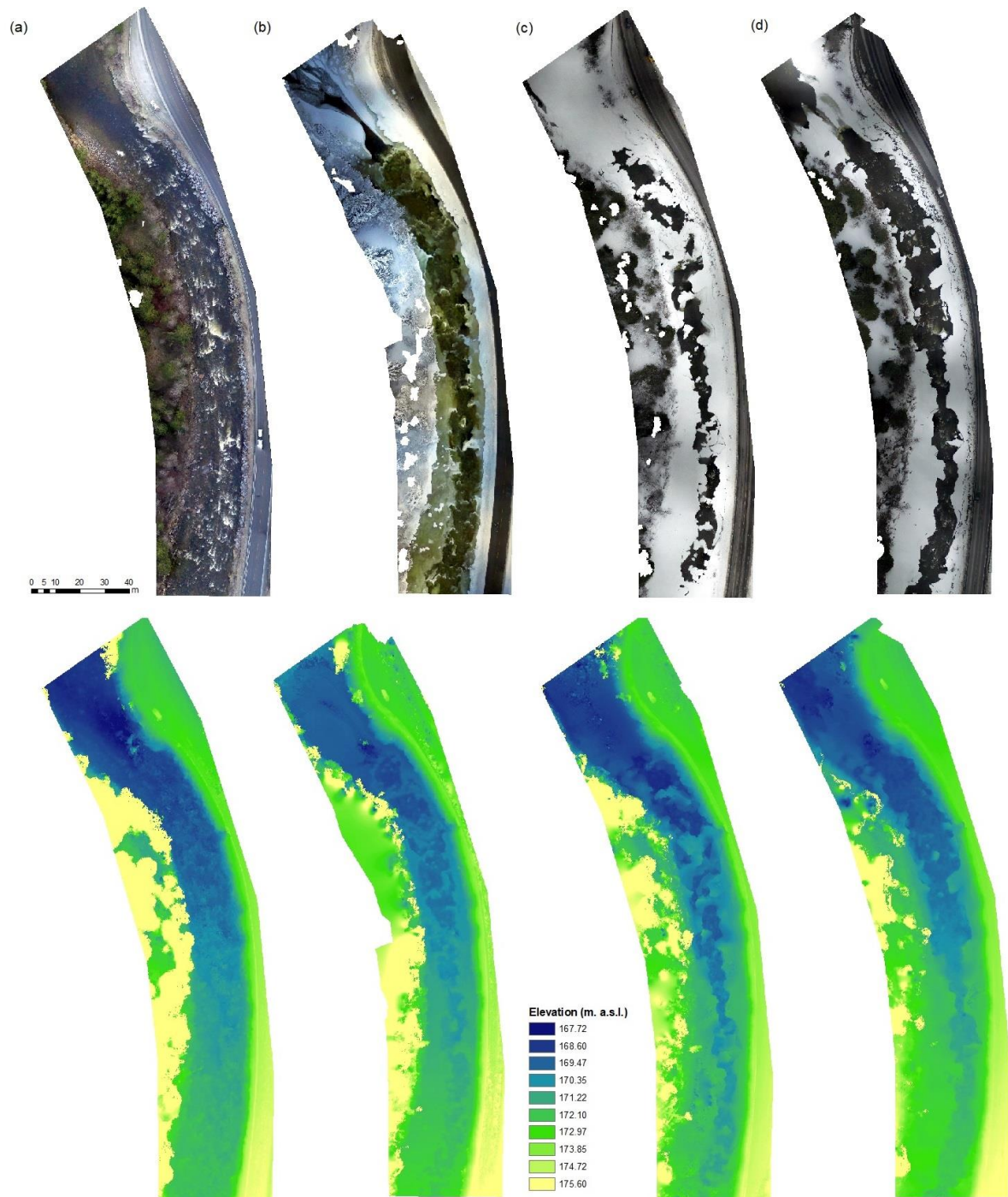
Figure 13: The two areas of interest marked in Figure 12. The left figure (a) show a problematic region in the calibration process in an artificial channel downstream of weir 9. The figure on the right (b) show the calibrated LiDAR based model for the artificial channel surveyed with UAV.

3.6 Mapping River Ice

The general SfM workflow described in chapter 3.3.2 were used to reconstruct DEMs and orthophotomosaics from aerial imagery collected at the Sokna site. Four UAV surveys were carried out between November 2018 and April 2019 and includes data for the river completely free of ice as well as formation and break-up of ice.

The area of interest is extracted from the orthomosaics and DEMs using a polygon boundary. A shapefile is created in ArcMap and a polygon boundary representing the area of interest is drawn in the shapefile. The ‘Data Management’ tool ‘Clip’ with the rasters set as input and shapefile set as ‘Output Extent’ will extract the area of interest from the raster. Due to the irregular shape of the polygon boundary the option to ‘Use Input Feature for Clipping

Geometry' is checked. If left unchecked the tool will use the minimum bounding rectangle area as clipping extent instead of the actual polygon boundary. This will produce orthomosaics and DEMs of the same area with identical boundaries, seen in Figure 14.



The cross-sections were created using the '3D Analyst' toolbar in ArcMap. Three cross-sections (A-A', B-B' and C-C') were manually drawn onto the rasters with the 'Interpolate Line' tool. Before drawing the cross-sections the correct layer representing each of the DEMs were chosen, keeping the orthomosaics displayed in the data viewer. This allowed for identification of different ice-formations which can be difficult to interpret from the DEMs. For each of the 3D lines representing cross-sections the 'Profile Graph' will generate the elevations over the distance from the bank. The cross-sections were drawn in the west to east direction, producing profiles graphs with the distance from the west bank on the x-axis.

Several methods for mapping river ice using tools available in ArcMap have been investigated, two of them presented. The first method calculates the total surface area and volume of the ice cover in Sokna using the '3D Analyst' tool 'Surface Volume'. The DEM of the three surveys with ice cover (January, March and April) were selected as the 'Input Surface' and output destination for the resulting textfile set. Using the 'Surface Difference' tool with the ice-cover DEMs as 'Input Surface' and the ice-free November surface set to reference surface. The rasters were already clipped to the same bounding region so the processing extent were the extent of the DEMs.

4 RESULTS

4.1 LiDAR Data Assessment

The quality control on the two LiDAR datasets consist of an evaluation of bathymetric coverage and vertical accuracy of the LiDAR measurements in the constructed DEM. The LiDAR data were evaluated using the ASPRS standards on required check point numbers. The bathymetric coverage is described by the point density (pts/m²) and point spacing (m) in the channel area.

4.1.1 Bathymetric coverage

The bathymetric coverage is found as the point spacing and point density in the channel area for both the 2018 and 2019 survey data. Table 2 shows the point spacing and point density in the channel area. The methodology used to extract the results allowed for some over-water ground points to be included, in particular areas close to the banks, the calculated point density is therefore considered as an upper boundary for the bathymetric coverage of the two datasets.

Table 2: Point spacing and point density in the channel area for the 2018 and 2019 LiDAR data.

LiDAR data	2018	2019
Point spacing (m)	0.76	0.37
Point density (pts/m ²)	1.72	7.47

Appendix B includes images of LiDAR points from the combined dataset on and around the weirs modeled with measures. All the weirs were covered in the data but some of the weirs have low coverage in the channel areas upstream. This introduced the need for assumptions of the riverbed elevation to be implemented in the model. The terrain used in the hydraulic model is built on the combination of the 2018 and 2019 LiDAR data, but as the combined data have several areas with overlapping points, the combined point density is considered as an unrealistic measure of bathymetric coverage.

4.1.2 Vertical Accuracy

The vertical accuracy assessment is summed up for the LiDAR point derived DEM in Table 3 and Separating the check-points measured on-land and in water as seen in Table 3 show that the check point with maximum absolute error is located above water, with a 41 cm difference from check point elevation and LiDAR DEM elevation. The maximum error for checkpoints

under water is 37.5 cm. The standard deviation for the check points above water is ± 19 cm, higher than the ± 15 cm seen for in comparison with under water check points.

Table 4. The for points under water, above water and the combination of these. Results are presented as the minimum- and maximum absolute error, the standard deviation, the mean average error and root mean square error on 171 measured check points. Figure 15 show the residuals for each of the seven check point groups, the locations of each group can be seen in appendix C.

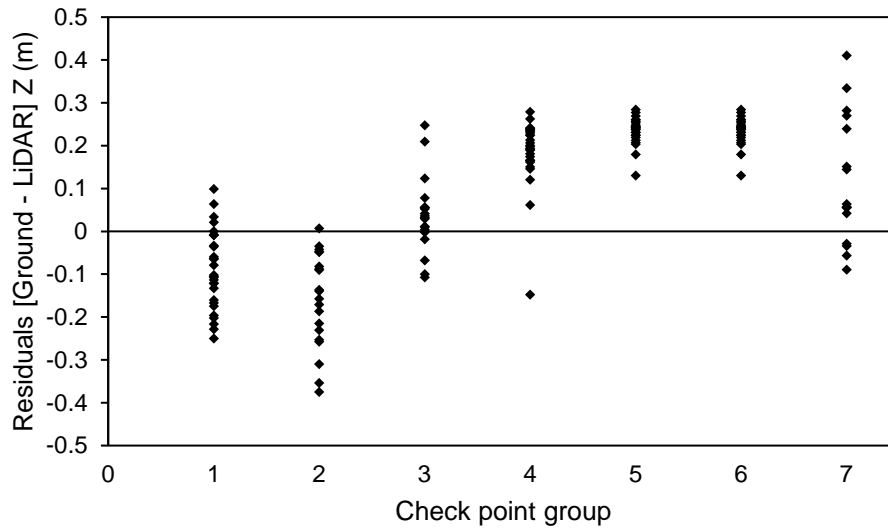


Figure 15: Elevation difference for compared LiDAR derived DEM and the seven groups of check points.

Table 3: Vertical accuracy of the LiDAR derived DEM compared to ground surveyed check points. Reported as the minimum and maximum absolute error, standard deviation, mean average and root mean square error for check points under water, on ground and the combination of these.

Check points	# of points No.	E_{\min} (cm)	E_{\max} (cm)	σ (cm)	E_{MA} (cm)	RMSE (cm)
Under water	68	0.06	37.50	14.88	11.00	14.18
Above water	103	1.35	41.03	19.02	10.74	18.93
Combined	171	0.06	41.03	17.25	14.74	17.20

Separating the check-points measured on-land and in water as seen in Table 3 show that the check point with maximum absolute error is located above water, with a 41 cm difference from check point elevation and LiDAR DEM elevation. The maximum error for checkpoints under

water is 37.5 cm. The standard deviation for the check points above water is ± 19 cm, higher than the ± 15 cm seen for in comparison with under water check points.

Table 4: Vertical accuracy of the LiDAR derived DEM compared to ground surveyed check points. Reported as the minimum and maximum absolute error, standard deviation, mean average and root mean square error for above water check points measured on grass and asphalt.

Check points	# of points No.	E_{\min} (cm)	E_{\max} (cm)	σ (cm)	E_{MA} (cm)	RMSE (cm)
Only grass	33	1.35	23.55	9.10	11.69	12.97
Only asphalt	59	4.26	28.45	21.13	20.03	20.95

Separating the above water check points into check points measured on grass and asphalt can be seen in Table 4. The standard deviation of 59 check points measured on the relative even surface of paved asphalt is ± 21.13 cm and the minimum absolute error is 4.26 cm. All the statistics show less accurate LiDAR data measured on grass than the asphalt road.

The LiDAR DEM elevations is compared with check point elevation is plotted in Figure 16- Figure 19 for the seven groups of check points including the regression line and R^2 value

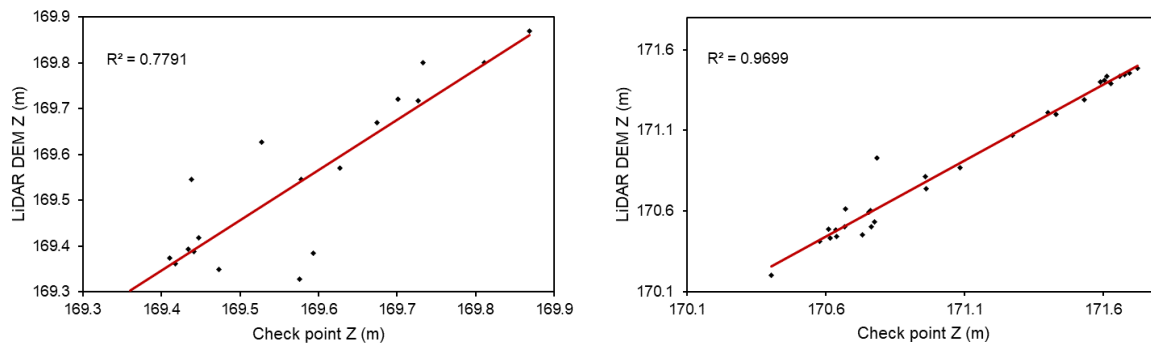


Figure 16: Measured Z values of check points in group 3 (under water) and 4 (grass), and Z values in LiDAR DEM at the corresponding location of each check point. Regression line is shown in red with the calculated value of determination coefficient for the regression line R^2 .

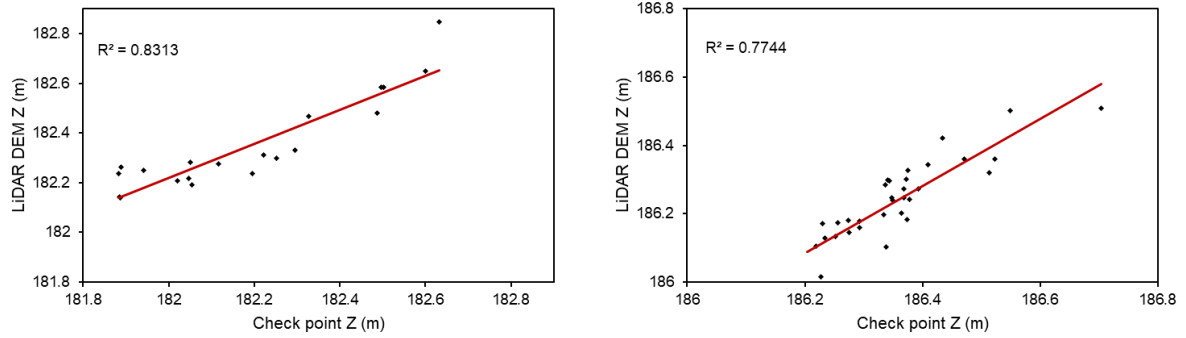


Figure 17: Measured Z values of check points in group 2 (under water) and 5 (grass), and Z values in LiDAR DEM at the corresponding location of each check point. Regression line is shown in red with the calculated value of R^2 .

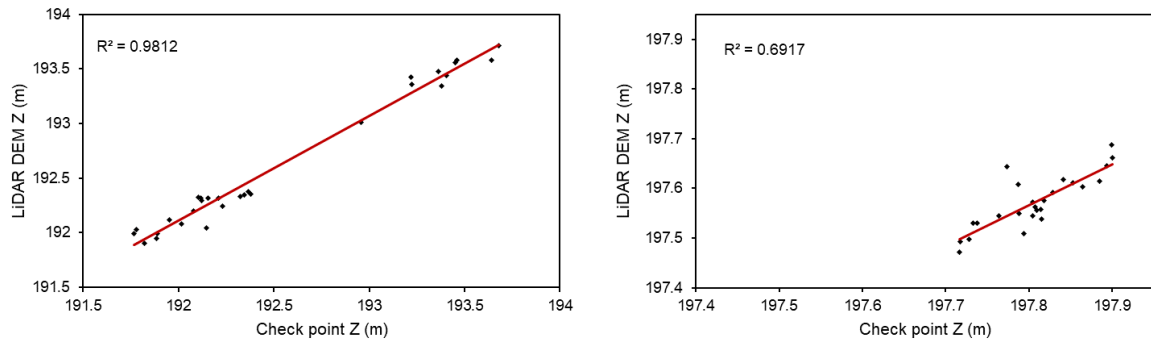


Figure 18: Measured Z values of check points in group 1 (under water) and 6 (asphalt), and Z values in LiDAR DEM at the corresponding location of each check point. Regression line is shown in red with the calculated value of R^2 .

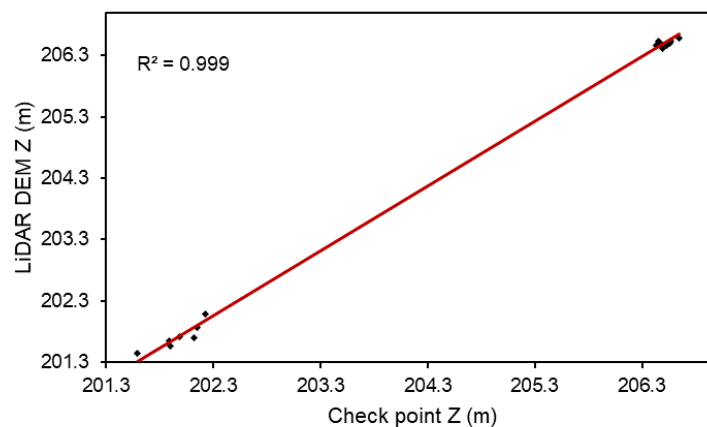


Figure 19: Measured Z values of check points in group 7 (asphalt, road barrier posts and rocks above water), and Z values in LiDAR DEM at the corresponding location of each check point. Regression line is shown in red with the calculated R^2 .

The discrepancy seen in the vertical accuracy is not what was expected prior to the vertical accuracy assessment. Looking at the Q-Q plots it can be seen that check point group 6 measured on asphalt (Figure 18) and check point group 5 on grass (Figure 17) both have large errors. When comparing group 5 to group 4, which is also grass (Figure 16) we see a check points on similar surfaces but with different accuracy.

4.2 Hydraulic Modeling of Nea

The following chapters presents the results from the hydraulic simulations in HEC-RAS. Three flow scenarios have been investigated, $1.5 \text{ m}^3/\text{s}$ corresponding to the required environmental flow during winter, $5 \text{ m}^3/\text{s}$ and $10 \text{ m}^3/\text{s}$. It is important to note that the results from the modeled weir measures is based on calculations without the possibility of control on the water surface elevation, while the simulations with today's weir situation is calibrated against a measured water surface elevation at a discharge of $1.5 \text{ m}^3/\text{s}$.

4.2.1 Calibrated model

Calibration of the hydraulic model have been conducted using a process of trial and error in the comparison between measured and simulated water surface. The results of the final calibration is shown as the mean, median and standard deviation of error in Table 5. The relative low mean and median error, and a standard deviation of 8 cm indicates that the calibrated model is within the accepted boundary of error. The boundary is set to $\pm 0.1 \text{ m}$ difference in order to account for potential errors in measurement when mapping the water surface with LiDAR and the naturally occurring variations in water surface due to waves or wind.

Table 5: Results from the comparison between measured and simulated water surface elevation after completing the calibration process.

Mean (m)	Median (m)	σ (m)
0.0144	0.0000	0.0798

The results presented in Table 5 is extracted from the calibration raster shown in Figure 12. All Manning's n regions used to calibrated can be seen in appendix D.

4.2.2 Water-covered area

The calculated water-covered area for the current situation and after implementing measures on the weirs can be seen in Table 6 for the three flow scenarios, for each weirs upstream area. The

increase in water-covered area for the different flow scenarios is shown in Table 5 as the percent difference going from 1.5 m³/s to 5 m³/s and 5 m³/s to 10 m³/s. Table 6 shows the reduction in water-covered area caused by implementing the measures on the weirs, for each of the flow scenarios. The basis for the calculations and visualization of the water-covered area for all the scenarios can be seen in the depth- and velocity rasters found in appendix E.

Table 6: Water-covered area in m² for the current situation and after implementing weir measures for the three simulation flows.

Weir	Current situation			Weir measures		
	Flow (m ³ /s)			Flow (m ³ /s)		
	1.5	5	10	1.5	5	10
32	41,774	43,971	44,920	38,981	43,360	44,654
29	46,980	55,231	57,546	41,766	52,329	56,945
28	28,585	30,619	31,817	25,020	27,860	29,831
27	24,311	25,530	26,240	21,724	24,175	25,554
24	33,908	35,501	36,542	29,461	34,110	35,894
23	54,462	61,060	64,829	50,381	59,474	64,063
22	62,190	66,782	68,476	54,128	63,354	67,352
21	36,180	38,882	40,110	33,977	37,872	39,459
9	63,997	66,293	68,234	58,356	62,440	65,035
6	31,642	39,455	45,073	30,635	38,132	43,340

Table 7: Difference in water-covered area shown as percent increase between 1.5 m³/s and 5 m³/s, and 5 m³/s and 10 m³/s, for the current situation and after implementing weir measures.

Weir	Current situation		After measures	
	Difference	Difference	Difference	Difference
	1.5 - 5 (%)	5 - 10 (%)	1.5 - 5 (%)	5 - 10 (%)
32	5.0	2.1	10.1	2.9
29	14.9	4.0	20.2	8.1
28	6.6	3.8	10.2	6.6
27	4.8	2.7	10.1	5.4
24	4.5	2.8	13.6	5.0
23	10.8	5.8	15.3	7.2
22	6.9	2.5	14.6	5.9
21	6.9	3.1	10.3	4.0
9	3.5	2.8	6.5	4.0
6	19.8	12.5	19.7	12.0

In Table 7 show the difference in water-covered areas for the flow scenarios in the model. The largest increase is seen 1.5 – 5 m³/s with close to 20% more wetted area between weir 6 and 9.

Table 8: The difference in water-covered area shown as the percent decrease between the current situation and the situation after implementing weir measures.

Weir	Difference at 1.5 m ³ /s (%)	Difference at 5 m ³ /s (%)	Difference at 10 m ³ /s (%)
32	6.7	1.4	0.6
29	11.1	5.3	1.0
28	12.5	9.0	6.2
27	10.6	5.3	2.6
24	13.1	3.9	1.8
23	7.5	2.6	1.2
22	13.0	5.1	1.6
21	6.1	2.6	1.6
9	8.8	5.8	4.7
6	3.2	3.4	3.8
Average	9.3	4.4	2.5

4.2.3 Velocity

The simulation results of the velocities in the upstream areas of each weir is shown as the average velocities in Table 9. The average velocity in each section is not significantly changed in the model with weir measures due to the relatively large area. The results from the 1.5 m³/s flow show an increase in the average velocity in the weir-pool for all but weir 28, 23 and 22. Simulations with a flow of 5 m³/s and 10 m³/s show an increase in the average velocity for six of the ten weirs.

Table 9: Average velocity (m/s) in the area upstream of each weir, to the next encountering weir.

Weir	Current situation			After measures		
	Flow (m ³ /s)			Flow (m ³ /s)		
	1.5	5	10	1.5	5	10
32	0.24	0.43	0.61	0.25	0.44	0.61
29	0.19	0.31	0.43	0.20	0.32	0.43
28	0.21	0.36	0.49	0.19	0.34	0.47
27	0.26	0.48	0.66	0.27	0.45	0.61
24	0.17	0.32	0.45	0.19	0.32	0.45
23	0.17	0.30	0.42	0.16	0.28	0.39
22	0.14	0.25	0.36	0.13	0.24	0.35
21	0.20	0.38	0.53	0.20	0.38	0.53
9	0.25	0.47	0.67	0.27	0.49	0.69
6	0.53	0.90	1.18	0.56	0.93	1.20

The distribution of water velocities for each flow, in the current situation and after implementing the measures is presented in Figure 20 - Figure 22. The areas on and around the weir has the largest differences in the current and after situation with a typical increase in velocity at the location of the measure. For the rest of the area the water velocity is slightly reduced, but as the proportion of these areas is significantly larger than the area on and around the weir, they amount to a reduced average velocity in the upstream reaches. This effect is best seen on the velocity rasters shown in appendix F.

For the minimum flow scenario of 1.5 m³/s there is a decrease of 4% in the lowest range of velocities (0 – 0.05 m/s) while the proportion of areas with a velocity between 0.1 and 0.2 m/s is increased by 4%. The proportion of areas with a velocity over 0.5 m/s is primarily located in the areas where the weirs is lowered. Looking at all the weir-pools included in these results the modification of weirs will not have significant impact on the average velocity combined. The average velocity for the flow of 1.5 m³/s is 0.24 m/s before and after implementing the measures. The average velocity for the flow of 5 m³/s is 0.42 m/s before and after implementing the measures. The average velocity for the flow of 10 m³/s is 0.58 m/s for the current situation and 0.57 m/s in the situation with measures.

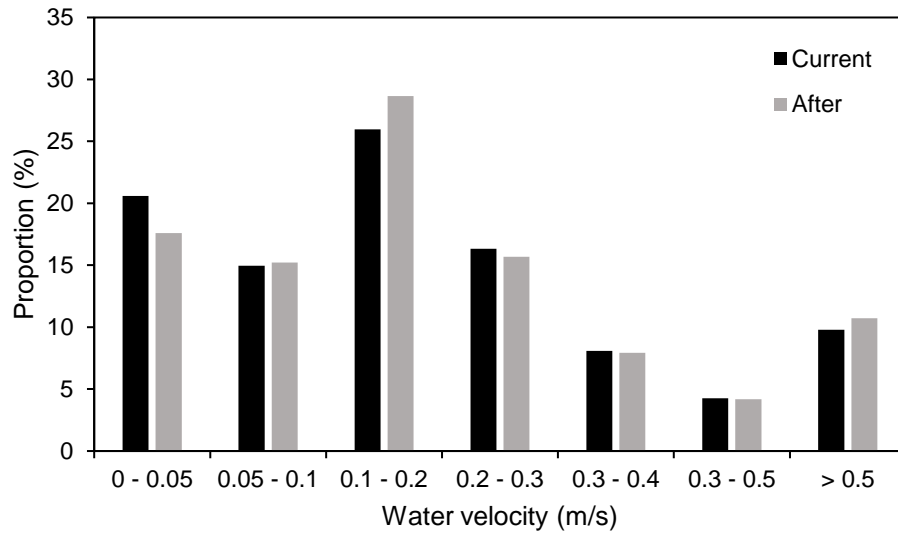


Figure 20: Distribution of velocities for all the areas upstream of weirs with implemented measures for a flow of $1.5 \text{ m}^3/\text{s}$.

In the $5 \text{ m}^3/\text{s}$ flow scenario the situation after implementing weir measures follows the same pattern as for the minimum flow scenario. The proportion of the lowest ranges of velocities is decreased while the proportions of the highest velocities in the area is increased, and mainly resides on the weir.

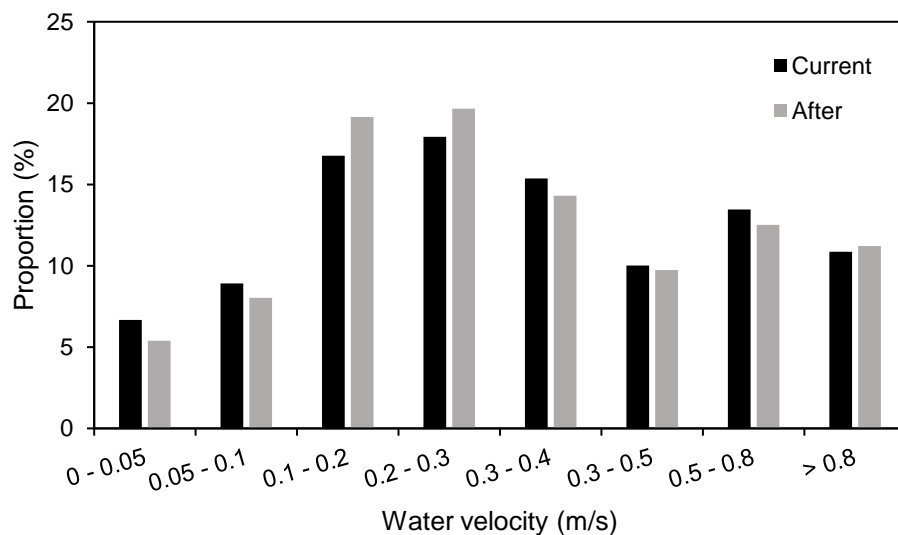


Figure 21: Distribution of velocities for all the areas upstream of weirs with implemented measures for a flow of $5 \text{ m}^3/\text{s}$.

In the highest flow scenario ($10 \text{ m}^3/\text{s}$) the distribution of water velocities is less influenced by the measures on the weirs. For the velocities between 0.1 m/s and 0.3 m/s there is a 1% increase

in the situation after implementing the measures, while there is a 1% decrease in both the 0.5 m/s to 0.8 m/s and 0.8 m/s to 1 m/s. As the tables in appendix F show, the weir-pool of weir 27 is most affected by the measures.

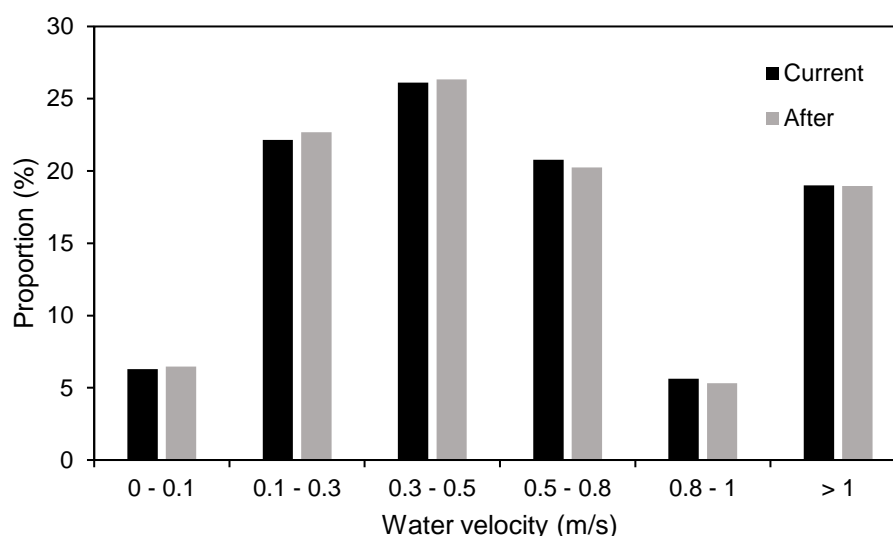


Figure 22: Distribution of velocities for all the areas upstream of weirs with implemented measures for a flow of 10 m³/s.

4.2.4 Depth

Table 10 presents the average depth in the upstream reaches of each weir, in the current situation and after implementing the measures on the weirs. The values are extracted from the simulation results for the depth shown as rasters. For all the weirs the average depth decreases after implementing the measures. The reduction in depth is most prominent in the upstream area of weir 9 with a reduction in average depth of 31% for a flow of 1.5 m³/s, 22% for a flow of 5 m³/s and 18 % for a flow of 10 m³/s. Weir 9 also has the largest upstream area of all the modeled weirs.

Table 10: Average depth (m) in the weir-pool upstream of each weir, to the next encountering weir.

Weir	Current situation			After measures		
	Flow (m ³ /s)			Flow (m ³ /s)		
	1.5	5	10	1.5	5	10
32	0.23	0.32	0.40	0.20	0.28	0.37
29	0.32	0.34	0.40	0.27	0.33	0.38
28	0.31	0.35	0.39	0.20	0.27	0.34
27	0.41	0.45	0.49	0.27	0.37	0.44
24	0.54	0.58	0.62	0.39	0.53	0.59
23	0.26	0.36	0.46	0.24	0.35	0.45
22	0.30	0.37	0.44	0.27	0.33	0.41
21	0.49	0.52	0.57	0.47	0.50	0.55
9	0.61	0.64	0.67	0.42	0.50	0.55
6	0.37	0.35	0.34	0.35	0.34	0.34

The distribution of depth for the lowest flow scenario is seen in Figure 23. There is a significant decrease of areas deeper than 0.5 m in the situation with measures, increasing areas with depths of 0.1-0.3 m.

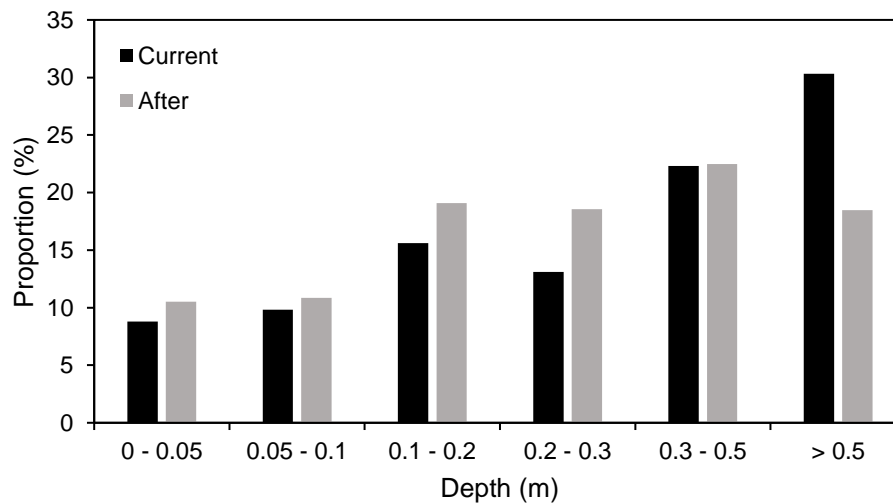


Figure 23: Distribution of depth for all the areas upstream of weirs with implemented measures for a flow of 1.5 m³/s.

The distribution of depth for the 5 m³/s and 10 m³/s have to some similar distributions seen as seen in Figure 24 and Figure 25. The 5 m³/s flow will however loose more areas with depths

over 0.5 m after implementing the weir measures, with the proportion of these areas reduced from 34% to 27%. For the flow of 10 m³/s the areas proportion of areas deeper than 0.5 m is reduced from 44 % to 39%.

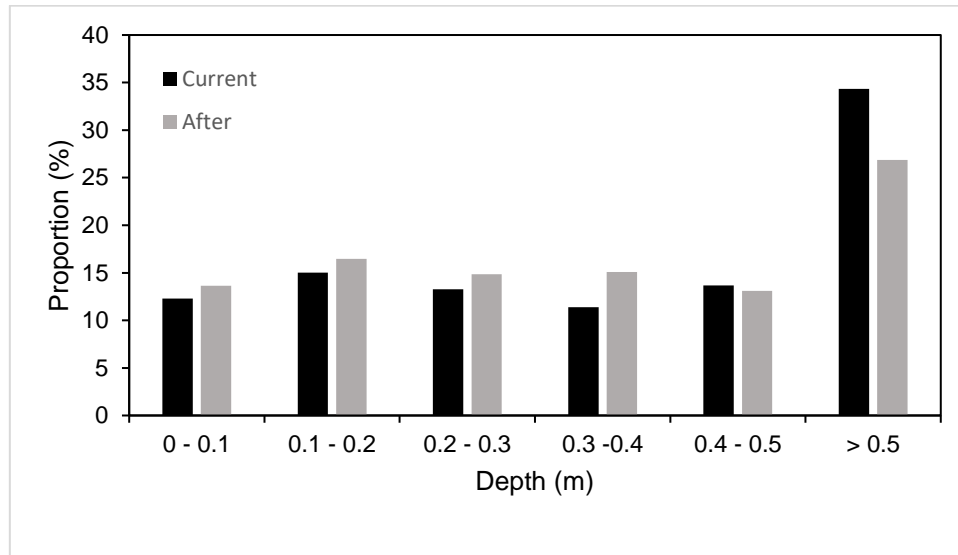


Figure 24: Distribution of depth for all the weir-pool upstream of weirs with implemented measures for a flow of 5 m³/s.

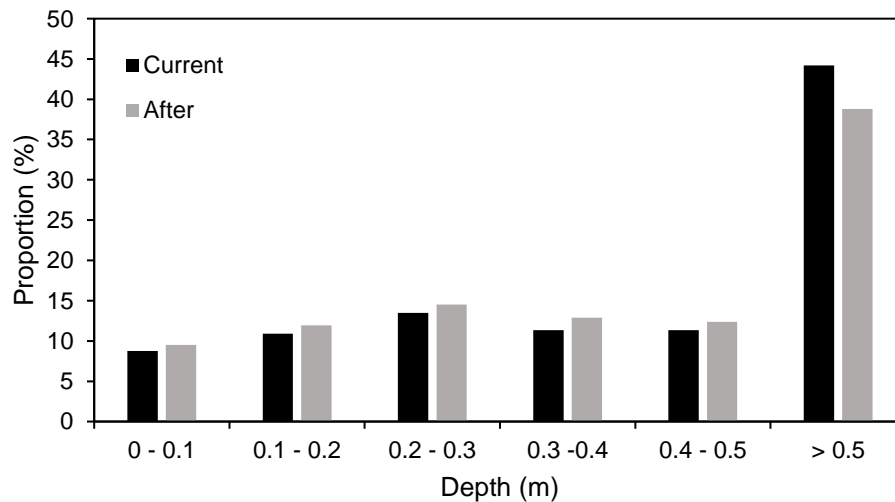


Figure 25: Distribution of depth for all the weir-pool upstream of weirs with implemented measures for a flow of 10 m³/s.

4.2.5 Artificial channel

The artificial channel between weir 24 and 25 in Nea were surveyed by UAV on 11 September 2018. The reconstructed orthomosaic and DEM from UAV images can be seen in Figure 26. The model accuracy is presented as the combined RMSE on control points and check points in Table 11. During the UAV survey the GCP measuring GNSS equipment was unable to measure the markers placed in the study area. The model is georeferenced with GCPs collected at a later time, using road markings and large rocks as GCPs. Five of the GCPs were excluded as they produced large errors in the models due to few reprojections.

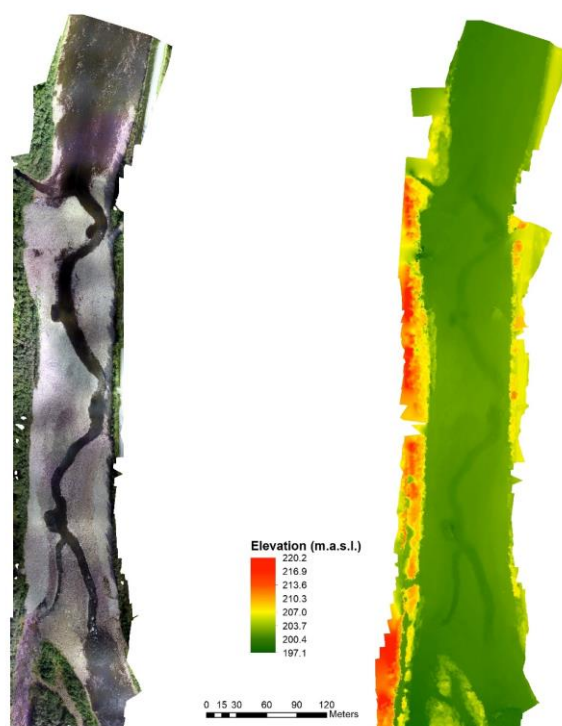


Figure 26: Orthophotomosaic and DEM reconstructed from the UAV survey data for the artificial channel.

Table 11: The accuracy in models reconstructed from UAV topographic data in Nea. The combined RMSE is shown for 7 control points and 4 check points.

Measurement	No. of points	Mean RMSE combined (m)	Min RMSE combined (m)	Max RMSE combined (m)	Long. (m)	Lat. (m)	Alt. (m)
Control points	7	0.175	0.086	0.336	0.090	0.056	0.139
Check points	4	0.212	0.124	0.268	0.090	0.096	0.168

The 1 m-resolution national DTM from hoydedata is used as reference for the UAV model. The elevation differences when comparing the two models is shown in Figure 27. The analyst tool 'Minus' were used to subtract the elevations in the UAV model from the reference.

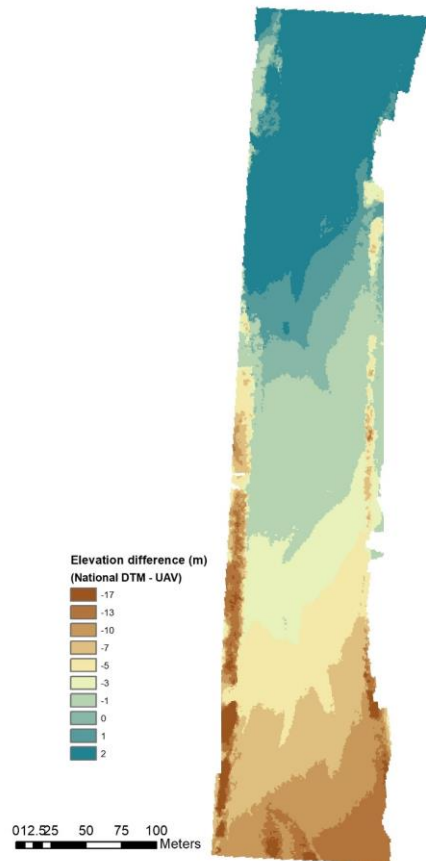


Figure 27: Elevation differences (m) comparing the reference DTM (1m) from hoydedata.no and the UAV derived DEM.

The DEM from the UAV topographic survey show large residuals in the upstream area, with errors up to 17 m. In the center area where most of the GCPs are located the differences is reduced. The model is not a good representation from the UAV images and the river gradient in the model is exaggerated causing unnatural flow scenarios when used in hydraulic modelling. The GCPs for this model was collected after the topographic survey were located primarily in the center channel area and on road markings.

The results from the hydraulic model on the UAV based can be seen in Figure 28 for the three flow scenarios. The DEM from the UAV data have large errors in the upstream parts and the river gradient is exaggerated causing flooding in the model area.

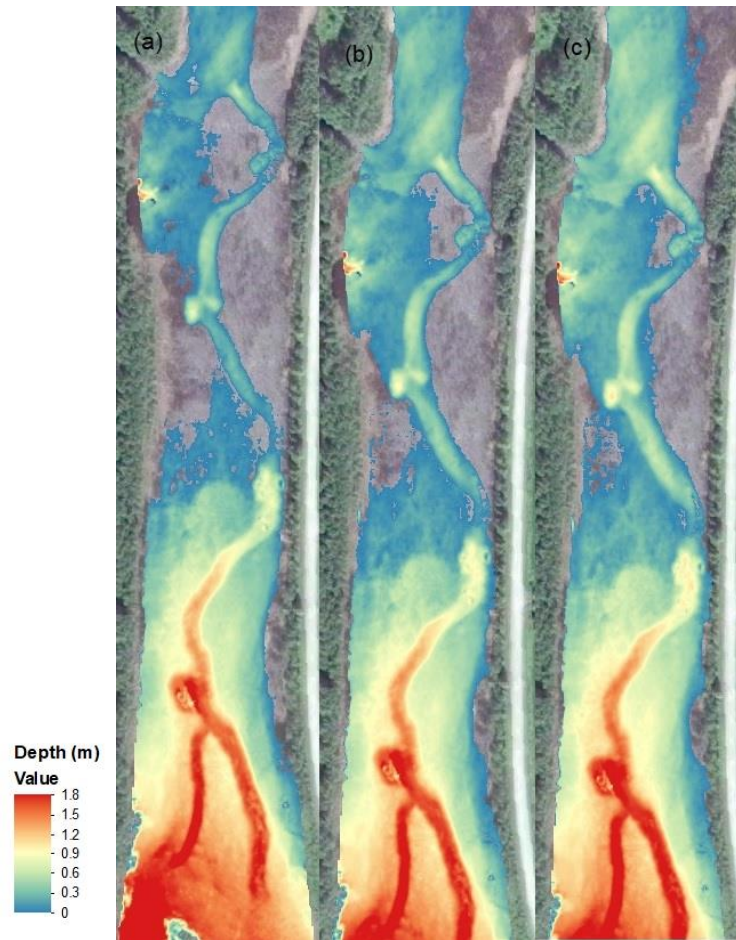


Figure 28: Water depth (m) from the simulations in the artificial channel in Nea on the UAV derived DEM, with a flow of (a) $1.5 \text{ m}^3/\text{s}$, (b) $5 \text{ m}^3/\text{s}$ and (c) $10 \text{ m}^3/\text{s}$.

The simulation results from the hydraulic model on the LiDAR based terrain model for the three different flow scenarios is presented in Figure 29. The minimum flow scenario of $1.5 \text{ m}^3/\text{s}$ show the principle of the environmental design concept of an artificial channel, where the flow is concentrated in the constructed channel, increasing depth and velocity. Simulations with the highest flow scenario in the model ($10 \text{ m}^3/\text{s}$) have flooding starting to occur at the entrance of the channel and flooding of the downstream constructed pool.

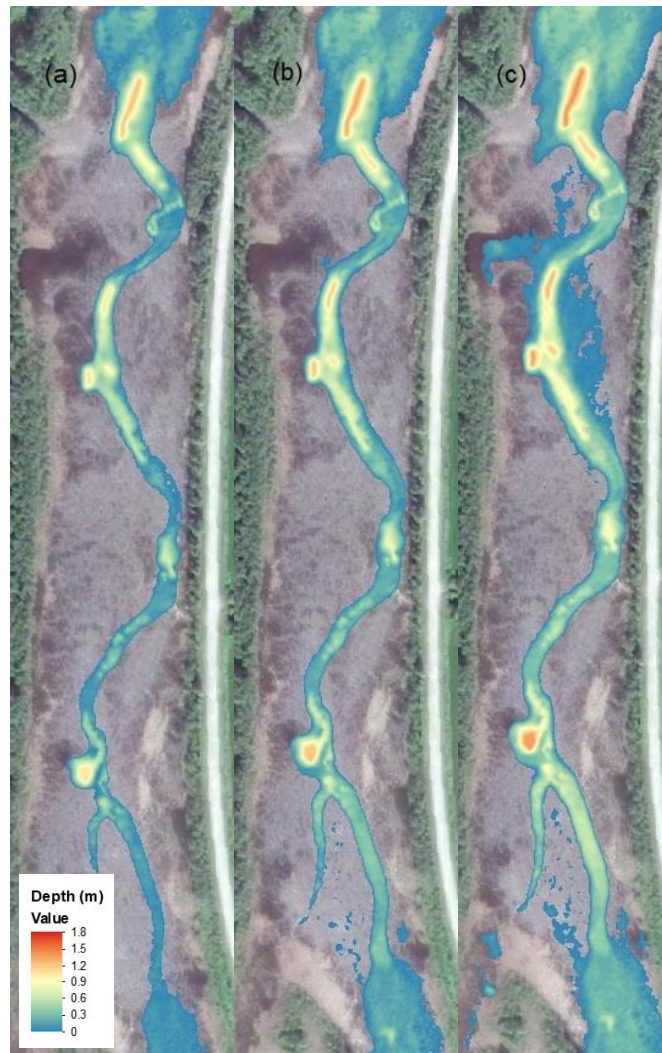


Figure 29: Water depth (m) from the simulations in the artificial channel in Nea on the LiDAR derived DEM, with a flow of (a) $1.5 \text{ m}^3/\text{s}$, (b) $5 \text{ m}^3/\text{s}$ and (c) $10 \text{ m}^3/\text{s}$.

4.3 Mapping River Ice in Sokna

The DEM and orthomosaic reconstructed from the survey data of Sokna is the basis for the analyses on river ice. The accuracy of each model is seen in Table 12 as the combined RMSE on control points and check points. Based on the low RMSE seen here the models of Sokna is considered to have a high accuracy. The orthophotos from the surveys seen in Figure 30 show the ice-free geometry in the November data and anchor ice has started to form in January. In March there is fully developed anchor ice dams and some break-ups can be seen. The April orthophoto show the ice cover deteriorating, anchor ice dams are still present in the upstream areas.

Table 12: Root mean square error on 7 control points and 3 check points for each of the UAV survey dates. The error is reported as the combination of x, y and z.

Survey date	Control points			Check points		
	Mean RMSE combined (m)	Min RMSE combined (m)	Max RMSE combined (m)	Mean RMSE combined (m)	Min RMSE combined (m)	Max RMSE combined (m)
7 Novemeber 2018	0.077	0.048	0.104	0.070	0.017	0.093
25 January 2019	0.039	0.022	0.045	0.045	0.040	0.050
13 March 2019	0.064	0.029	0.101	0.045	0.039	0.052
2 April 2019	0.041	0.012	0.066	0.087	0.032	0.109

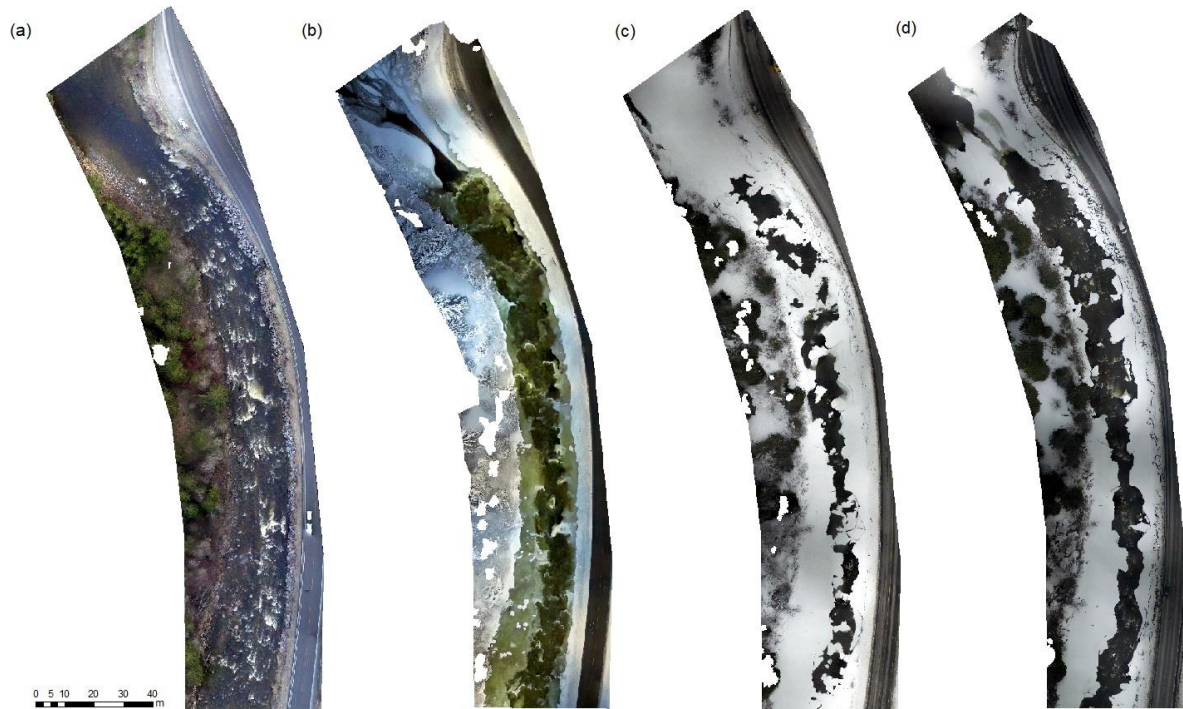


Figure 30: Orthophotos from the four UAV surveys in Sokna

The reconstructed DEMs from the survey data collected in Sokna is used to find the spatial extent of the river ice in Sokna as it develops over the winter. The 3D analyst tools available in ArcMap described in chapter 3.6 is used to find the surface area and volume of the ice with the ice-free river geometry in the November model as a reference. The two approaches produced results with a relative error within $\pm 5\%$. The surface area and volume are summarized in Table 13 as the mean estimated by the tools in ArcMap.

Table 13: Surface area (m^2) and volume (m^3) of the river ice in Sokna for the three models including ice.

Date	Surface area (m^2)	Volume (m^3)
25 January	1,867	1,976
13 March	4,170	8,693
2 April	3,314	6,265

The orthophotos from the four surveys are used to locate ice processes and cross-sections are used to extract elevation profiles at areas of interest. Figure 31 show the orthophoto from the 13 March survey data and three cross-sections used to extract elevations in the DEM from the riverbank.



Figure 31: Orthophoto from the March survey data showing three cross sections, A-A', B-B' and C-C' in the Sokna site.

The elevation data extracted for cross-section C-C' in all of the DEMs can be seen in Figure 32. Cross-section shows the development of an ice jam event in a location with anchor ice dam present in the January model. The elevation data is also extracted from the national 1m resolution DTM as seen in Figure 33.

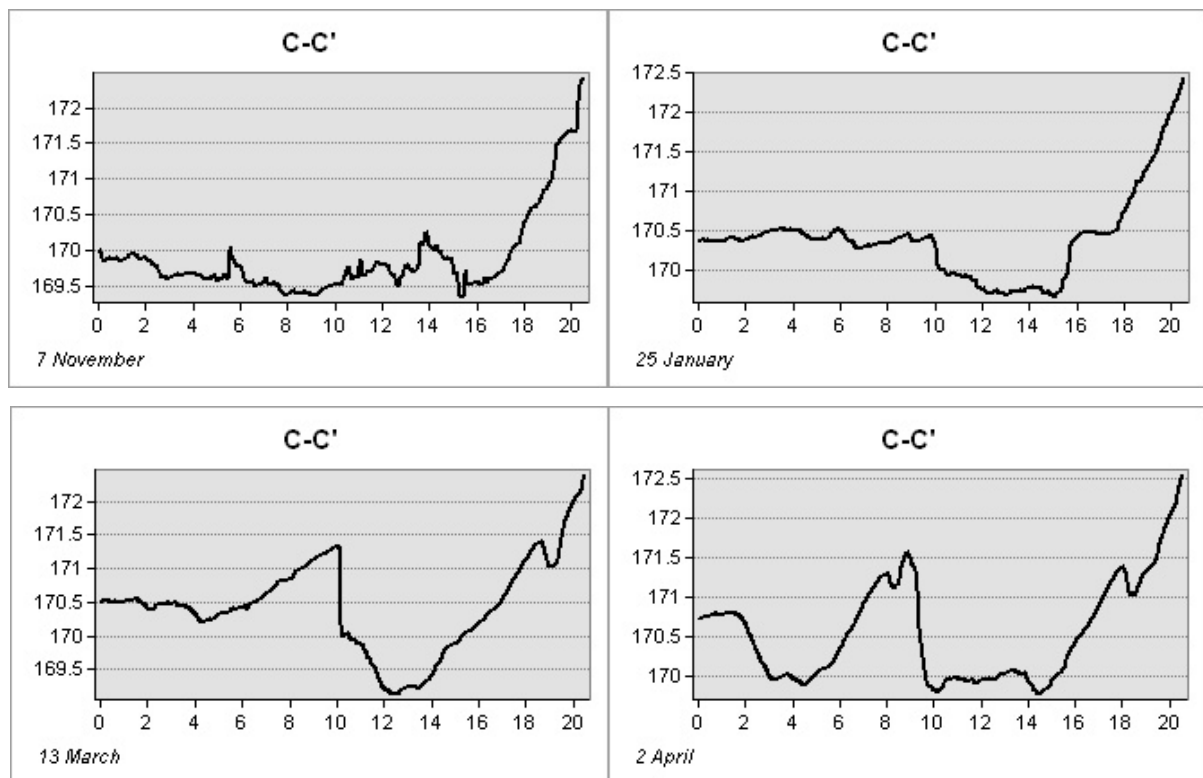


Figure 32: Profile graphs for cross-section C-C' extracted from Sokna DEMs showing elevation and distance from left bank.

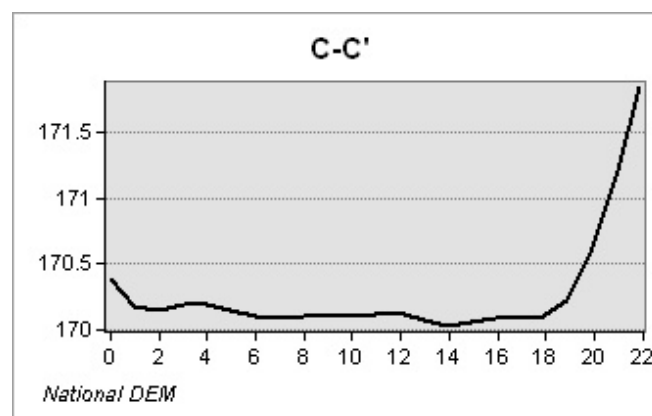


Figure 33: Profile graph for cross-section C-C' extracted from the national 1m resolution DTM (hoydedata.no).

The cross-sections show the formation of ice starting in January in a location with large rocks on the riverbed, a likely place for anchor ice to form. The March model captures the ice-jam in

this narrow part of the river, where sheets of ice have collided, pressing sheets of ice over another, increasing total height of the ice. The April data show the deteriorating ice on the left bank with anchor ice still adhering to the large rocks in the river. The profile graphs for cross-section A-A' and B-B' are presented in appendix G.

5 DISCUSSION

This study evaluated two sets of data from surveys in Nea using airborne LiDAR. The bathymetric coverage is found as the point density in the channel area, giving a measure of the surveys ability to map underwater topography. The vertical accuracy of the supplied data is evaluated by comparing the reconstructed DEM to check points measured with differential GNSS. These measures give an indication of the overall quality of the LiDAR data and its ability to serve as a basis for the hydraulic model. The point density of the 2019 survey is estimated to be 7.47 pts/m² but areas around weirs investigated did have no coverage in the nearby upstream and downstream areas, requiring assumptions of the riverbed elevations to be made. The hydraulic effects of measures on nine of the weirs in Nea were examined using a two-dimensional model HEC-RAS based on the LiDAR data. Three flow scenarios were simulated on the LiDAR derived terrain and on the modified terrain where small sections on the weirs were lowered. The simulation results show the effect of the measures on hydraulic conditions in the river, including water-covered area, velocities and depth. Airborne LiDAR surveys is able to efficiently map large areas, where traditional ground surveying methods would prove undesirable due to the size of the study area. Hydraulic modelling on the basis of LiDAR data have a wide range of application such as studying river morphology, habitat areas and hydraulic factors linked to fish migration.

5.1 LiDAR Data Assessment

The bathymetric coverage estimated for the two LIDAR datasets is based on the approach presented in chapter 3.2. This method uses a manually drawn polygon to estimate the channel area, used to locate bathymetric LiDAR points. When locating these points with a polygon like this, some over-water terrain points close to the channel or in the channel area will be counted as points on the riverbed. This method will probably produce results which are to be considered as an optimistic value.

The 2018 LiDAR survey is estimated to have a point-density in the channel area of 1.72 pts/m². Visually inspecting the LiDAR point-cloud in ArcMap to see large channel areas without any LiDAR points and compared to previous work in other studies, reaching point densities of 20-40 pts/m² indicates that this LiDAR data have poor under-water coverage. Many factors contribute to LiDAR sensors under-water mapping abilities, weather conditions, flying altitude of the survey aircraft, and conditions in the water. The weather conditions during this survey is

considered good, the orthophotos reveal some dark areas in the water which may affect the penetration depth of the LiDAR beam. It is possible that the flying altitude of the aircraft during this survey affected the under-water mapping ability of the sensor. Building terrain models from the 2018 LiDAR data were challenging due to the many areas with no measurements. The 2019 LiDAR data delivered in May 2019 have an estimated bathymetric coverage of 7.47 pts/m². The conditions during this survey included ice in the river, ice on the surface is not ideal conditions these areas require manual post-processing for mapping bathymetry. The 2019 data provided LiDAR points in areas where the 2018 data had no measurements and increased the point density in the channel are by a factor of four. However, compared to similar projects the point density of the 2019 LiDAR data is still considered as low.

The comparison of the LiDAR DEM and check points to evaluate vertical accuracy in the LiDAR data presented in chapter 4.1.2 show a lower vertical accuracy for LiDAR points on asphalt than on grass or under water. It was assumed that the vertical accuracy of points measured on a stable and even surface like asphalt would have higher vertical accuracy than points measured under water and in grass. The RMSE of error when comparing measurements on asphalt is 21 cm. The low accuracy seen in the vertical accuracy on asphalt surfaces is hard to explain, Table 3 separates the check points measured on-land and under water and show a higher vertical accuracy for topographic points than when comparing bathymetric points. The measurements in water was assumed to have a lower accuracy due to the potential for a check point to be measured between rocks on the riverbed while the LiDAR pulse is reflected on the surface of the rock, measuring different elevations for the same position. The vertical accuracy assessment used the combined dataset of the two LiDAR surveys were a possible source to discrepancies, as the interpolation included LiDAR points for both surveys.

5.2 Hydraulic Modelling of Nea

There are several methods to choose from when constructing a DEM from a LiDAR point cloud in ArcMap. In this study the tool ‘LAS Dataset to Raster’ were used in creating the elevation model of Nea. This tool offers four different approaches for doing this, with two different interpolation techniques (binning and triangulation) and three methods (average, inverse distance weighing and closest neighbor). In the early work of this study the 2018 LiDAR data was used to construct a DEM primarily using the ‘Binning’ interpolation, due its slightly shorter processing time. All the methods tested produced similar models with model artefacts in the same locations. In the final model the method of applying surface constraints using break lines in ArcMap were applied. This method requires the terrain to be created through triangulation,

hence the triangulation method was chosen as the interpolation type. Applying break lines as surface constraints, estimating the riverbed elevation from the surrounding terrain and aerial images serves as a reasonable method for manipulating the interpolation in areas with no LiDAR measurements.

The process of calibrating the hydraulic model required manipulating the terrain model where the interpolation between LiDAR points gave unnatural elevations causing dry areas in unlikely places. The calibration process used the LiDAR measured water surface from the 2018 survey as reference. Based on observations from the survey date a flow of $1.5 \text{ m}^3/\text{s}$ was estimated that day. The recorded flow at the gauge at Kulset bru was $32.35 \text{ m}^3/\text{s}$. The weirs of interest in this study is upstream of Kulset bru and Nedre Nea power plant and a flow of $1.5 \text{ m}^3/\text{s}$ is assumed for this part of the river. The comparison between the simulated water surface and the measured water surface included a visual inspection in RAS Mapper, hovering over areas to read out the elevation. This method was efficient in a rough calibration of the model. A more detailed approach for fine-tuning particular areas included analyses of the simulation results in ArcMap. A raster for the LiDAR measured water surface was created and the simulation results imported to ArcMap. Using the 'Minus' tool with the measured and simulated water surface as input provided an efficient way of visualizing the difference between the measured and simulated results. Natural fluctuations in the water surface due to winds or waves, and the potential error in measurement in the LiDAR data was considered when selecting the maximum allowed difference of ± 0.1 meter. The Manning's n value will typically be increased in areas where the simulated water surface is below the measured and decreased in areas where simulated water surface is above. It is not desirable to apply unrealistic roughness values to the model. Some areas were problematic to calibrate without using a Manning's n value below $0.006 \text{ s/m}^{1/3}$. Manning's n value as low as this is not probable to occur in a natural river as it is close to the roughness of surfaces like glass. However, as the model setup in HEC-RAS do not account for processes such as infiltration, some areas required Manning's n values as low as $0.006 \text{ s/m}^{1/3}$ to transport the water rapidly. Areas with riffles was often problematic, but these areas are prone to local variations due to waves and large rocks and will often not have an even surface. Areas of pools on the river would many times fall within the accepted boundaries of error using the default Manning's n value of $0.03 \text{ s/m}^{1/3}$.

The process of calibrating the hydraulic model started prior to the 2019 LiDAR data being available, using only data from the 2018 survey to create the underlying terrain. This dataset has a point density in the channel are of 1.72 pts/m^2 which is a relative low average density for

mapping the underwater topography. The calibration process was initiated using the unaltered terrain data created from the 2018 LiDAR point cloud and this proved to be a time-consuming and problematic task. The interpolation techniques used in the process of creating the terrain raster in ArcMap created areas with unrealistic topography. These areas were typically located where there were no LiDAR points of the bathymetry or very few sparsely located in the channel, resulting in interpolation between the over-water riverbanks over the entire channel width. The calibration process of adding regions with specific Manning's n values required the use of unrealistic values, with some areas reaching a Manning's n value as low as $0.001 \text{ s/m}^{1/3}$ while still not coming within the accepted boundaries of error on water-surface elevation.

The 2019 LiDAR data was delivered in early May with an estimated point density in channel areas of 7.47 pts/m^2 . The final terrain used in the hydraulic simulations were created from the combined point cloud of the 2018 and 2019 LiDAR survey. The combined dataset still had areas with no LiDAR measurements and the interpolation created unnatural depiction of the bathymetry. The method chosen for adding more realistic assumptions of the riverbed was found, using break lines with elevations estimated from orthophotos captured during the survey and satellite images. This improved the terrain model making the calibration process faster and resulting in the parameter (Manning's n) more natural. Calibration of the model was completed using the assumption of a flow of $1.5 \text{ m}^3/\text{s}$, corresponding to the required environmental flow and the measured water-surface from the 2018 LiDAR survey. The Manning's n regions used in the model were in the range of 0.006 to $0.08 \text{ s/m}^{1/3}$.

A weakness in the calibration is the uncertainty of the actual flow along the relative long reach. There are several tributaries between Heggsetdam and Nedre Nea power plant, providing additional inflow of water along the way. The environmental flow of $1.5 \text{ m}^3/\text{s}$ was assumed for the reach from Heggsetdam to the intersection with Rotla but it is likely that the flow is increased after Heggsettfoss power plant. Manual measurements of the water surface during the airborne survey, spread out along the river would provide a more accurate foundation for the calibration process. The two remaining simulation flows ($5 \text{ m}^3/\text{s}$ and $10 \text{ m}^3/\text{s}$) is not included in the calibration as there is no calibration data available for these flow scenarios. It is probably reasonable to assume that the relatively small increase will not significant impact model results. The reference water surface is measured by LiDAR which also introduces errors on measurements and risk of human error in the post processing of data.

Kulset bru gauge is downstream of the outlet of Nedre Nea and data for the water level or discharge is available from NVE. From Figure 3 we can see the percentiles and how its kept

relative stable in the winter and spring season. Assuming the recorded flow at Kulset bru on the day of surveying ($32.35 \text{ m}^3/\text{s}$) can be linked to the upstream reach of Nedre Nea, it is reasonable to assume that flow values ranging from $1.5 \text{ m}^3/\text{s}$ to $10 \text{ m}^3/\text{s}$ is very likely in that period.

The hydraulic simulations used the diffusive shallow wave approach as it can remove some of the problems that can occur with diffusion, causing the model to become unstable and efficiency in longer simulations. For river systems mainly driven by the force of gravity and friction on surface, the DSW equations is preferable.

There are several contributing factors when deciding the cell size for the 2D flow area mesh. The DSW calculations neglects the transient and convection parts of the SW equations. These effects tend to increase as the cell sizes increase. However, small cell sizes increase the number of cells needed in the mesh hence increasing the simulation time considerable. Considering the 34 km long reach modelled in this work and the desire to run simulations on the whole model at once (not breaking it up to smaller areas), a cell size of 5x5 meters were chosen. To cover the whole reach 204 561 cells were used in the mesh and 9-12 hours were needed to complete one simulation.

Break lines were used in the hydraulic model to align the cells in the flow direction. The polyline features of the river boundary supplied by Terratec were imported as break lines in HEC-RAS. As the HEC-RAS manual specifies that break lines should be applied areas where abrupt changes in flow occurs, break lines were drawn on each of the weirs, perpendicular to the flow direction. Manipulation of the mesh using break lines aligns the cells in the preferred direction. The break lines can also be used to create a finer mesh in areas of interest, choosing a smaller cell size for the cells facing a break line. This was not deemed necessary for the break lines on the weirs. However, as finding the measures impact on water-covered area a smaller grid size of 2x2 meters were chosen for the boundary cells, allowing for more detailed calculations at the river boundaries.

The results in Table 8 **Error! Reference source not found.** show that the water-covered area is reduced by close to 10 % in the flow scenario of $1.5 \text{ m}^3/\text{s}$, indicating that the required environmental flow is an important measure in combating drying of areas due to hydropeaking. The reduction in water-covered area decreases as the flow increase in the hydraulic model and the highest flow scenario of $10 \text{ m}^3/\text{s}$ is least affected. This is an indication that for higher flow events ($> 10 \text{ m}^3/\text{s}$) the water covered area will not be significantly reduced due these weir measures.

Looking at Figure 20 and Figure 21 a reduction in the lower ranges of velocities can be seen. The reduced water-covered area must be considered when evaluating this. Many of the areas with low velocity becomes dry in the situation with measures on the weirs. The goal of the measures on weirs in Nea included in the model is to concentrate the flow over the weir and ease fish-migration. The result maps in appendix E provides a visual representation of the velocities in each weir-pool. These maps also show the changed flow over the weir. The flow is concentrated through the lowered section and the velocity is increased. This is a desirable effect to this type of measures as it will create a path for fish-migration over the weir.

5.3 Mapping River Ice

The approach for mapping river ice put forward in this thesis required field work at the study site with UAV and GNSS equipment in close proximity to the river but without the need to access the ice. The survey method in this work were completed by two persons, but a single person would be able to make the same measurements. All the surveys were completed in less than one hour, at the study site. All models were georeferenced with ten control points located close to the riverbanks, measured with differential GNSS. The georeferenced models were used to measure surface area and volume of the developing and break-up of river ice. This approach removes the need to access the ice providing a reliable and effective method for collecting data on river ice.

The data collection with remote sensing in Sokna included a survey in November with no ice present. The model developed from this data were used to inspect the river prior to ice formation, allowing to locate areas where ice processes would occur. The first survey in Sokna were conducted on 7 November 2018 with a complete ice-free river. Reconstructed models from this data is used as reference for a zero-ice river geometry when measuring ice in the other models. The orthomosaic is used to locate areas of interest in ice formation (e.g. large rocks where anchor ice can form). The first survey with ice present is the 25 January survey. The orthomosaic from this data show developed anchor ice located in an area where large rocks were observed, and ice cover starting to form on the banks and in the lower-end pool. The upstream area containing the largest boulders have the most anchor ice. The reconstructed models of the March survey show developed anchor ice dams blocking some areas. In addition, break-up of smaller sheets of the ice cover are seen being trapped in the narrow sections. The last survey of April 2019 shows retreating ice cover with indications of a recent ice run event.

6 CONCLUSION

Airborne LiDAR surveys can efficiently map large areas and the data it provides can be used to reconstruct detailed terrain models. Hydraulic modelling based on LiDAR data requires effective mapping of the under-water topography. The two LiDAR datasets used in this study reveal how survey conditions can influence the quality of collected data. The bathymetric coverage in the 2019 LiDAR data is 7.47 pts/m², an increase of point density on the riverbed by a factor of four compared to the 2018 survey data. Airborne LiDAR bathymetric surveys are affected by the conditions in the water, weather, aircraft altitude and post-processing routines by the supplier. Airborne LiDAR surveys will under ideal conditions supply accurate spatial data of the current terrain in a project area with greater efficiency than traditional ground-based measurements or satellite images.

The hydraulic model is calibrated against a measured water surface mapped by LiDAR on 27. July 2018 with a discharge of 1.5 m³/s from Heggsetdam to Bogstadhølen. This flow event is likely to occur in the period from May to September, as it corresponds to the required environmental flow in summer season. The calibrated model shows a difference in measured and simulated water surface elevation of ± 8 cm. This is considered acceptable as natural variations in the water surface and the vertical accuracy of the measurement is assumed to be on the decimeter level. Based on the calibration results it is considered likely that the hydraulic model generates reliable results in this flow scenario.

Hydraulic modelling is a useful tool when planning environmental design measures and assessing their influence on hydraulic conditions related to habitat and spawning areas or fish-migration. Hydraulic modelling reveals that the environmental design concept of lowering small sections on a weir will concentrate the flow over the weir and increase water velocity in the area around- and over the weir. The measures included in the hydraulic model will reduce the water-covered area by up to 10 % in the flow scenario representing the environmental flow between Heggsetdam and Bogstadhølen.

UAV topographic surveys and SfM software can be used to create detailed models of river ice. The surveys can be carried out in relative short time without accessing the river ice. The project area can be surveyed several times during the winter, collecting data on a developing ice cover, anchor ice or ice jam events. The low cost of equipment and detailed data it provides make it a viable tool for mapping river ice and analysis of dynamic ice processes.

Recommendations for future work:

- Measure the water surface during periods of high flow ($> 20 \text{ m}^3/\text{s}$) to provide calibration data to the hydraulic model for higher flow events.
- Model the hydraulic effect of changing the elevation in the lowered sections on the weirs and find the optimal height for concentrated flow and water-covered area
- Model the hydraulic effect of measures on a different set of weirs, including some of the larger weirs close to Bogstadhølen.
- Measuring hydraulic conditions in the river before and after weir modification will provide data to confirm the model's results.

REFERENCES

- Agisoft LCC (2016). *Agisoft Photoscan User Manual, Version 1.2*. Available at: https://www.agisoft.com/pdf/photoscan-pro_1_2_en.pdf (visited on: 12 May 2019)
- Alfredsen, K., Haas, C., Tuhtan, J., & Zinke, P. (2018). Brief Communication: Mapping river ice using drones and structure from motion. *The Cryosphere*, 12(2), 627-633.
- Arnekleiv, J.V., Koksvik, J., Rønning, L. & Kjærstad, G. (2006). Tiltaksrettet fiskebiologisk undersøkelse i Selbusjøen og Nea 2001-2005. - NTNU Vitenskapsmuseet Rapp. Zool. Ser. 2006, 2: 1- 83.
- ASPRS (2019). LAS SPECIFICATION, VERSION 1.4 - R14. The American Society for Photogrammetry & Remote Sensing. Available at: http://www.asprs.org/wp-content/uploads/2019/03/LAS_1_4_r14.pdf (visited on: 28 May 2019).
- ASPRS (2014). ASPRS Accuracy Standards for Digital Geospatial Data. Available at: https://www.asprs.org/wp-content/uploads/2015/01/ASPRS_Positional_Accuracy_Standards_Edition1_Version100_November2014.pdf (visited on: 29 May 2019)
- Bakken, T.H, Forseth, T. & Harby, A. (red.). (2016). Miljøvirkninger av effektkjøring: Kunnskapstatus og råd til forvaltning og industri. NINA Temahefte 62. 205 s.
- Bjølstad, O.K.H., Angell-Pettersen, S., Skatvold, B.R & Bergan, P.I. (2014). Forslag til plan for biotoptiltak i Nea på strekningen Bogstadhølen til Gresslidammen. Ungfiskundersøkelse, bonitering og forslag til tiltak. SWECO Rapport, Oppdragsnummer 584861. SWECO Norge AS Energi, Trondheim
- Bjølstad, O.K.H. (2015). Detaljplan for landskap og miljø. Nea – tiltak for terskler og biotoptiltak i Tydal kommune. SWECO Rapport, nr. 01-2015. Oppdragsnummer 584862. SWECO Norge AS Energi, Trondheim.
- Chu, T. and Lindenschmidt, K.-E. (2016). Integration of space-borne and air-borne data in monitoring river ice processes in the Slave River, Canada, *Remote Sens. Environ.*, 181, 65–81, <https://doi.org/10.1016/j.rse.2016.03.041>, 2016.
- Forseth, T. & Harby, A. (red.) (2013). Håndbok for miljødesign i regulerte laksevassdrag. – NINA Temahefte 52: 1-90
- Heidemann, Hans Karl (2018). Lidar base specification (ver. 1.3, February 2018): U.S. Geological Survey Techniques and Methods, book 11, chap. B4, 101 p., <https://doi.org/10.3133/tm11b4>
- Kartverket (2014). TopoBaty 2014: Eit pilotprosjekt om datainnsamling med grøn laser i kystsona. Tech. rep. Available at: <https://www.kartverket.no/contentassets/0b2c2d1337cc4a299d6fdc38d39c30eb/rappor- ttopobaty2014.pdf> (visited on: 26 May 2019)

- NVE (2006). *Rapport nr. 3/2006. Evaluering av terskler som avbøtende tiltak i et utvalg vassdrag i Midt- og Vest-Norge*. (3/2006). Available at: http://publikasjoner.nve.no/rapport_miljoebasert_vannfoering/2006/miljoebasert2006_03.pdf (visited on: 7 June 2019)
- Optech (2015). Optech Titan specification sheet. Available at: <http://info.teledyneoptech.com/acton/attachment/19958/f-02b6/1/-/-/-/Titan-Specsheet-150515-WEB.pdf> (visited on: 29 May 2019).
- Rapidlasso (2019). LAsTools. Available at: <https://rapidlasso.com/lastools/> (visited on: 22 May 2019).
- Stickler, M., Alfredsen, K., Linnansaari, T., & Fjeldstad, H. (2010). The influence of dynamic ice formation on hydraulic heterogeneity in steep streams. *River Research and Applications*, 26(9), 1187-1197.
- USACE (2016a). *HEC-RAS River Analysis System User's Manual Version 5.0*. (CPD-68): US Army Corps of Engineers Institute for Water Resources Hydrologic Engineering Center (HEC).
- USACE (2016b). *HEC-RAS River Analysis System, 2D Modeling User's Manual Version 5.0*. (CPD-68A): US Army Corps of Engineers Institute for Water Resources Hydrologic Engineering Center (HEC).
- yr.no (2019). Værstatistikk for Sokna (Kotsøy). Available at: https://www.yr.no/sted/Norge/Tr%C3%B8ndelag/Midtre_Gauldal/Gaula/statistikk.html (visited on: 29 May 2019).

APPENDICES

Appendix A: Weir locations and modelled measures

Appendix B: LiDAR coverage on weirs

Appendix C: Check point locations

Appendix D: Manning's n regions

Appendix E: Simulation results (raster)

Appendix F: Simulation results (table)

Appendix G: Cross-section profiles

Appendix H: File structure in attachment folder

APPENDIX A – WEIR LOCATIONS AND MODELLED MEASURES

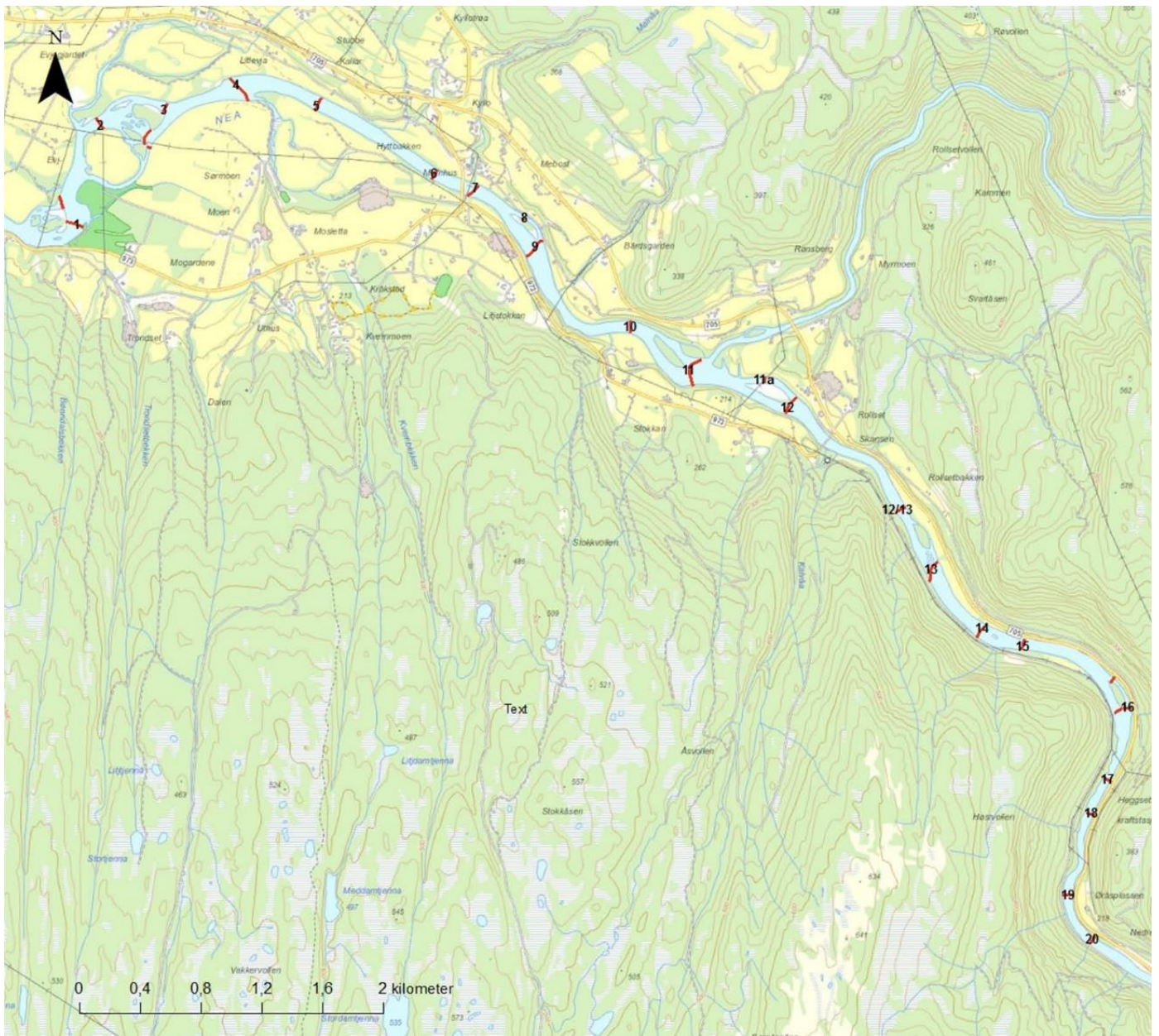


Figure 34: Map of Nea showing the locations of weir 1-20.

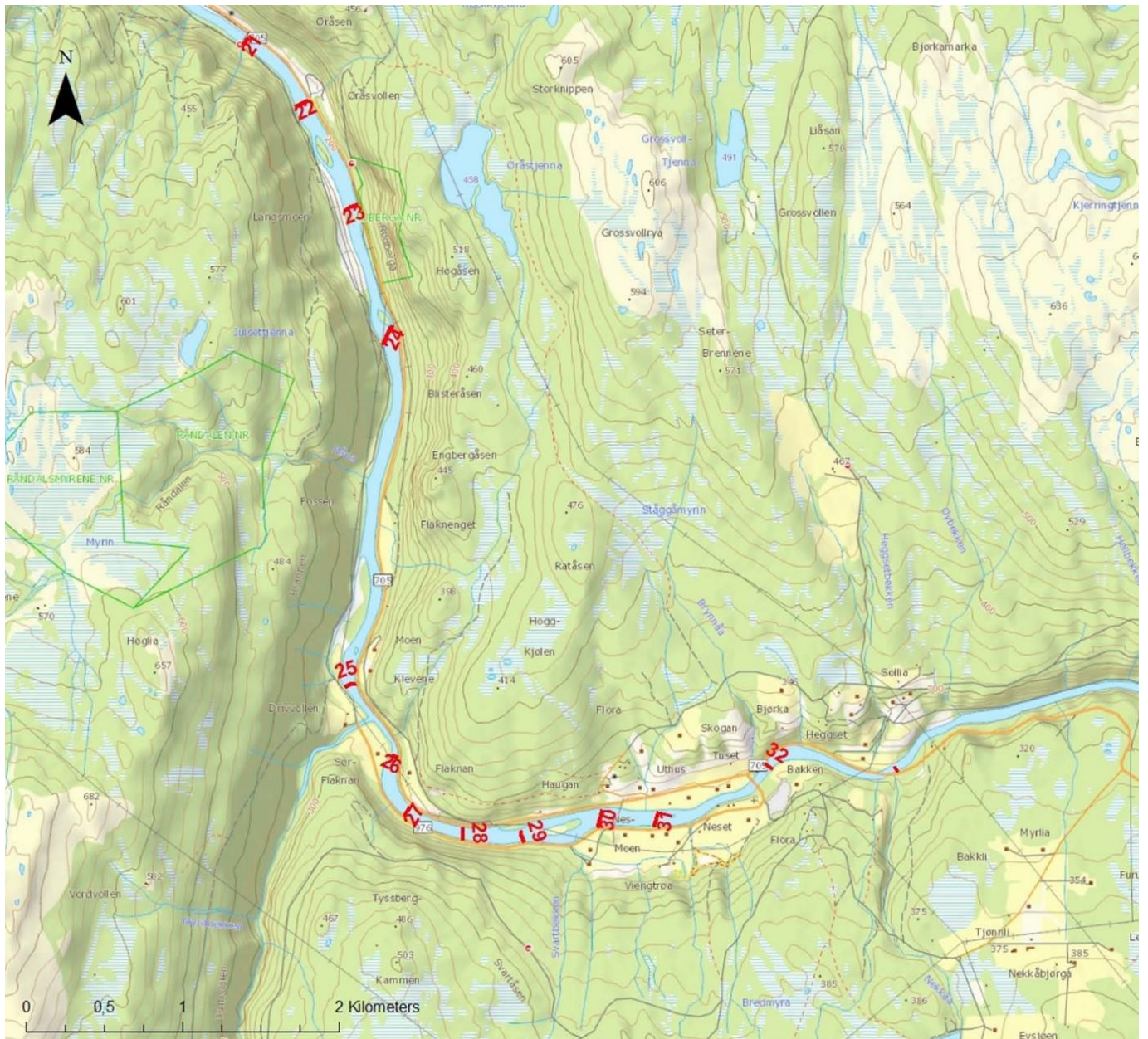


Figure 35: Map of Nea showing the locations of weir 21-32.

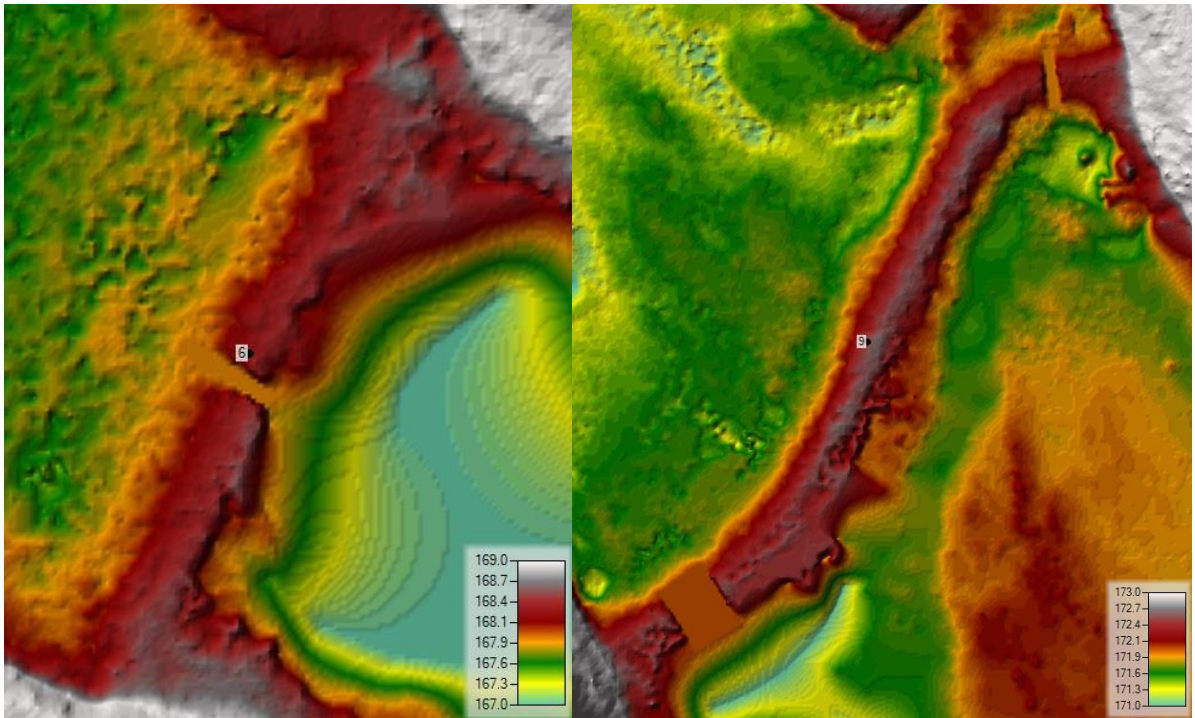


Figure 36: Terrain model with weir measures for weir 6 (left) and weir 9 (right).

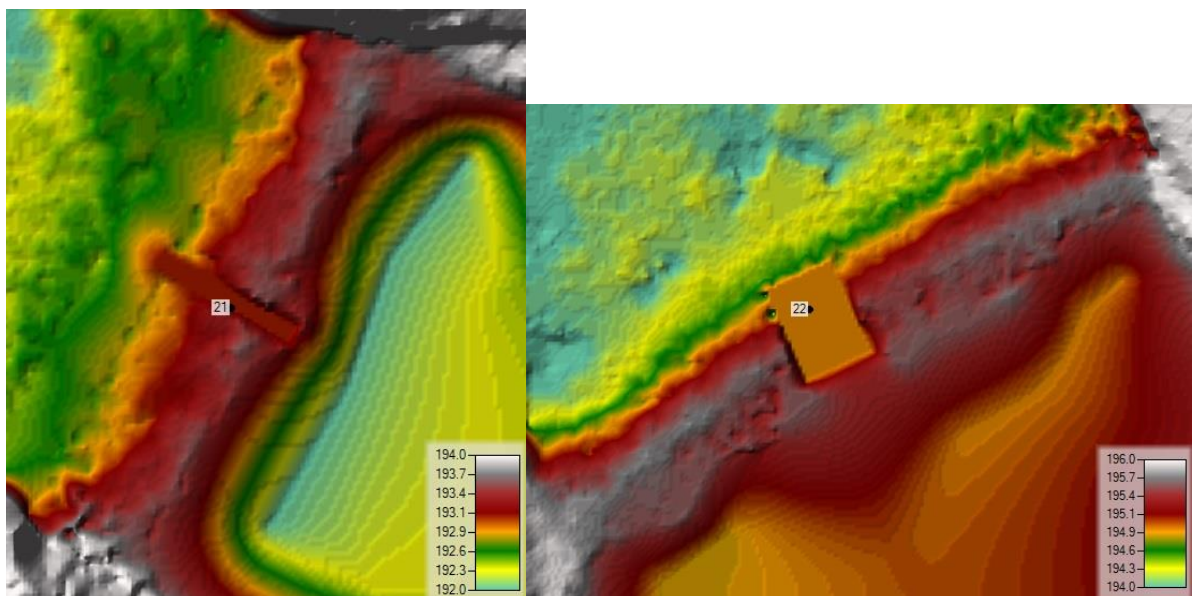


Figure 37: Terrain model with weir measures for weir 21 (left) and weir 22 (right).

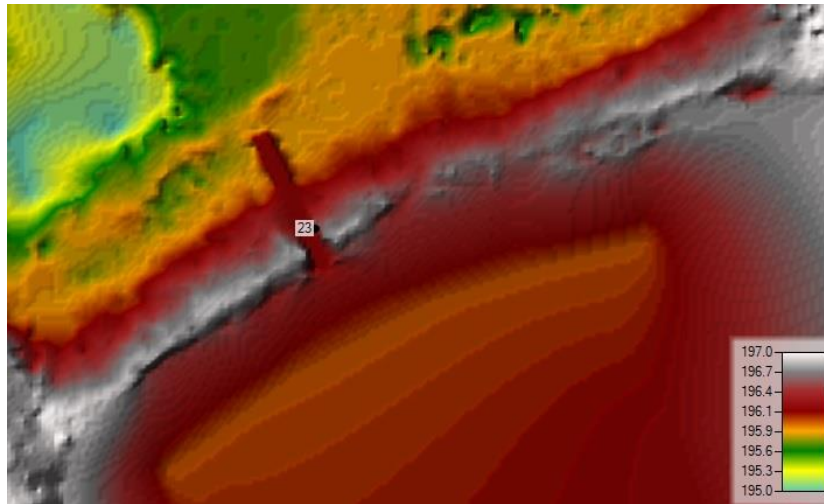


Figure 38: Terrain model with weir measures for weir 23.

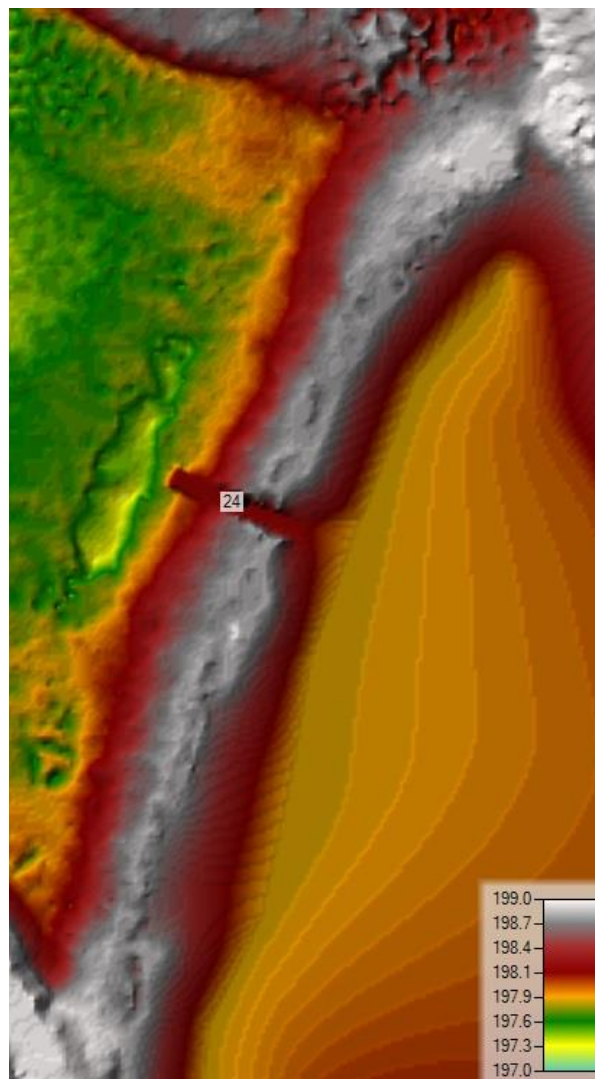


Figure 39: Terrain model with weir measures for weir 24.

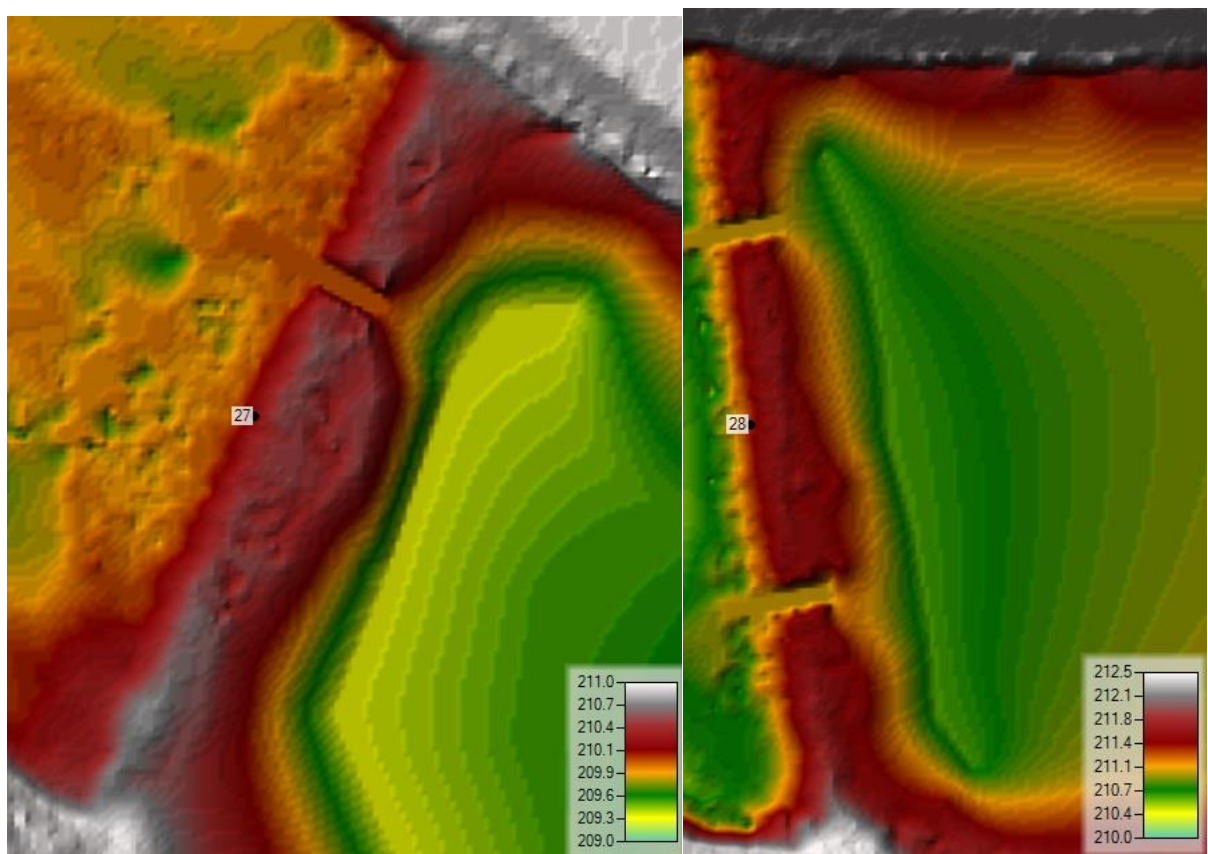


Figure 40: Terrain model with weir measures for weir 27 (left) and weir 38 (right).

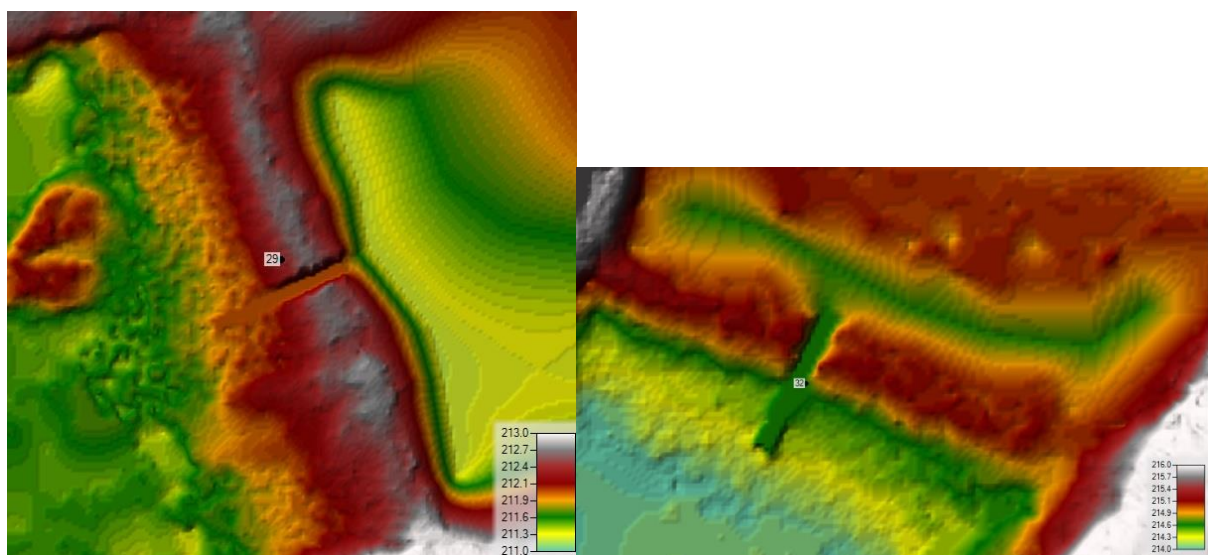


Figure 41: Terrain model with weir measures for weir 29 (left) and weir 32 (right).

APPENDIX B – LIDAR COVERAGE ON WEIRS

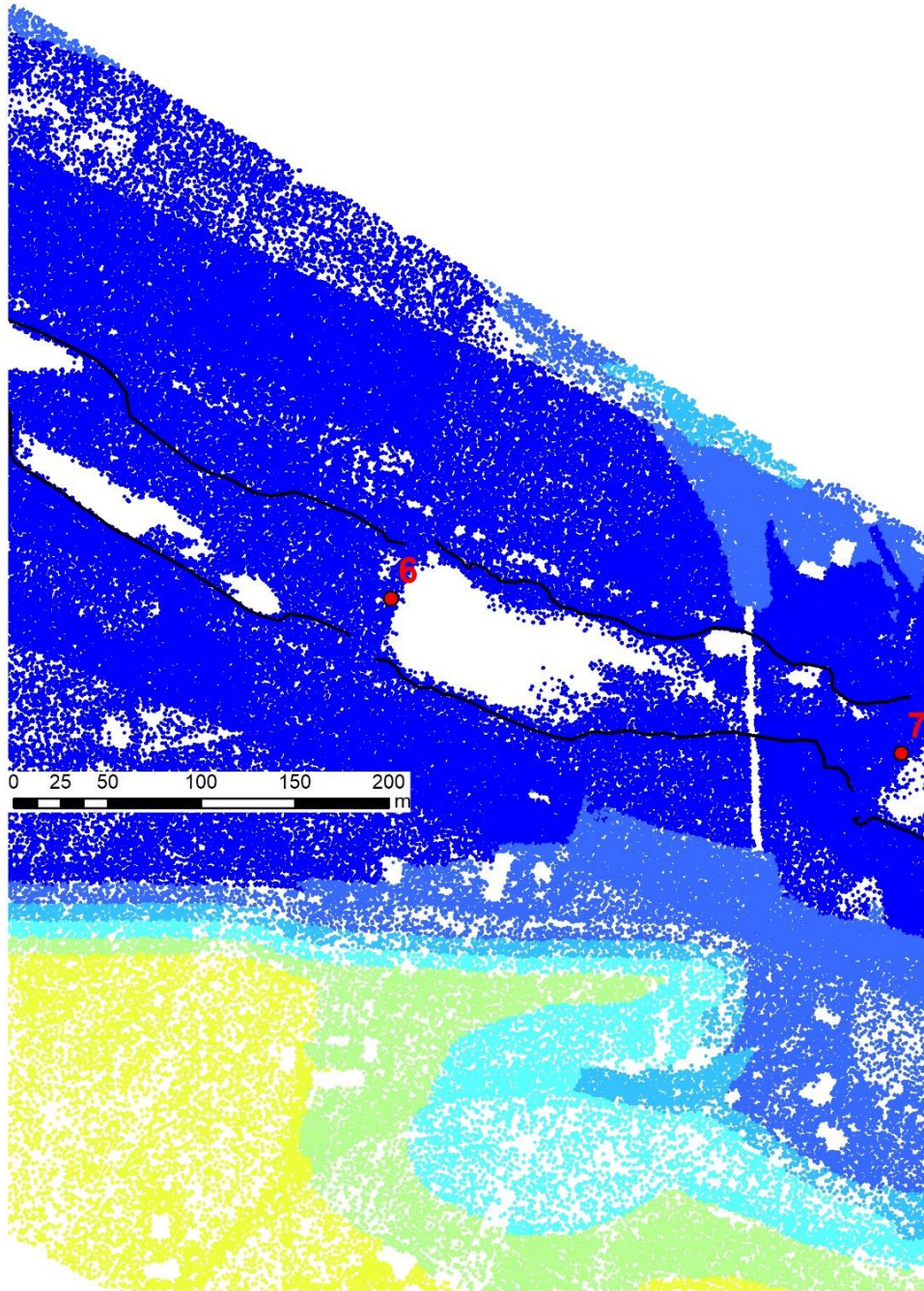


Figure 42: LiDAR point coverage on weir 6 from the combined 2018 and 2019 data.

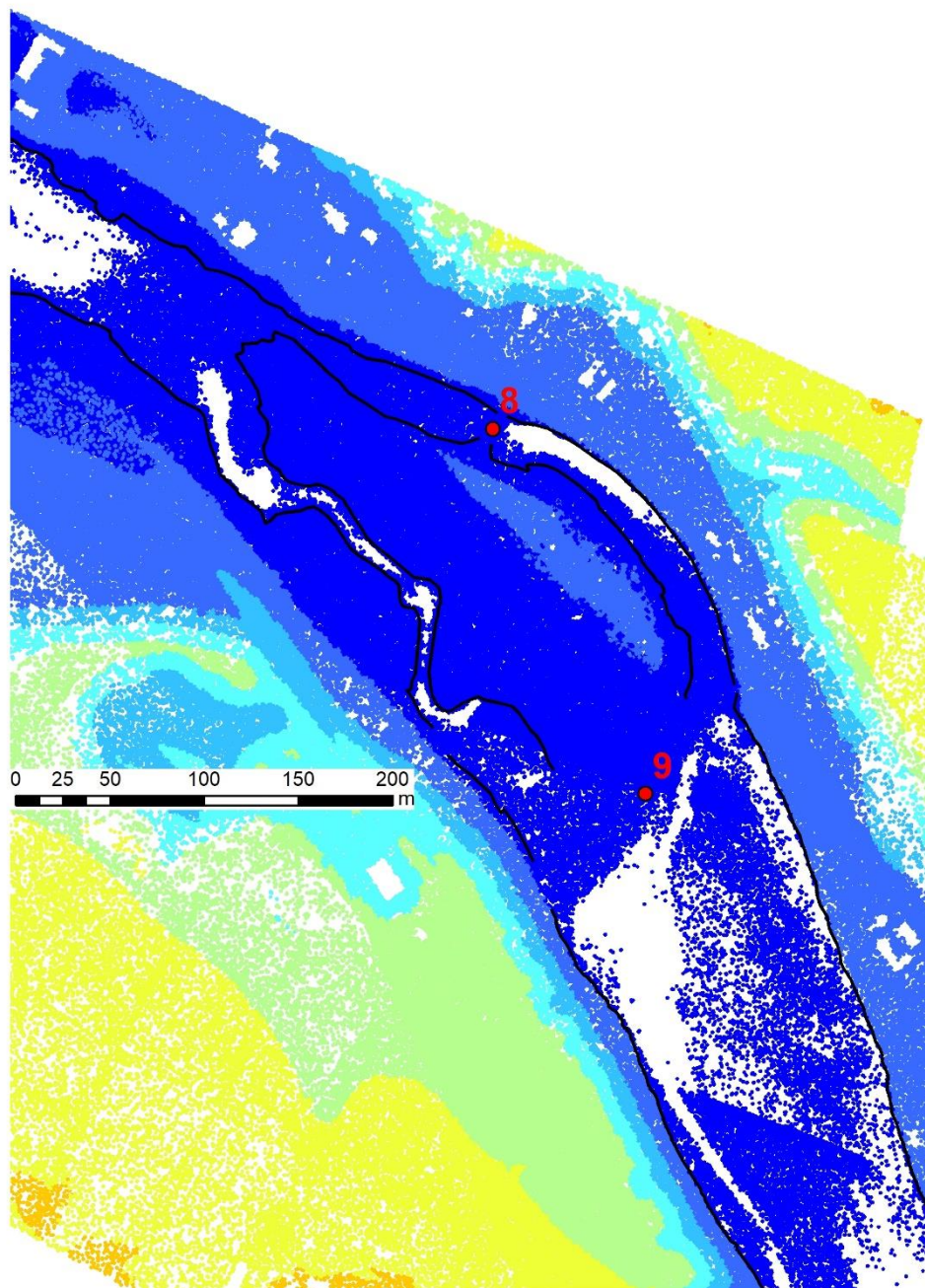


Figure 43: LiDAR point coverage on weir 9 from the combined 2018 and 2019 data.

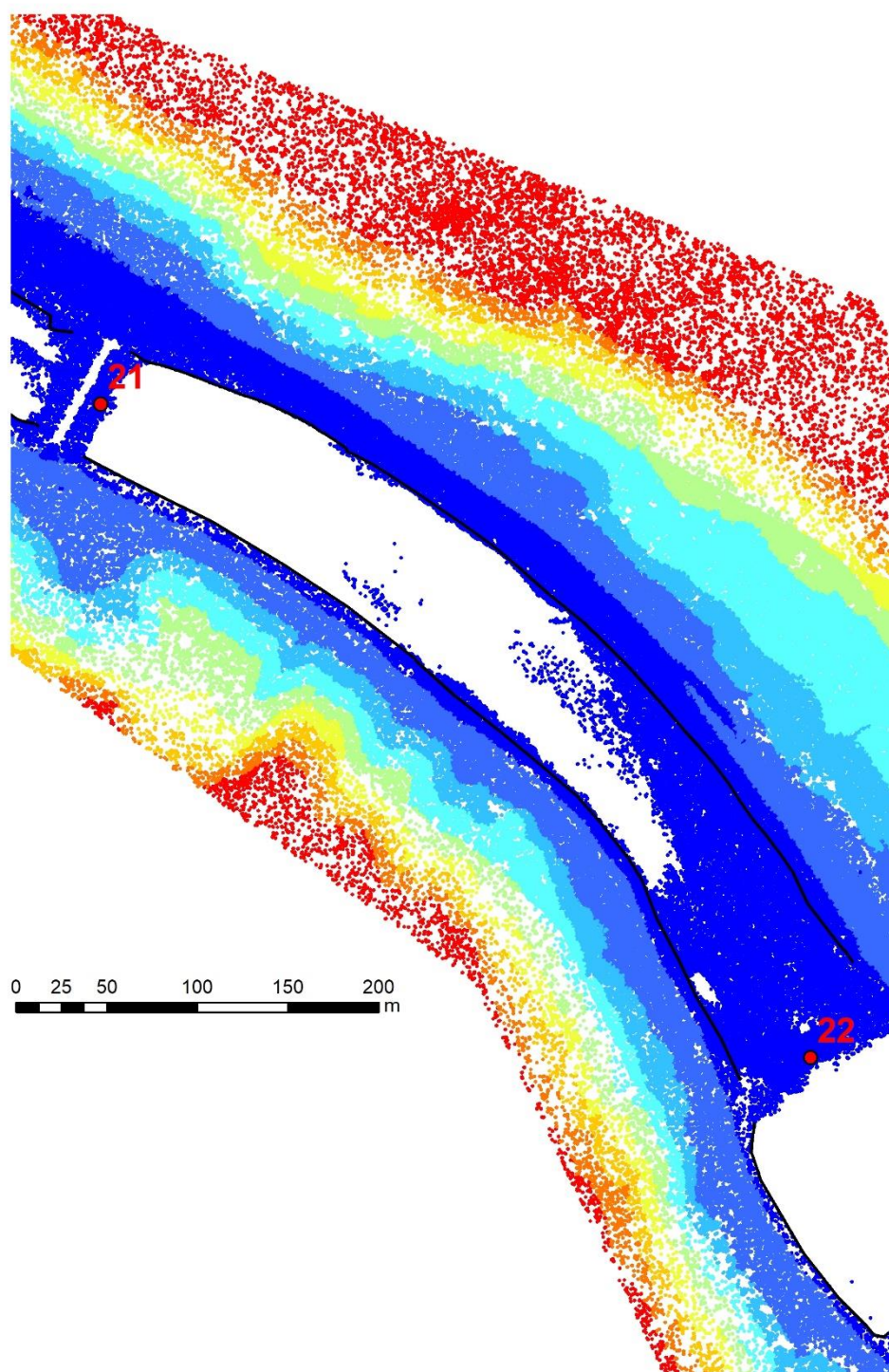


Figure 44: LiDAR point coverage on weir 22 from the combined 2018 and 2019 data.

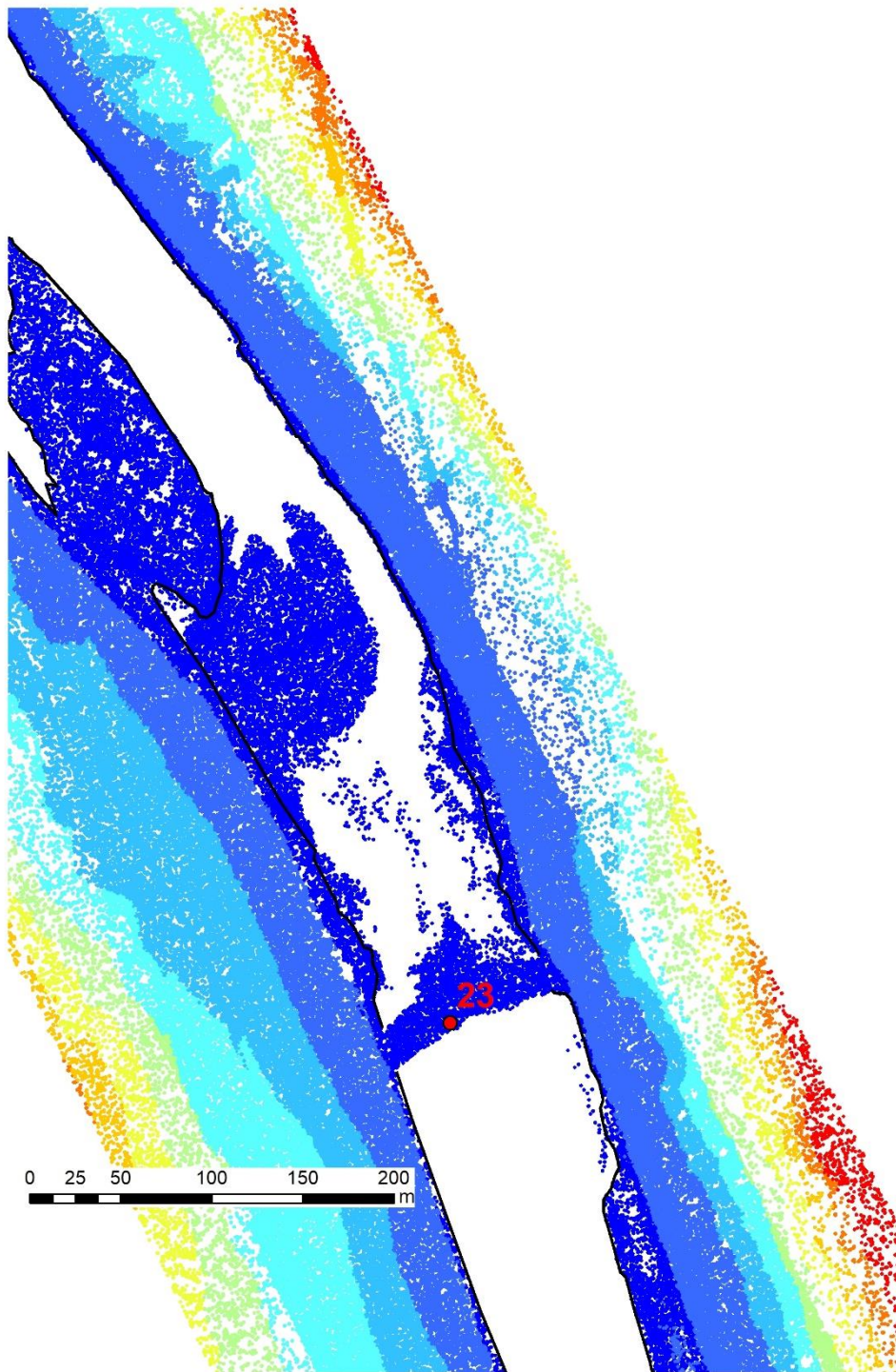


Figure 45: LiDAR point coverage on weir 23 from the combined 2018 and 2019 data.

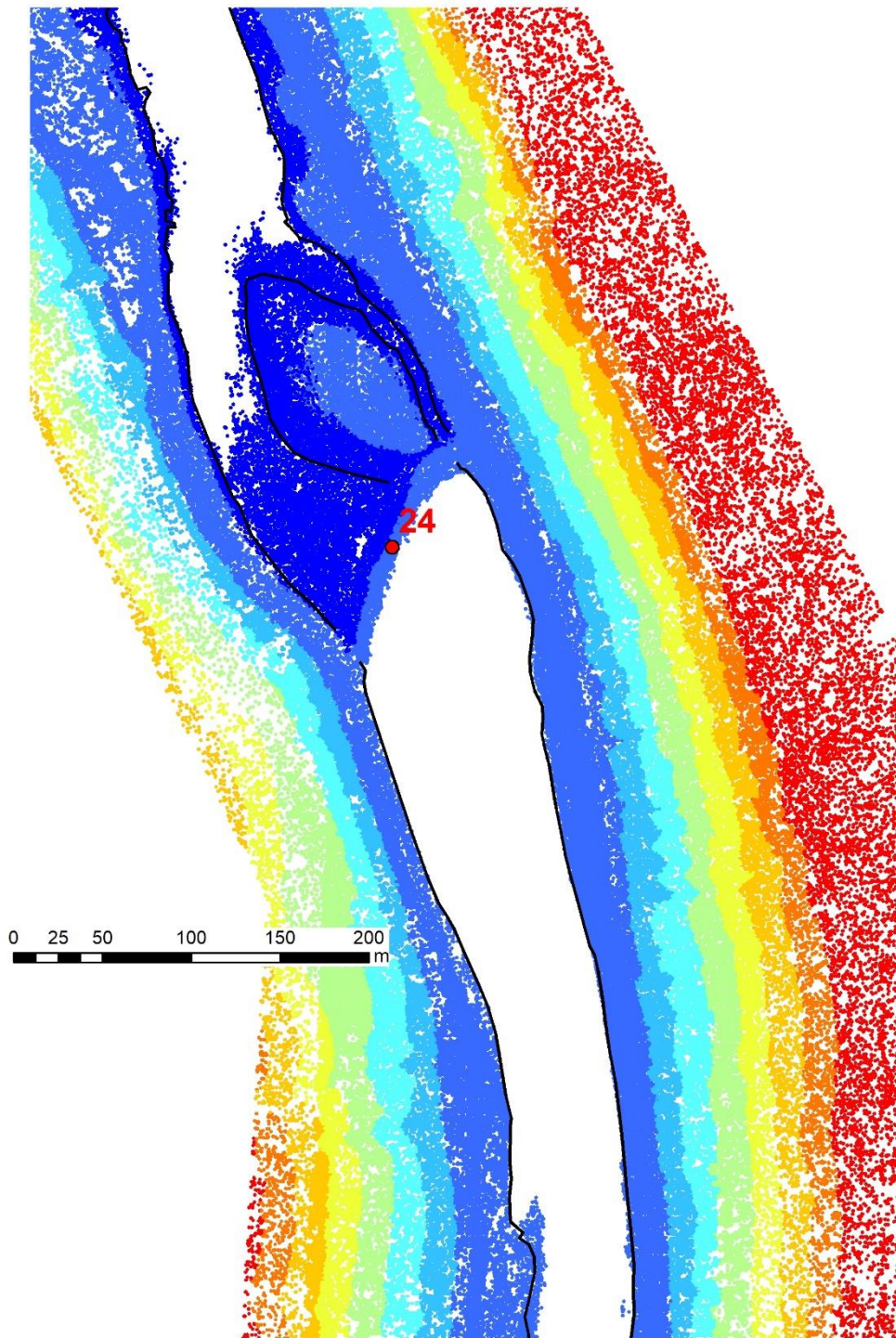


Figure 46: LiDAR point coverage on weir 24 from the combined 2018 and 2019 data.

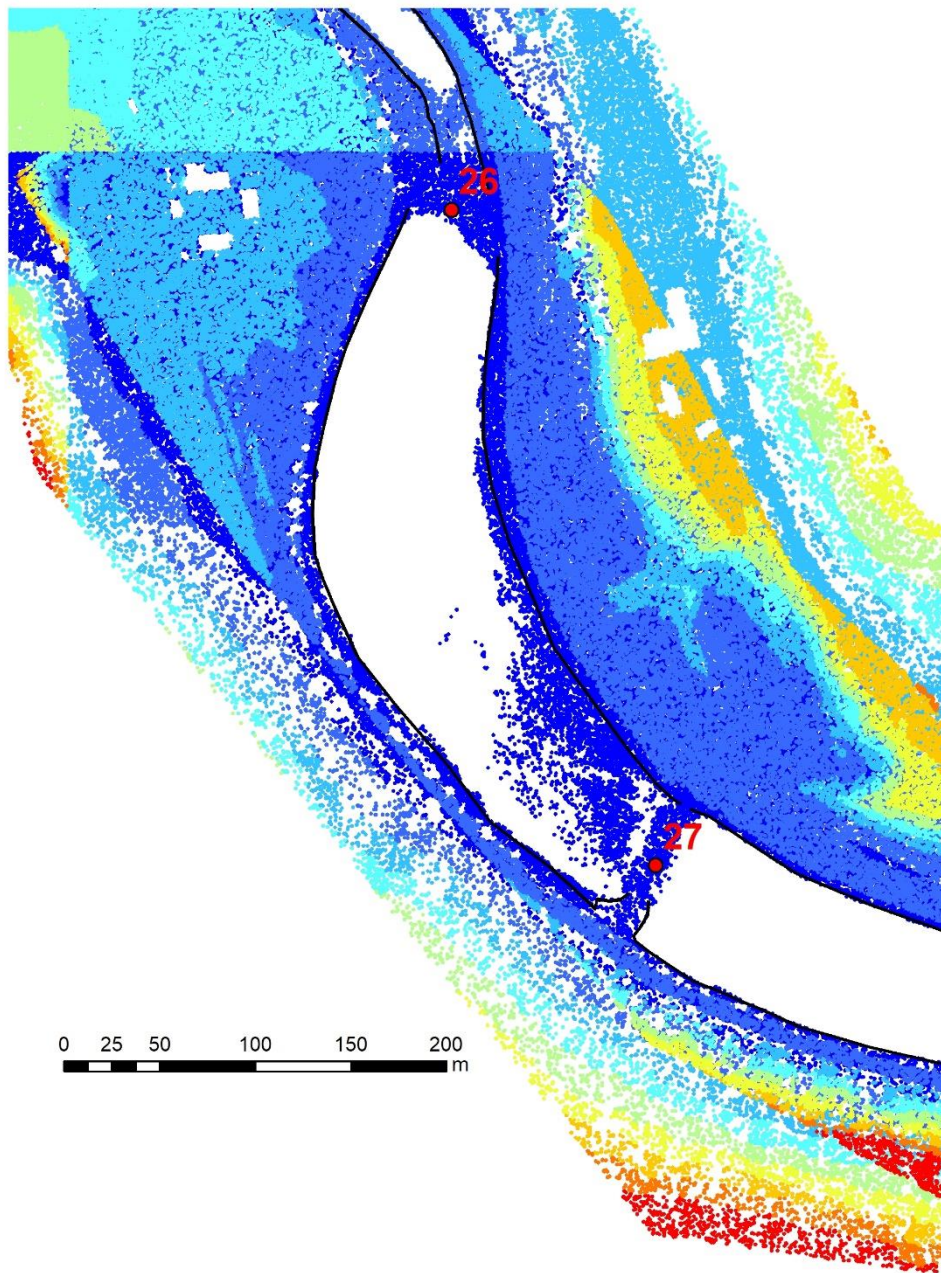


Figure 47: LiDAR point coverage on weir 27 from the combined 2018 and 2019 data.

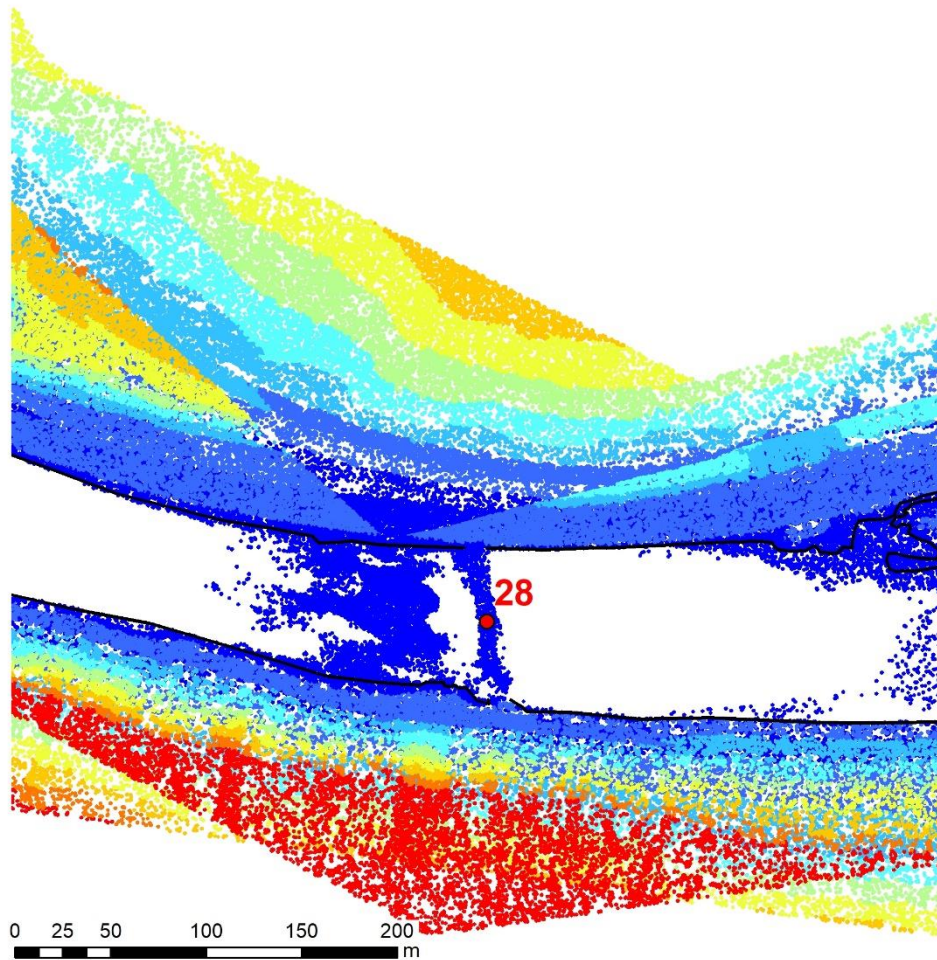


Figure 48: LiDAR point coverage on weir 28 from the combined 2018 and 2019 data.

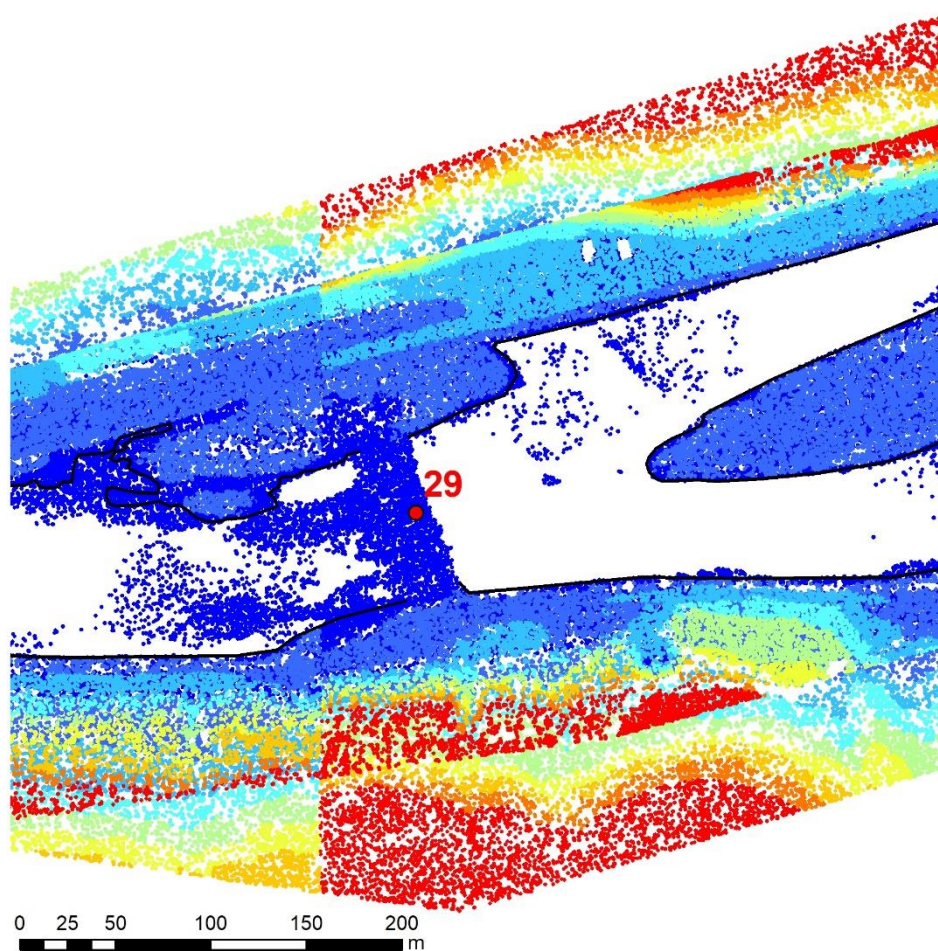


Figure 49: LiDAR point coverage on weir 29 from the combined 2018 and 2019 data.

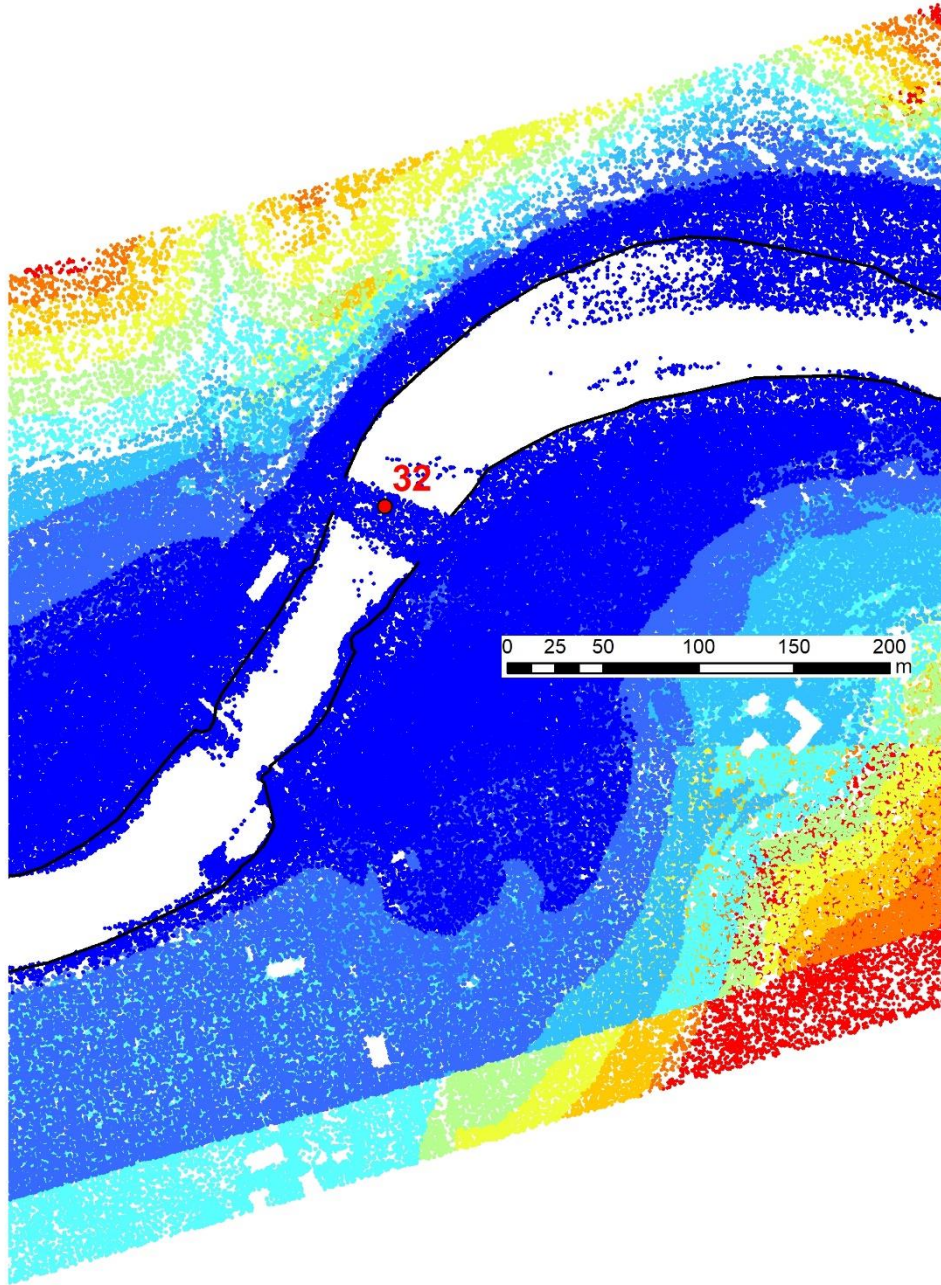


Figure 50: LiDAR point coverage on weir 32 from the combined 2018 and 2019 data.

APPENDIX C - CHECK POINT LOCATIONS

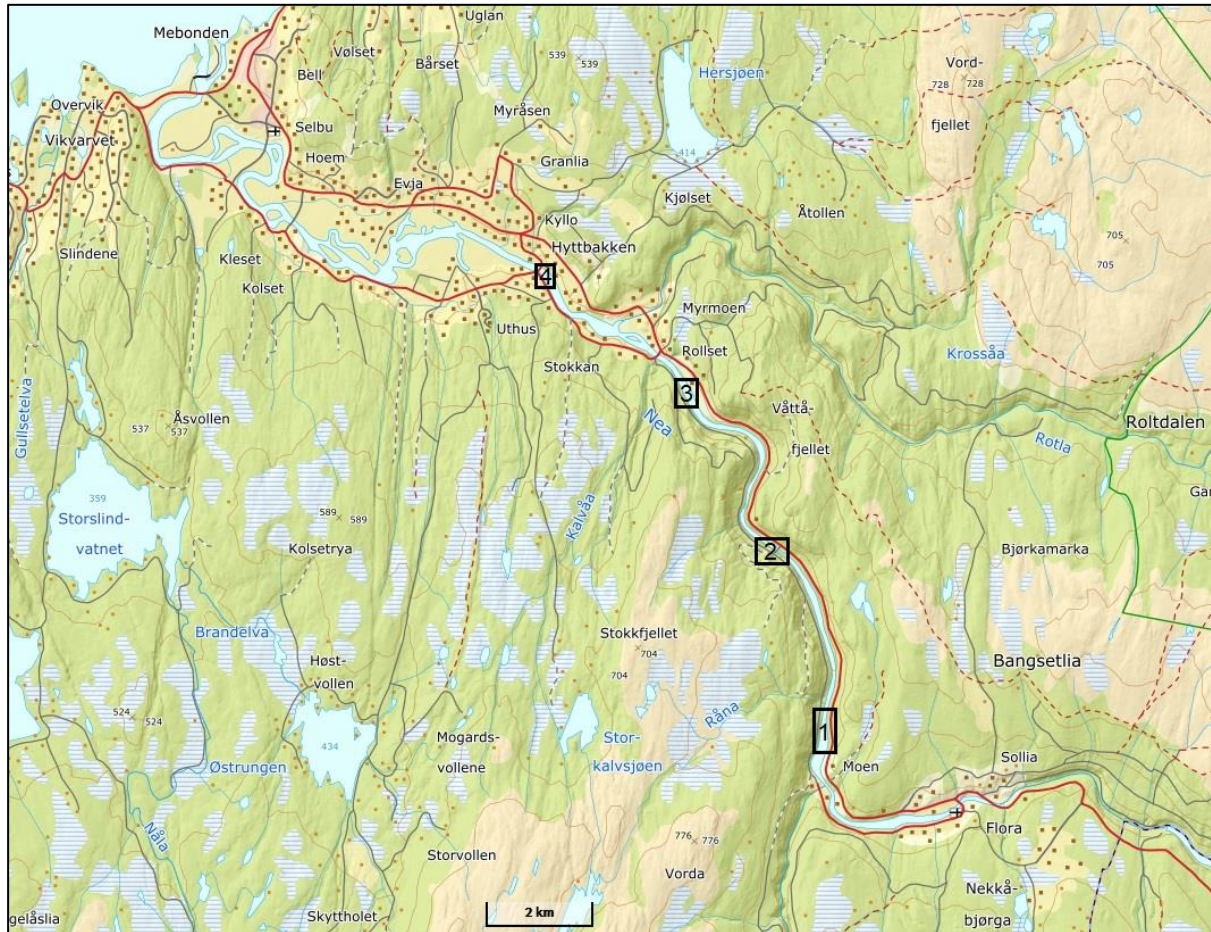


Figure 51: Map of the modeled reach in Nea (Hegsetdam to Selbusjø) and the four areas of each check point group location.

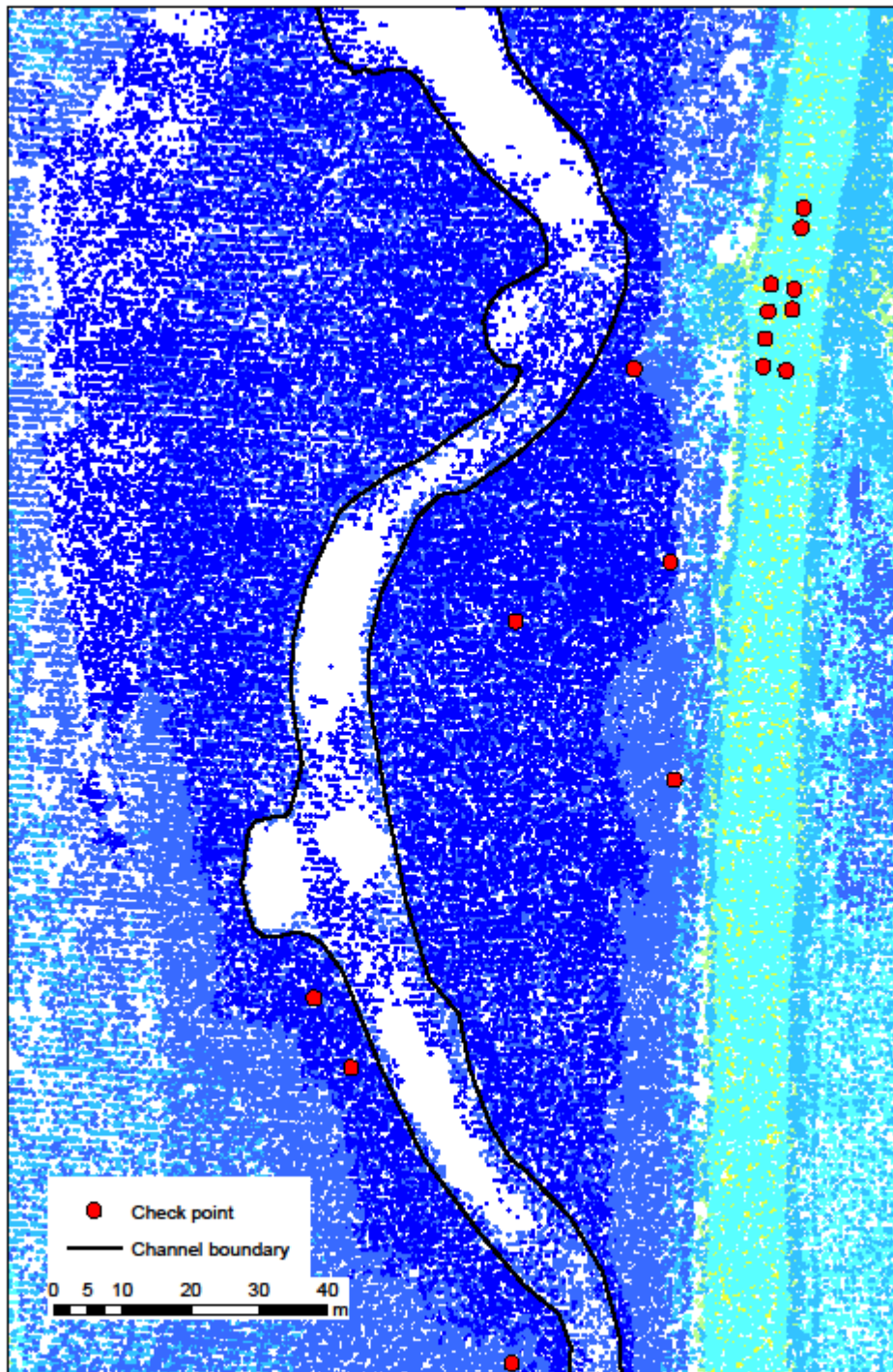


Figure 52: Check point locations in area 1 containing check points in group 7 (5 asphalt, 4 road barrier posts, 7 rocks above water).

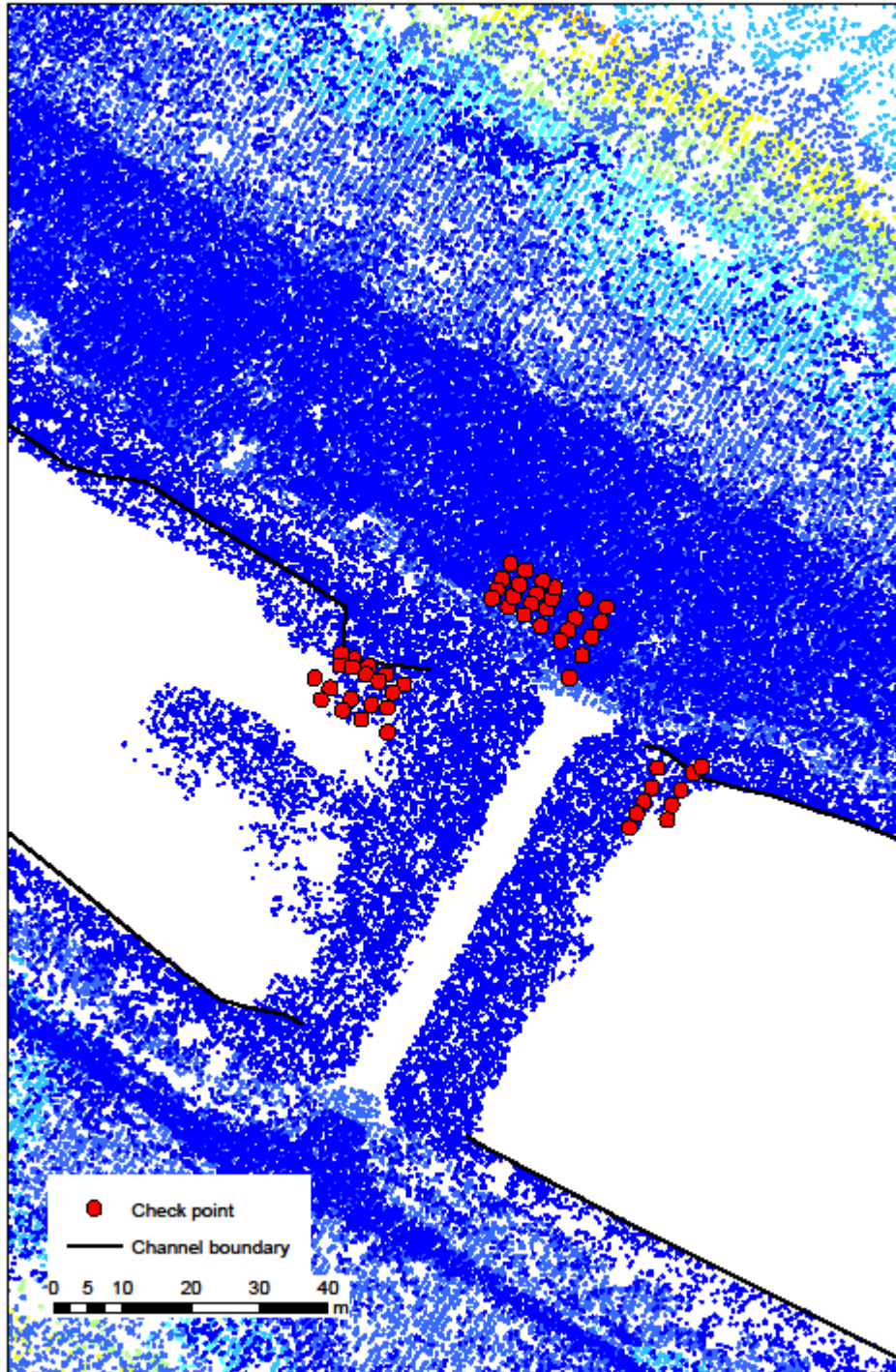


Figure 53: Check point locations in area 2 containing check points in group 1 (29 under water) and 6 (25 asphalt).

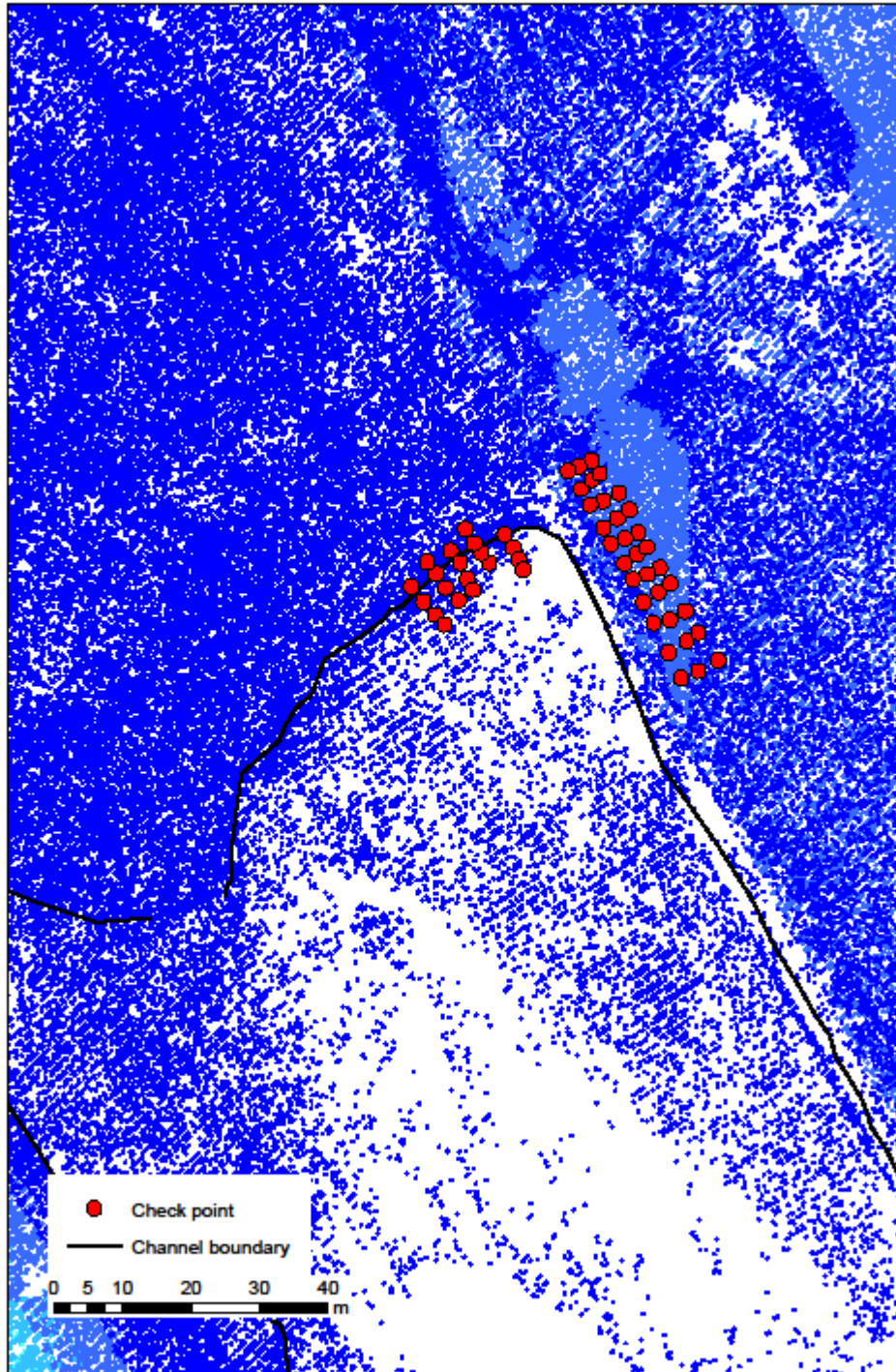


Figure 54: Check point locations in area 3 containing check points in group 2 (20 under water) and 5 (33 grass).

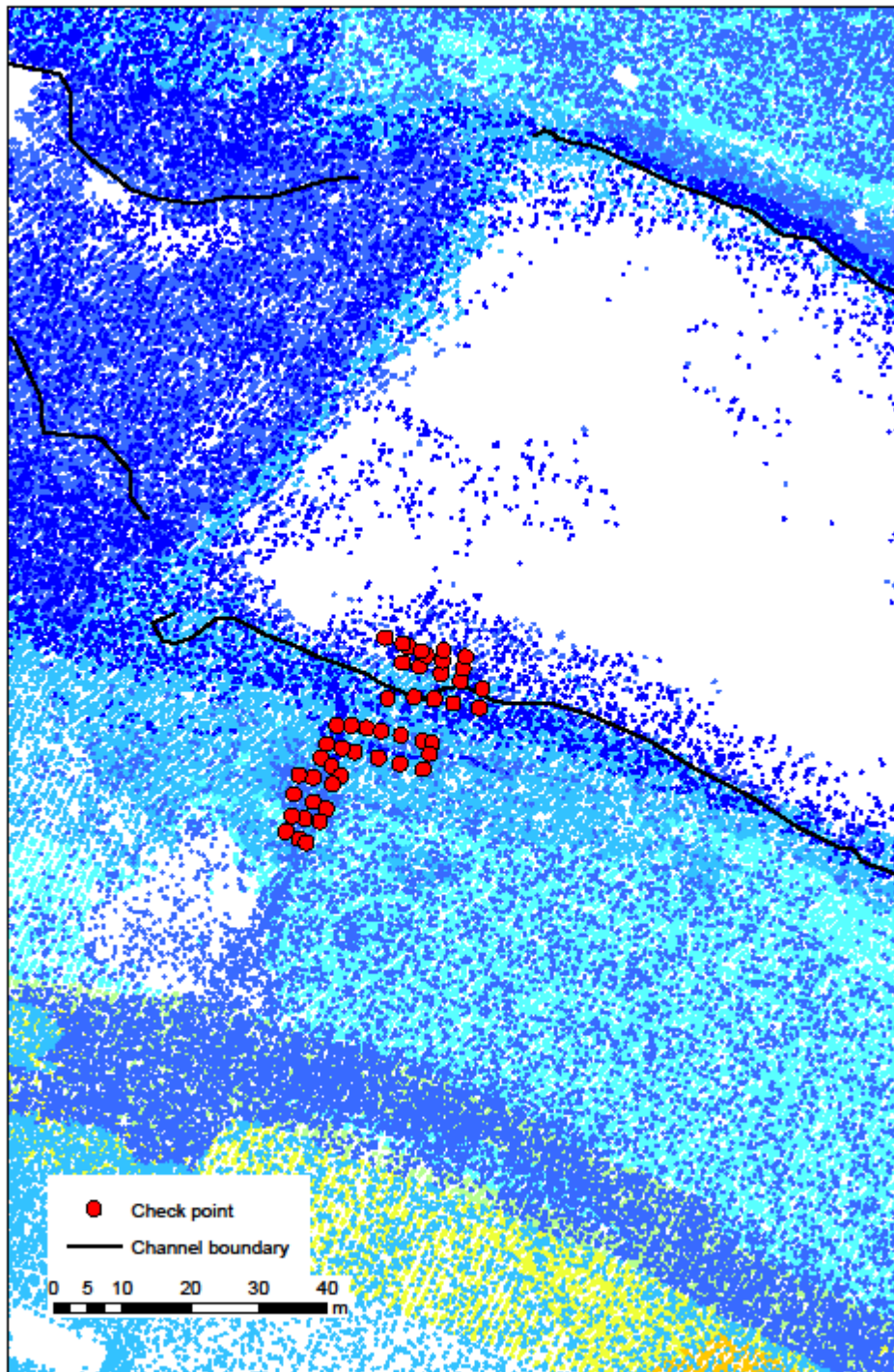


Figure 55: Check point locations in area 4 containing check points in group 3 (19 under water) and 4 (29 grass).

APPENDIX D - MANNING'S N REGIONS

Manning's Region	Area (m²)	n_Value	Manning's Region	Area (m²)	n_Value
0	11139	0.01	46	494970	0.01
1	12182	0.018	47	32085	0.01
2	12361	0.018	48	54282	0.01
3	12969	0.01	49	63086	0.01
4	14160	0.01	50	59026	0.08
5	20927	0.01	51	287188	0.06
6	23976	0.01	52	333706	0.06
7	48705	0.01	53	111495	0.01
8	9297	0.06	54	712369	0.045
9	7373	0.006	55	996	0.08
10	8741	0.018	56	621	0.01
11	5747	0.01	57	411	0.01
12	6319	0.018	58	970	0.01
13	2816	0.08	59	14116	0.006
14	3764	0.01	60	136453	0.01
15	521	0.08	61	866	0.08
16	602	0.08	62	1124	0.018
17	313	0.06	63	5292	0.018
18	3757	0.08	64	12498	0.018
19	5680	0.018	65	734	0.08
20	26699	0.06	66	817	0.08
21	1815	0.006	67	7205	0.006
22	361	0.06	68	769	0.01
23	25811	0.045	69	8833	0.018
24	9965	0.08	70	681	0.01
25	12349	0.01	71	54	0.018
26	347	0.06	72	1244	0.018
27	1447	0.06	73	4824	0.018
28	11395	0.01	74	1484	0.08
29	6914	0.01	75	264	0.08
30	2149	0.006	76	649	0.08
31	1798	0.006	77	149	0.06

32	669	0.006	78	403	0.06
33	1510	0.01	79	2080	0.018
34	19066	0.045	80	1253	0.08
35	9575	0.018	81	1123	0.08
36	40273	0.06	82	969	0.01
37	73440	0.06	83	1844	0.01
38	6554	0.06	84	23052	0.018
39	42645	0.06	85	11007	0.018
40	1030	0.06	86	58565	0.08
41	259488	0.01	87	115605	0.018
42	493448	0.01	88	2330	0.08
43	95855	0.01	89	7529	0.08
44	131331	0.01	90	2981	0.08
45	80227	0.01			

APPENDIX E - SIMULATION RESULTS (RASTER)

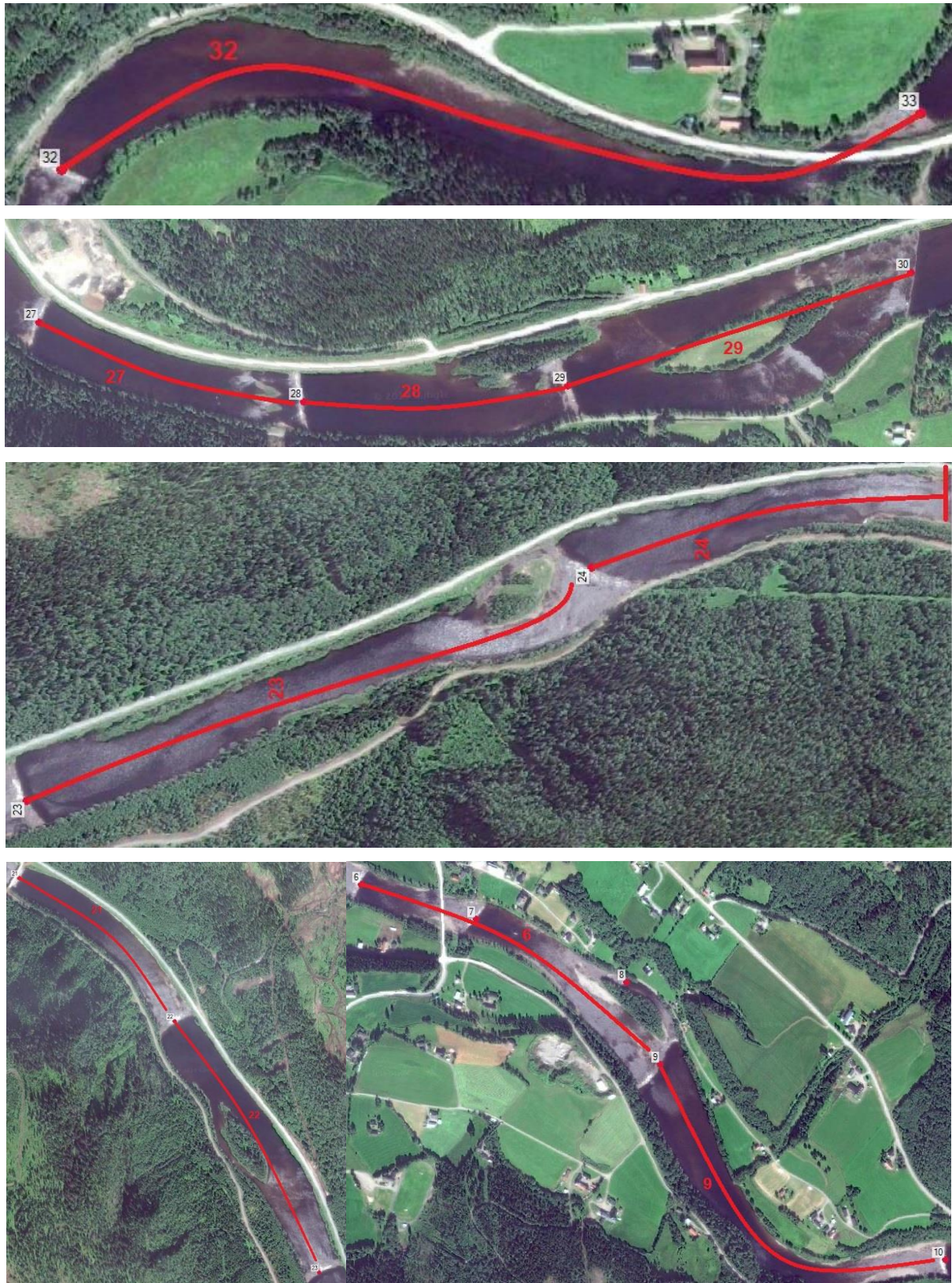


Figure 56: Map of all the weirs modelled with measures and the upstream weir-reservoir.

Q1.5



Figure 57: Simulation results as depth map for current (top) and after (bottom) for weir 32 at $1.5 \text{ m}^3/\text{s}$.

Q5

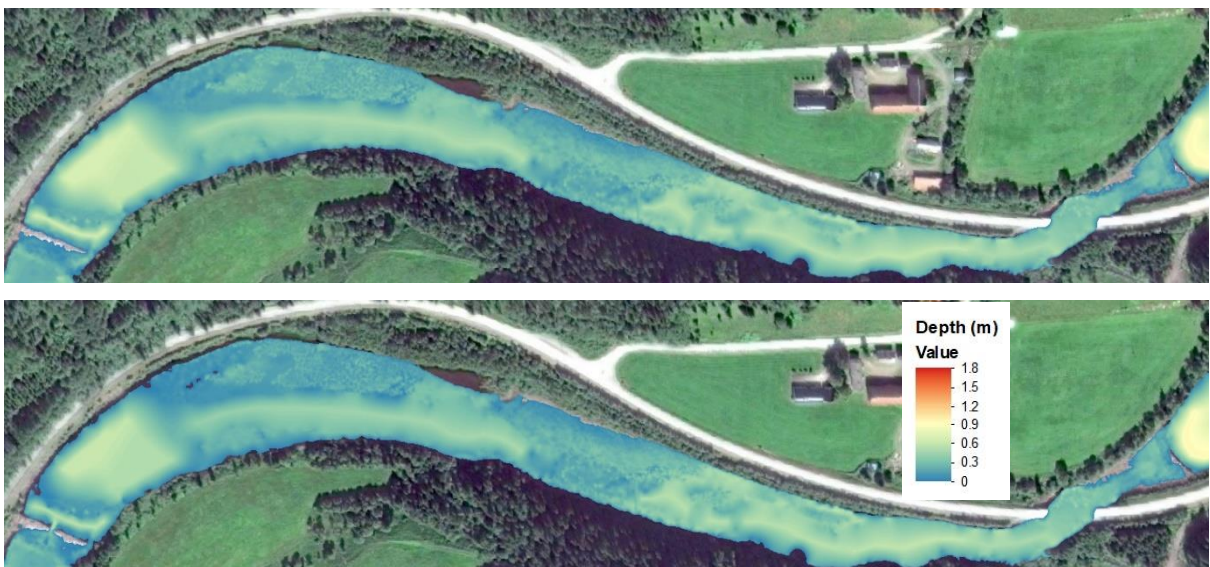


Figure 58: Simulation results as depth map for current (top) and after (bottom) for weir 32 at $5 \text{ m}^3/\text{s}$.

Q10

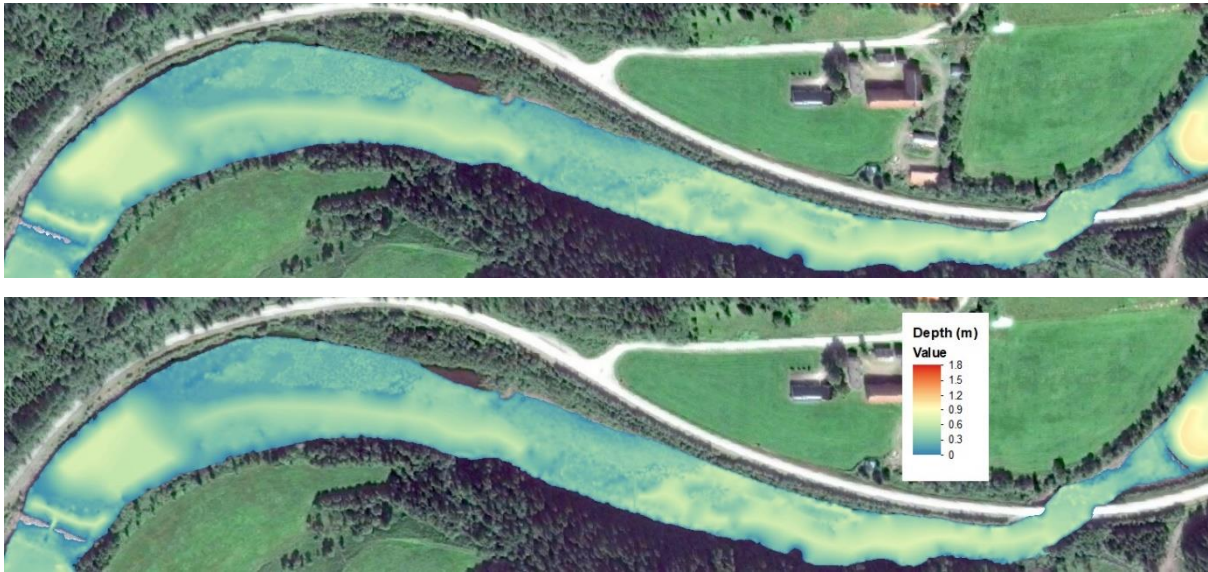


Figure 59: Simulation results as depth map for current (top) and after (bottom) for weir 32 at $10 \text{ m}^3/\text{s}$.

Q1.5

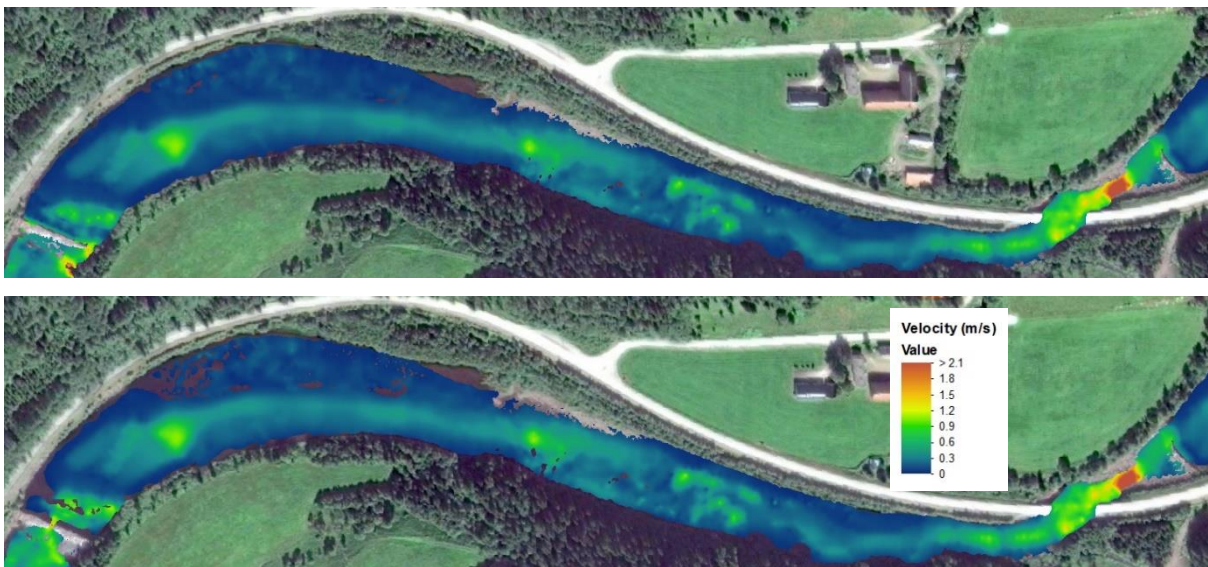


Figure 60: Simulation results as velocity map for current (top) and after (bottom) for weir 32 at $1.5 \text{ m}^3/\text{s}$.

Q5



Figure 61: Simulation results as velocity map for current (top) and after (bottom) for weir 32 at $5 \text{ m}^3/\text{s}$.

Q10

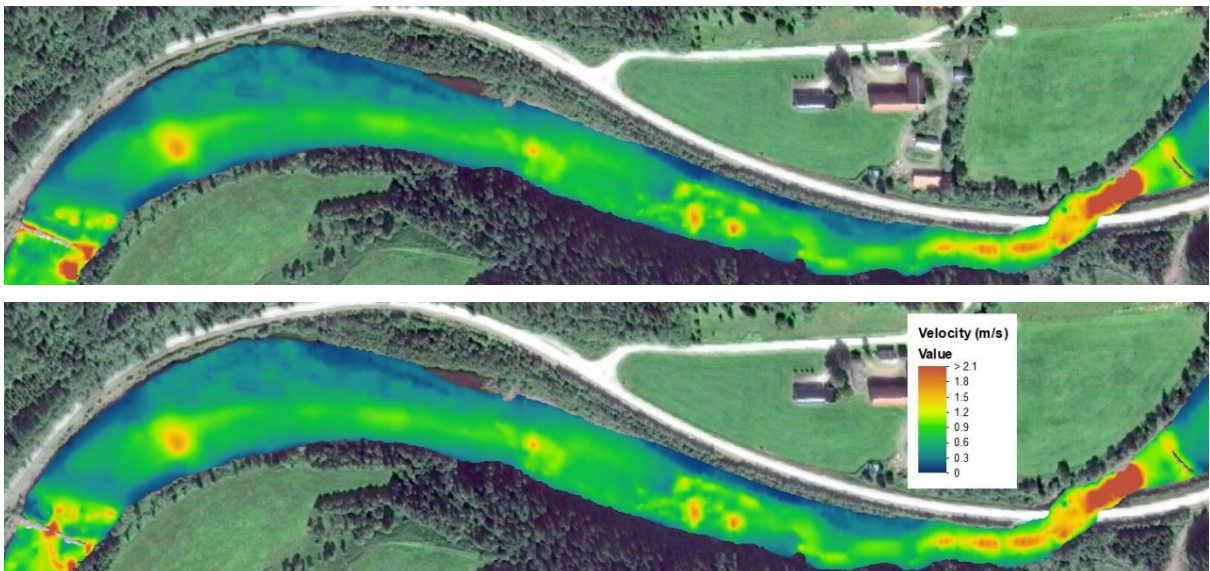


Figure 62: Simulation results as velocity map for current (top) and after (bottom) for weir 32 at $10 \text{ m}^3/\text{s}$.

Q1.5

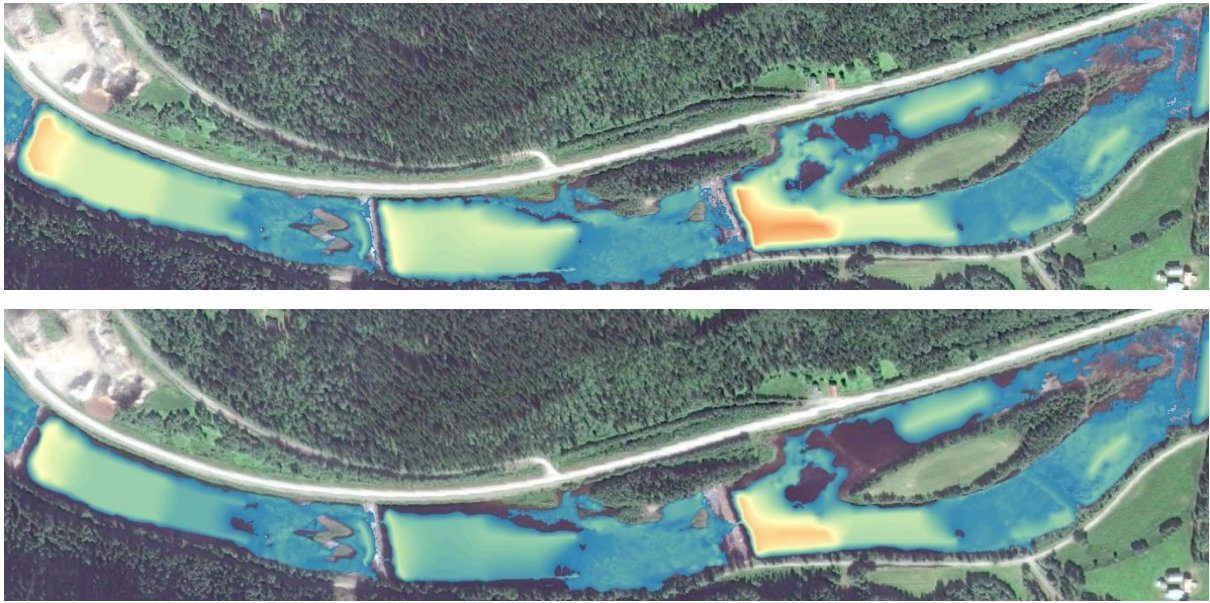


Figure 63: Simulation results as depth map for current (top) and after (bottom) for weir 27, 28 and 29 at $1.5 \text{ m}^3/\text{s}$.

Q5

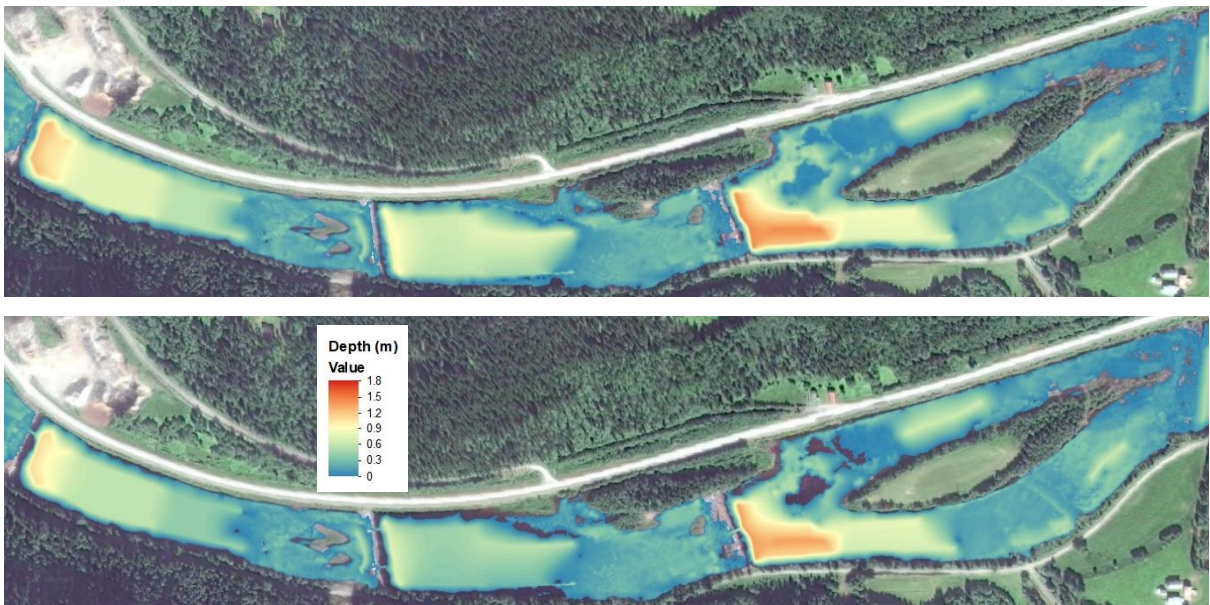


Figure 64: Simulation results as depth map for current (top) and after (bottom) for weir 27, 28 and 29 at $5 \text{ m}^3/\text{s}$.

Q10

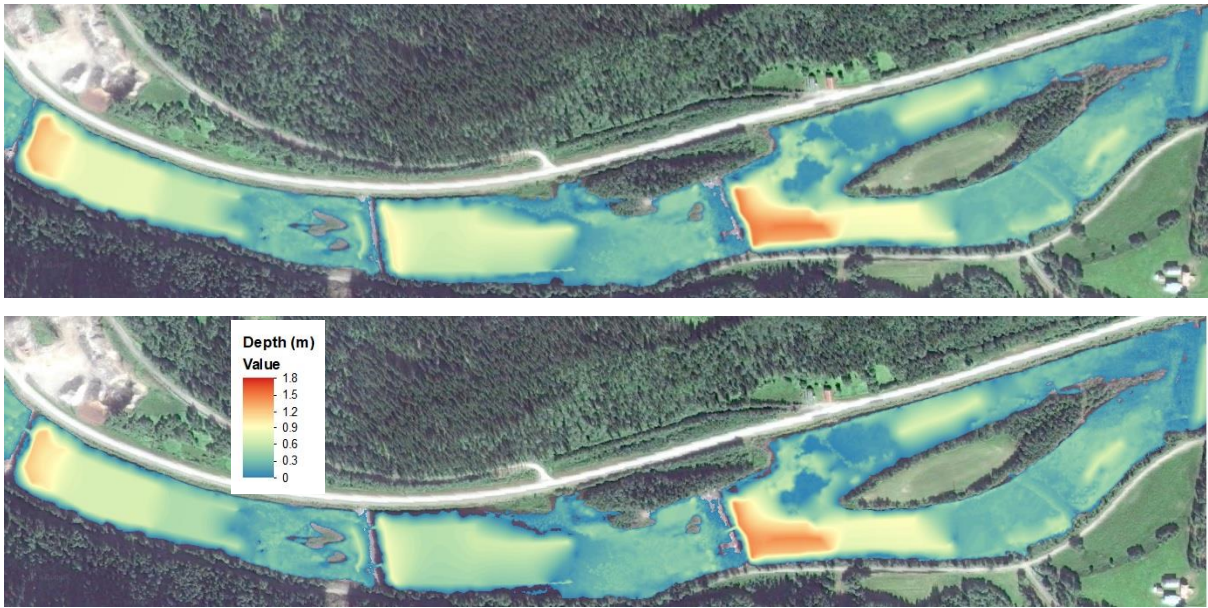


Figure 65: Simulation results as depth map for current (top) and after (bottom) for weir 27, 28 and 29 at $10 \text{ m}^3/\text{s}$.

Q1.5

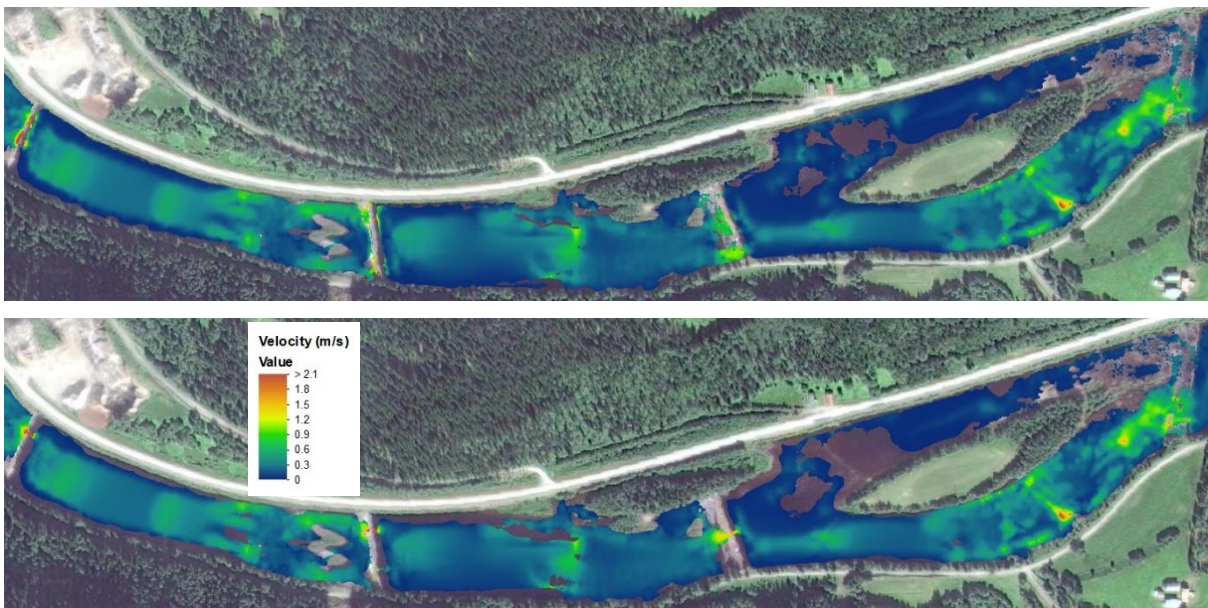


Figure 66: Simulation results as velocity map for current (top) and after (bottom) for weir 27, 28 and 29 at $1.5 \text{ m}^3/\text{s}$.

Q5

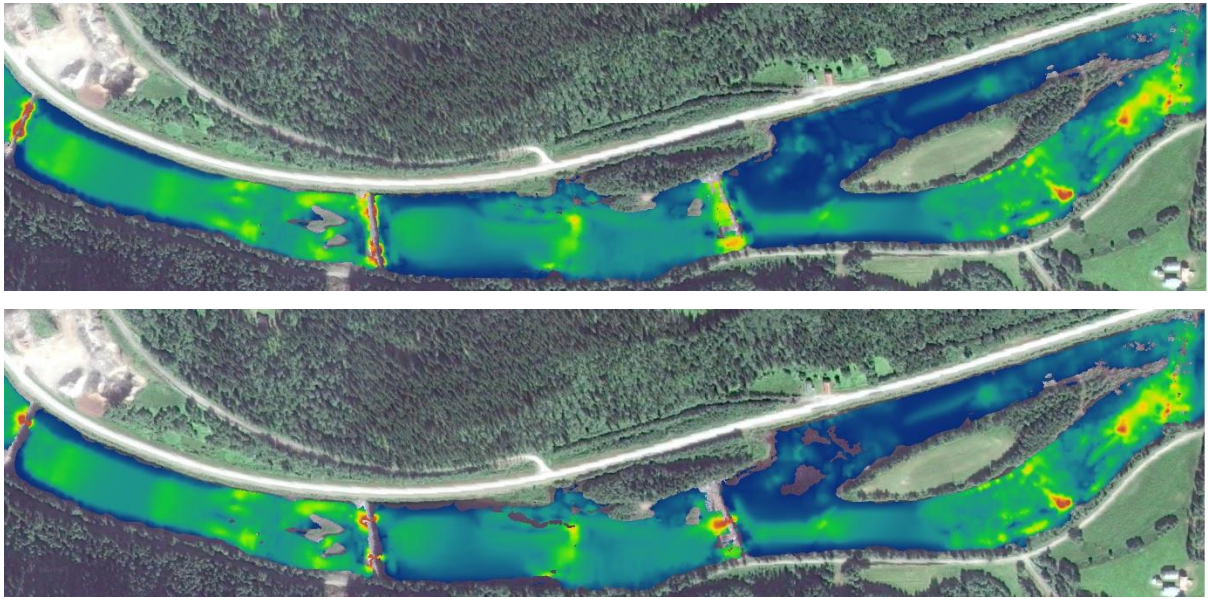


Figure 67: Simulation results as velocity map for current (top) and after (bottom) for weir 27, 28 and 29 at $5 \text{ m}^3/\text{s}$.

Q10

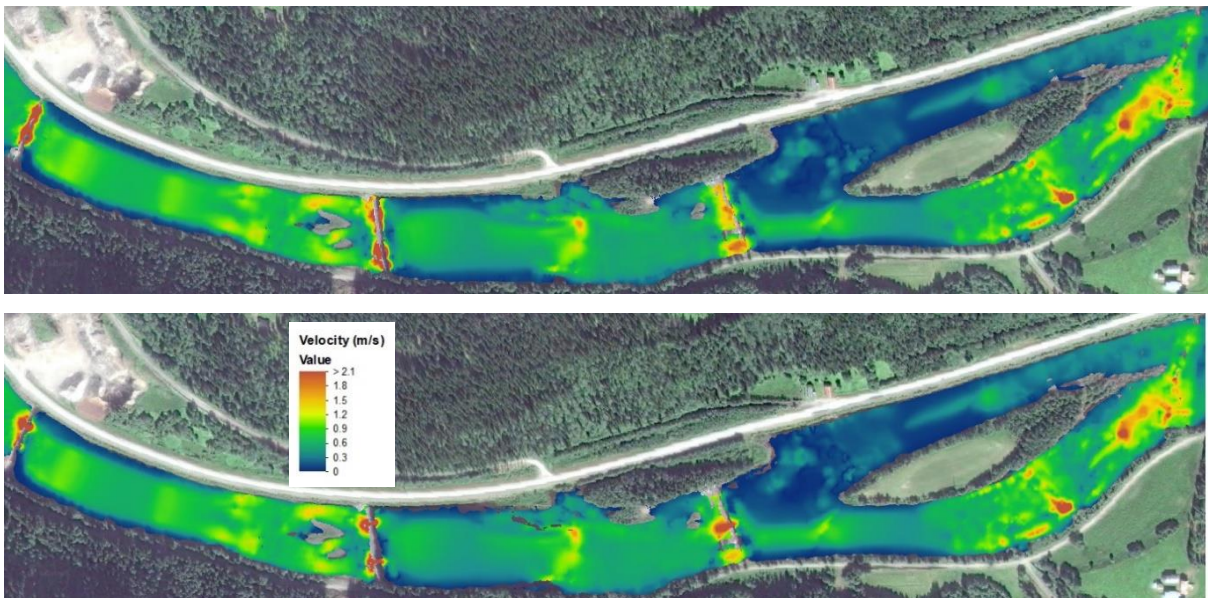


Figure 68: Simulation results as velocity map for current (top) and after (bottom) for weir 27, 28 and 29 at $10 \text{ m}^3/\text{s}$.

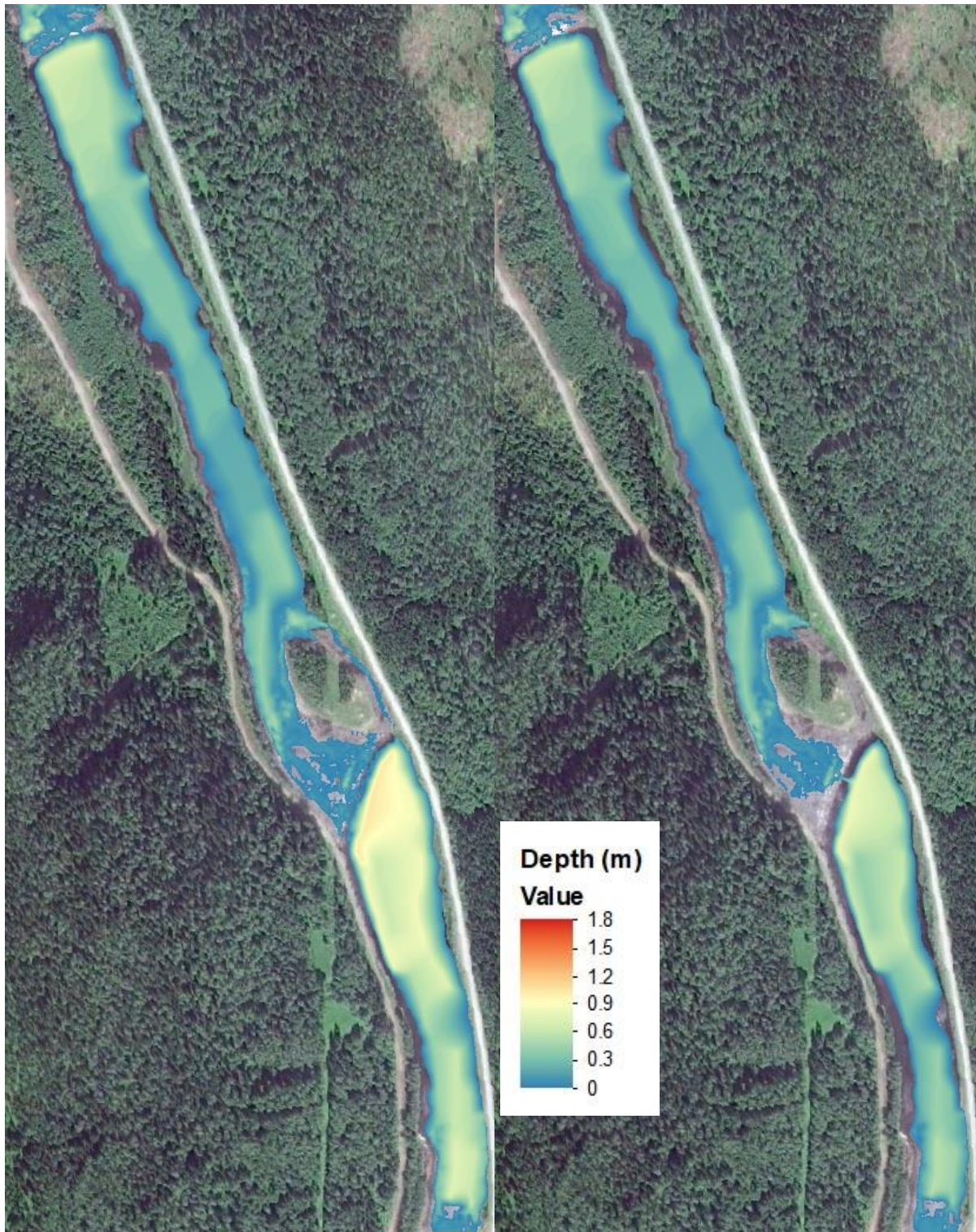


Figure 69: Simulation results as depth map for current (left) and after (right) for weir 23 and 24 at $1.5 \text{ m}^3/\text{s}$.

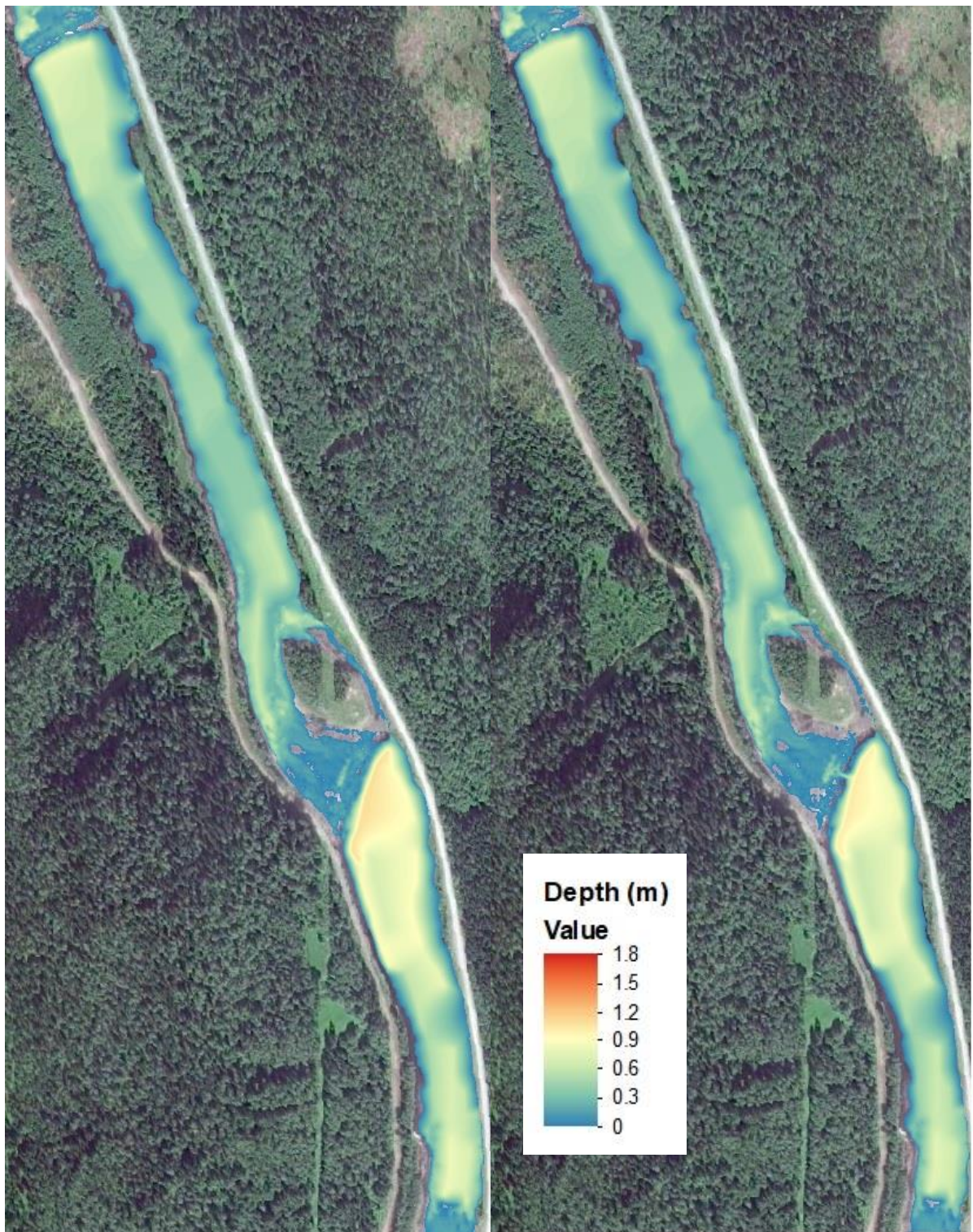


Figure 70: Simulation results as depth map for current (left) and after (right) for weir 23 and 24 at 5 m³/s.

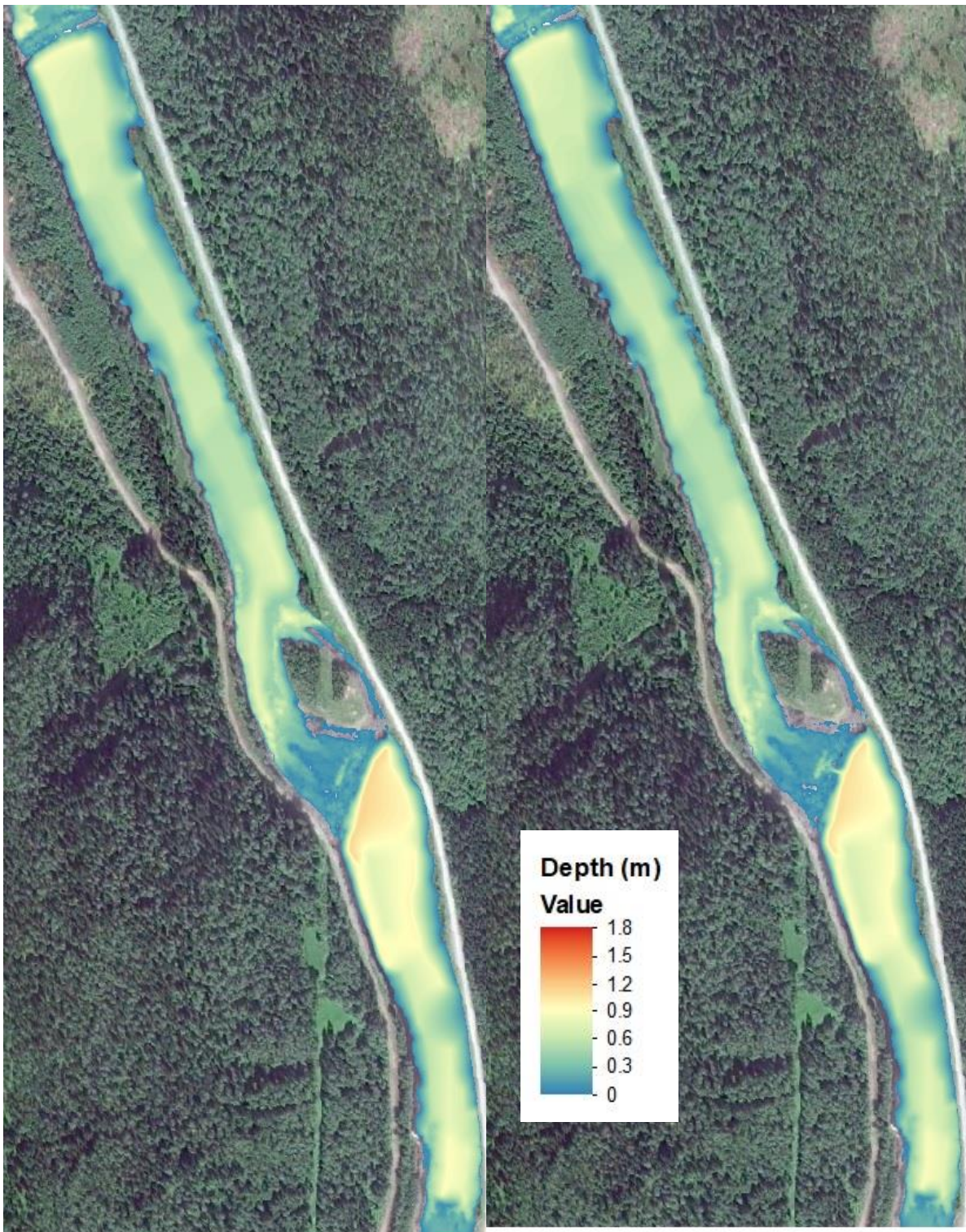


Figure 71: Simulation results as depth map for current (left) and after (right) for weir 23 and 24 at $10 \text{ m}^3/\text{s}$.

Q1.5



Figure 72: Simulation results as depth map for current (left) and after (right) for weir 21 and 22 at $1.5 \text{ m}^3/\text{s}$.

Q5

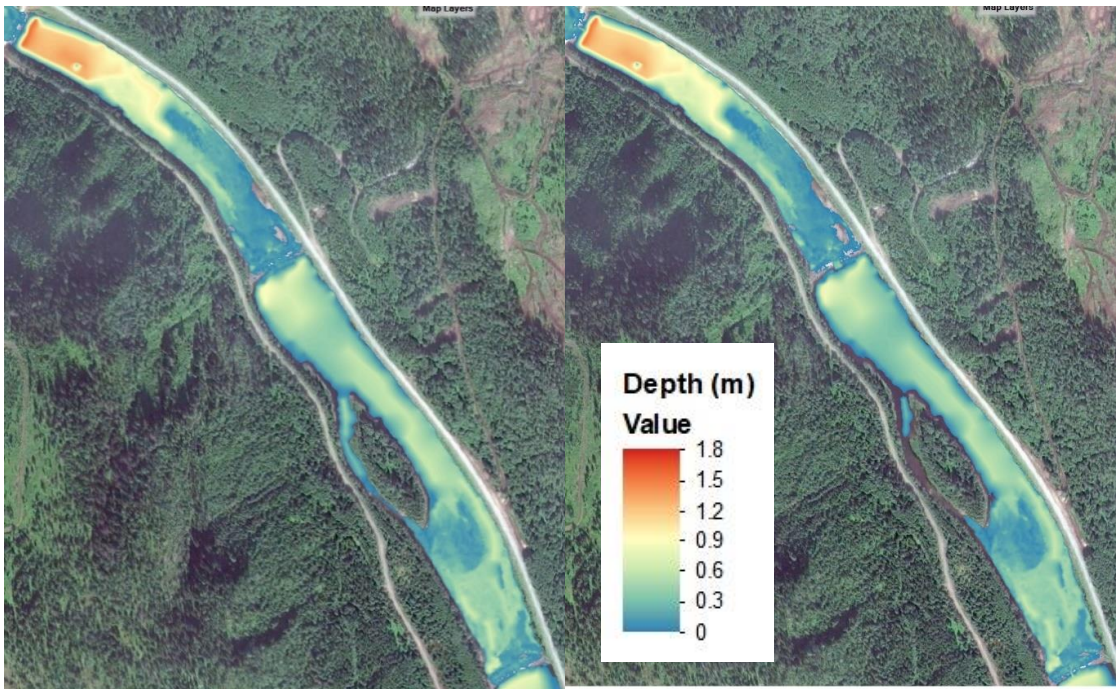


Figure 73: Simulation results as depth map for current (left) and after (right) for weir 21 and 22 at $5 \text{ m}^3/\text{s}$.

Q10

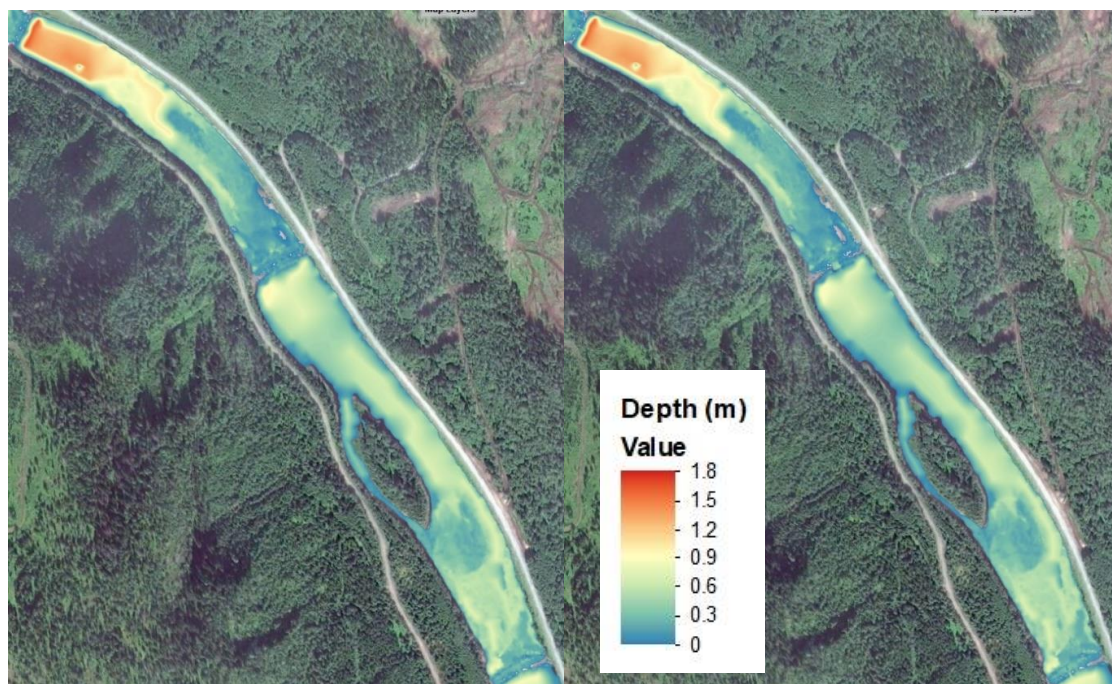


Figure 74: Simulation results as depth map for current (left) and after (right) for weir 21 and 22 at $10 \text{ m}^3/\text{s}$.

Q1.5

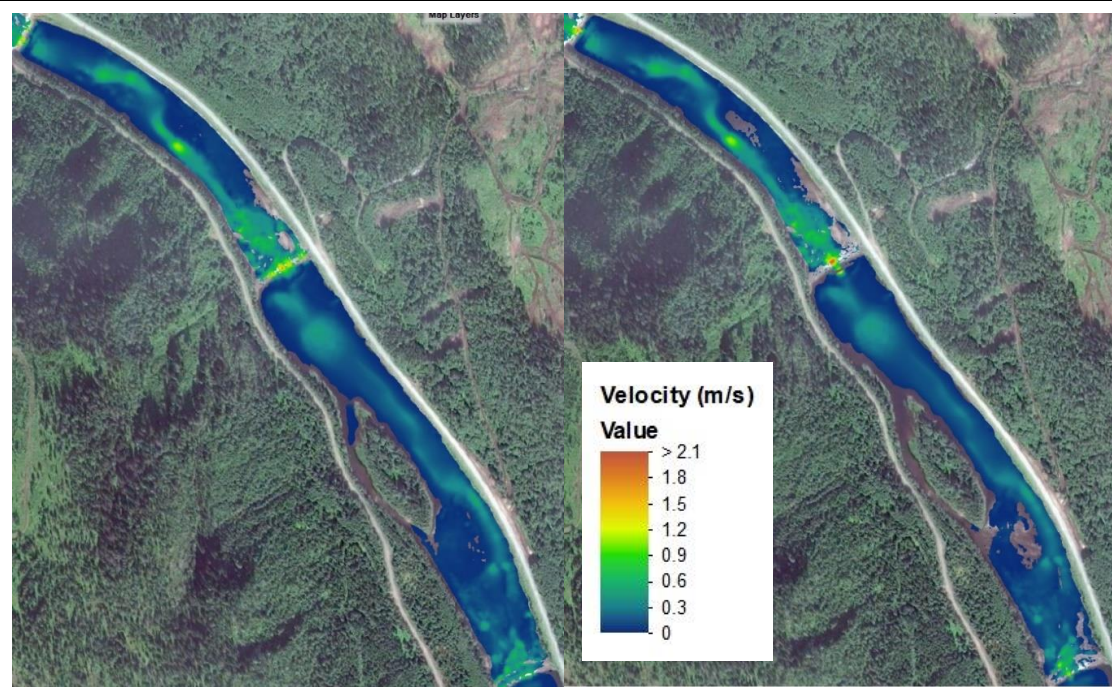


Figure 75: Simulation results as velocity map for current (left) and after (right) for weir 21 and 22 at $1.5 \text{ m}^3/\text{s}$.

Q5

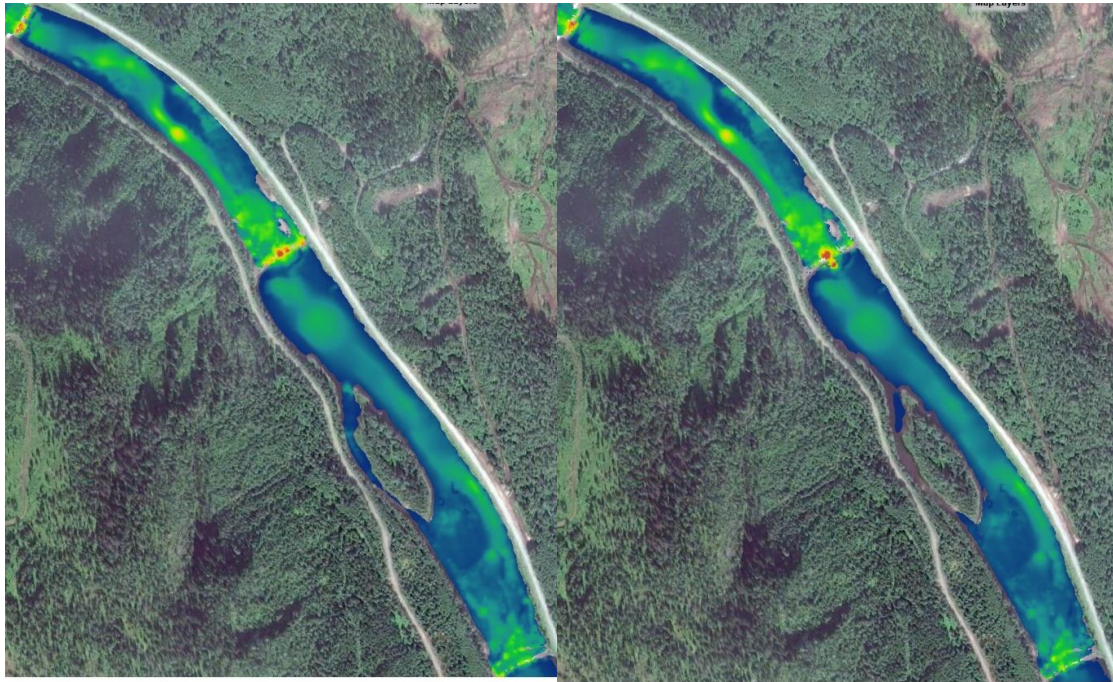


Figure 76: Simulation results as velocity map for current (left) and after (right) for weir 21 and 22 at $5 \text{ m}^3/\text{s}$.

Q10

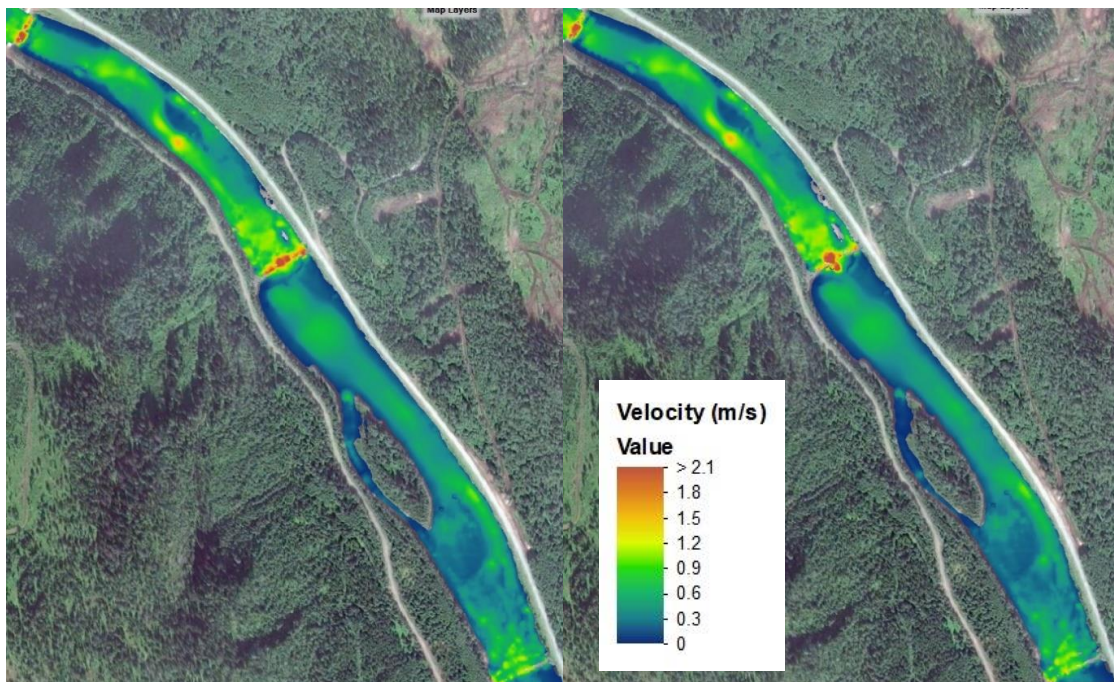


Figure 77: Simulation results as velocity map for current (left) and after measures (right) for weir 21 and 22 at $10 \text{ m}^3/\text{s}$.

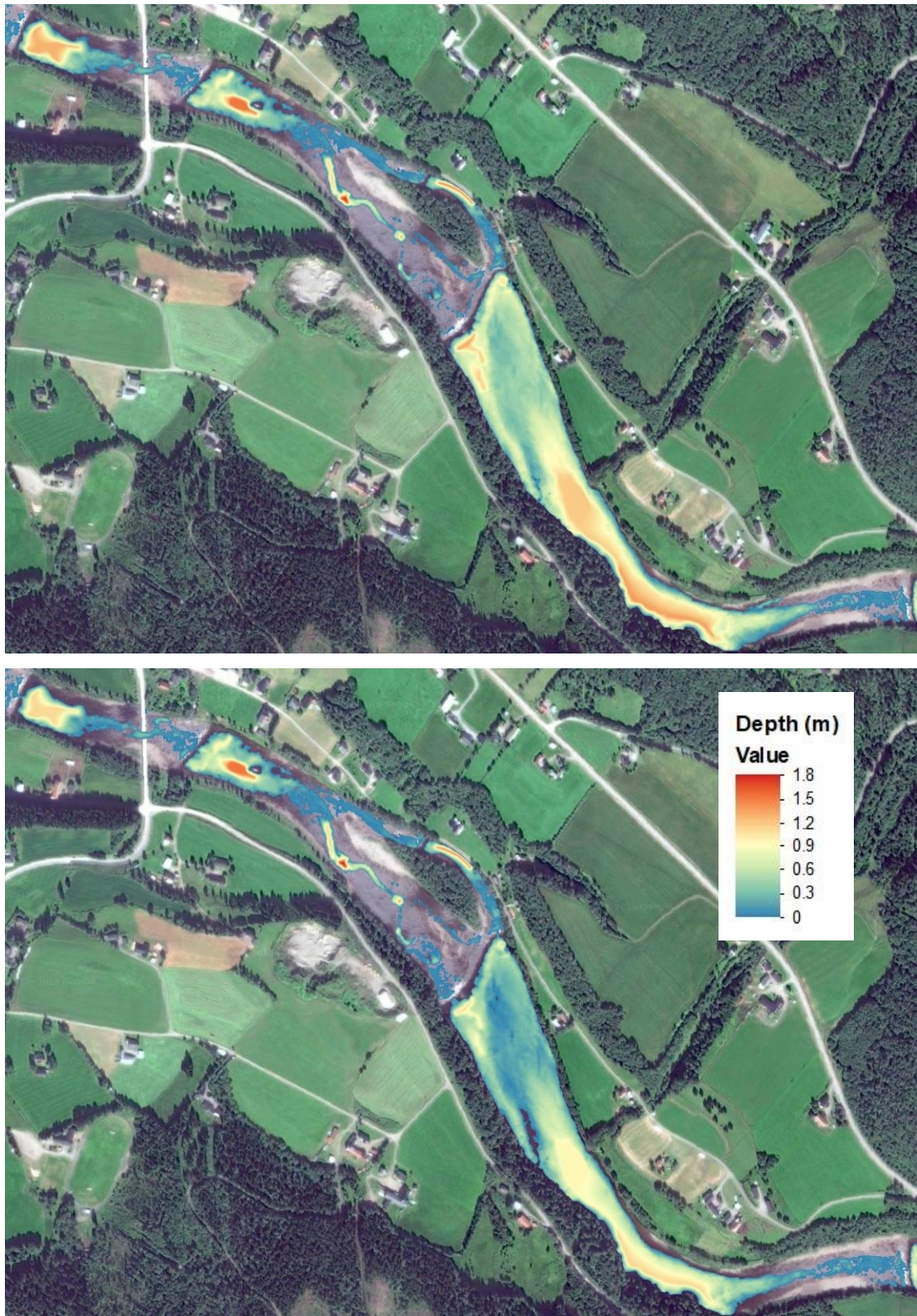


Figure 78: Simulation results as depth map for the current situation (top) and after measures (bottom) for weir 6 and 9 at 1.5 m³/s.

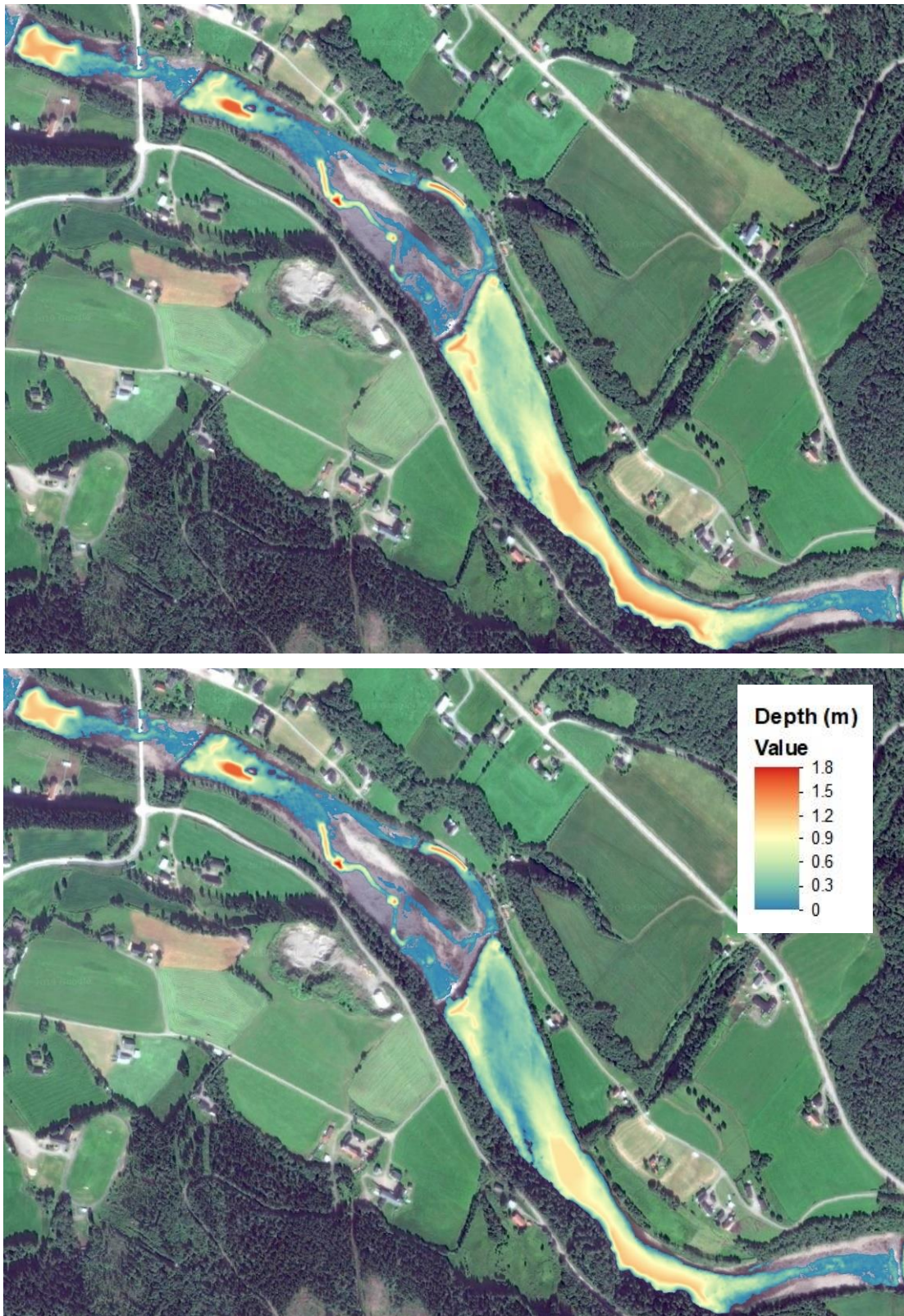


Figure 79: Simulation results as depth map for the current situation (top) and after measures (bottom) for weir 6 and 9 at 5 m³/s.

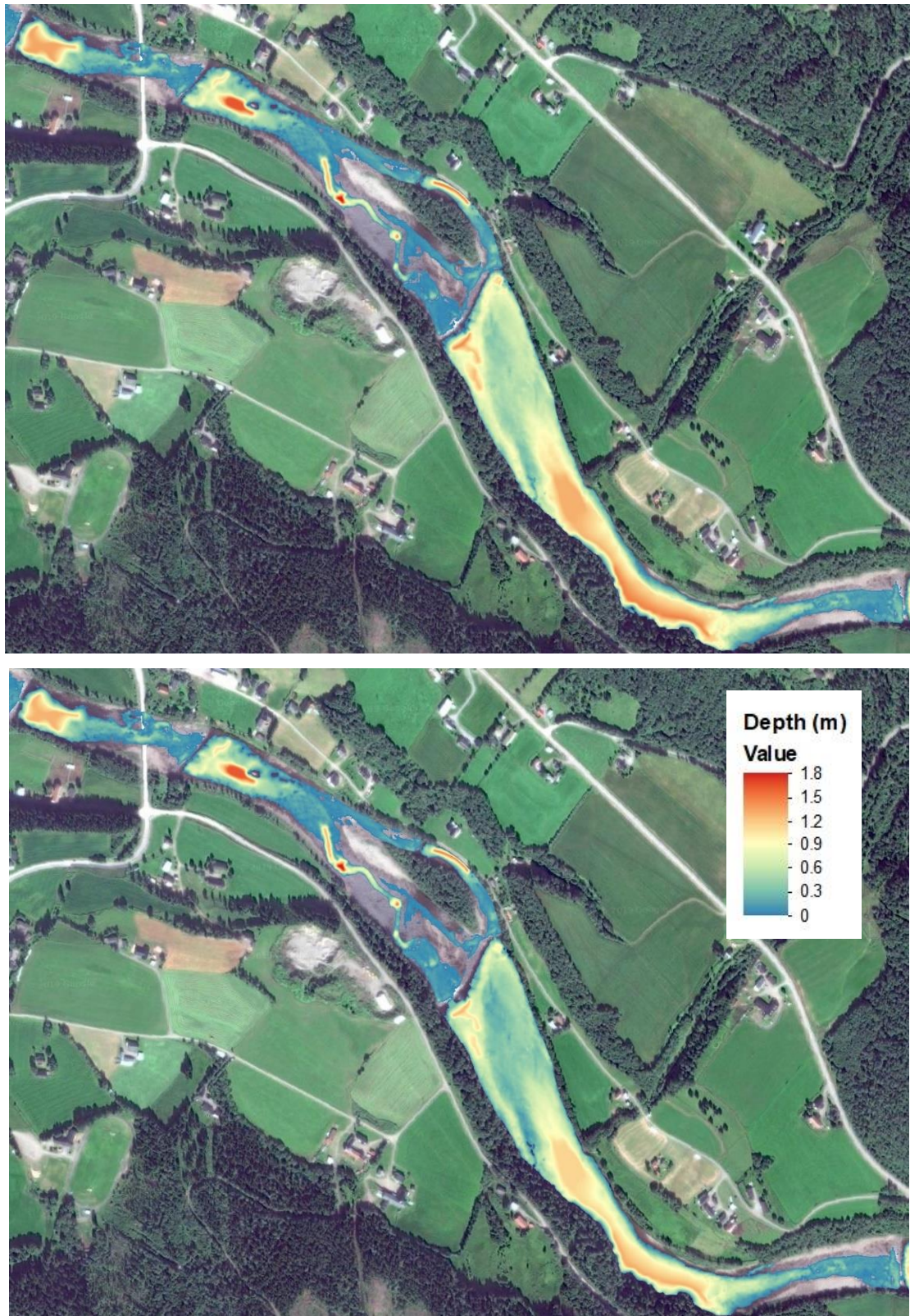


Figure 80: Simulation results as depth map for the current situation (top) and after measures (bottom) for weir 6 and 9 at $10 \text{ m}^3/\text{s}$.

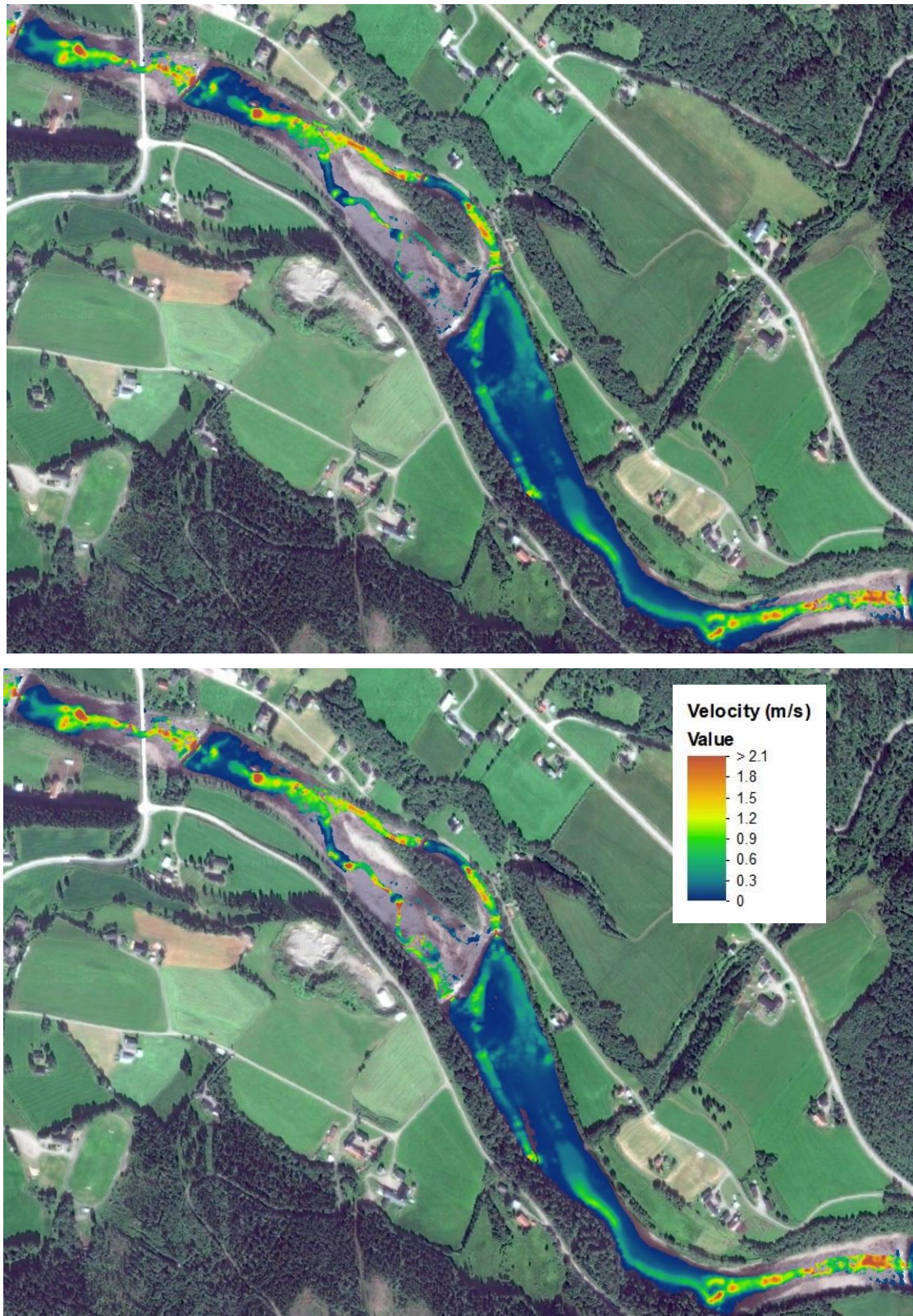


Figure 81: Simulation results as velocity map for the current situation (top) and after measures (bottom) for weir 6 and 9 at $1.5 \text{ m}^3/\text{s}$.

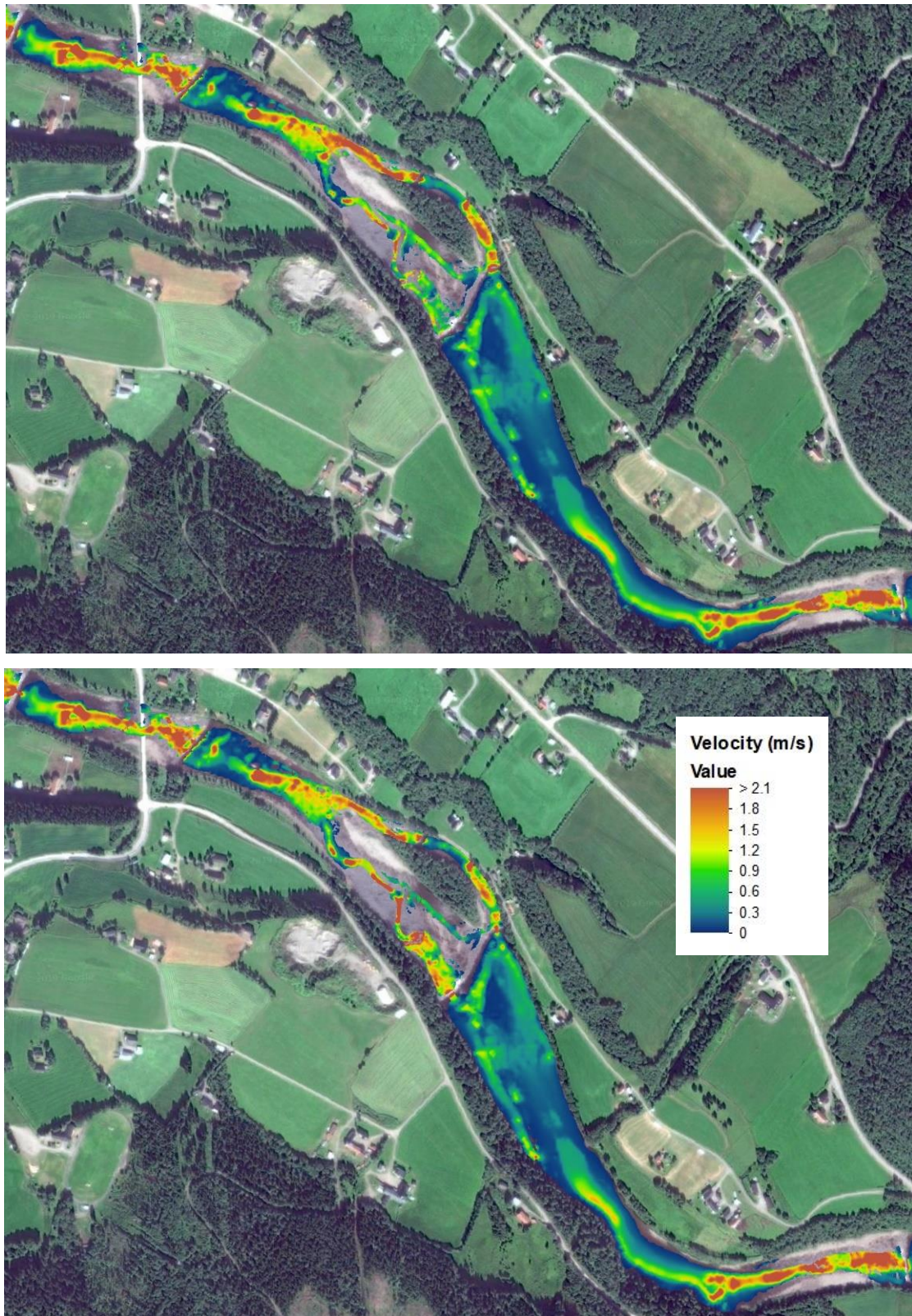


Figure 82: Simulation results as velocity map for the current situation (top) and after measures (bottom) for weir 6 and 9 at $5 \text{ m}^3/\text{s}$.

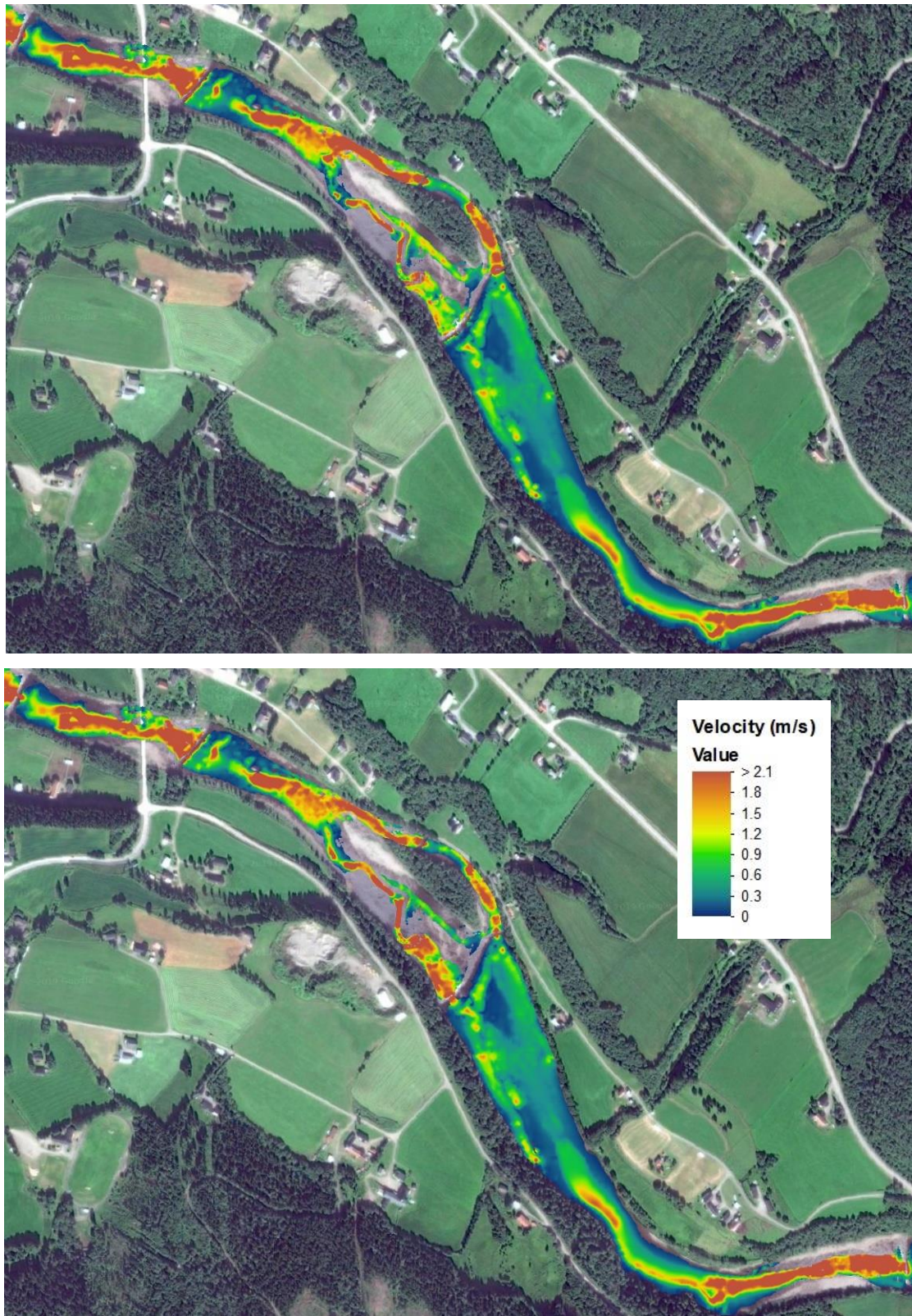


Figure 83: Simulation results as velocity map for the current situation (top) and after measures (bottom) for weir 6 and 9 at $10 \text{ m}^3/\text{s}$.

APPENDIX F - SIMULATION RESULTS (TABLE)

Velocity distributions

Q1	32				Q1	29			
	Current		After			Current		After	
0 - 0.05	14528	9	13339	9	0 - 0.05	47171	27	35772	23
0.05 - 0.1	33051	20	25735	17	0.05 - 0.1	23479	13	19372	13
0.1 - 0.2	41081	25	39171	25	0.1 - 0.2	39404	22	34618	22
0.2 - 0.3	36650	22	35908	23	0.2 - 0.3	28738	16	27438	18
0.3 - 0.4	19047	11	18512	12	0.3 - 0.4	15962	9	15772	10
0.3 - 0.5	7225	4	7014	5	0.3 - 0.5	7441	4	7411	5
0.5 - 0.8	10202	6	10428	7	0.5 - 0.8	9845	6	9817	6
> 0.8	5057	3	5454	4	> 0.8	4153	2	4237	3
Sum	166841	100	155561	100	Sum	176193	100	154437	100

Q1	28				Q1	27			
	Current		After			Current		After	
0 - 0.05	11042	10	5061	5	0 - 0.05	9527	10	4974	6
0.05 - 0.1	10872	10	13771	14	0.05 - 0.1	6649	7	4632	5
0.1 - 0.2	43894	39	47948	48	0.1 - 0.2	15966	17	16324	19
0.2 - 0.3	27113	24	20176	20	0.2 - 0.3	30313	32	28111	33
0.3 - 0.4	10451	9	6761	7	0.3 - 0.4	14913	16	15544	18
0.3 - 0.5	3570	3	2254	2	0.3 - 0.5	10863	11	10741	12
0.5 - 0.8	4164	4	2442	2	0.5 - 0.8	6100	6	5271	6
> 0.8	1466	1	1027	1	> 0.8	1130	1	708	1
Sum	112572	100	99440	100	Sum	95461	100	86305	100

Q1	24				Q1	23			
	Current		After			Current		After	
0 - 0.05	28383	21	17704	15	0 - 0.05	36727	17	23426	12
0.05 - 0.1	19631	15	17054	15	0.05 - 0.1	32291	15	32916	17
0.1 - 0.2	41244	31	38277	33	0.1 - 0.2	96662	45	110922	56
0.2 - 0.3	25291	19	24958	21	0.2 - 0.3	29676	14	15461	8
0.3 - 0.4	9032	7	9074	8	0.3 - 0.4	5004	2	3136	2
0.3 - 0.5	4419	3	3915	3	0.3 - 0.5	4044	2	1814	1
0.5 - 0.8	5781	4	5423	5	0.5 - 0.8	8841	4	7364	4
> 0.8	599	0	615	1	> 0.8	3045	1	2744	1
Sum	134380	100	117020	100	Sum	216290	100	197783	100

Q1	22				Q1	21			
	Current		After			Current		After	
0 - 0.05	66381	27	52407	25	0 - 0.05	27830	19	29718	22
0.05 - 0.1	48814	20	45559	21	0.05 - 0.1	28204	20	25827	19
0.1 - 0.2	71816	29	72621	34	0.1 - 0.2	28042	20	22849	17
0.2 - 0.3	37563	15	28658	13	0.2 - 0.3	19619	14	18950	14
0.3 - 0.4	16811	7	10537	5	0.3 - 0.4	17998	13	17196	13
0.3 - 0.5	3461	1	1809	1	0.3 - 0.5	10891	8	10008	7
0.5 - 0.8	2100	1	1709	1	0.5 - 0.8	9039	6	8298	6
> 0.8	79	0	423	0	> 0.8	1590	1	1449	1
Sum	247025	100	213723	100	Sum	143213	100	134295	100

Q1	9				Q1	6			
	Current		After			Current		After	
0 - 0.05	79988	32	63246	28	0 - 0.05	21296	17	19759	16
0.05 - 0.1	35041	14	35647	16	0.05 - 0.1	10981	9	9038	7
0.1 - 0.2	39809	16	38326	17	0.1 - 0.2	14218	11	10980	9
0.2 - 0.3	28153	11	27530	12	0.2 - 0.3	8661	7	9343	8
0.3 - 0.4	16161	7	15757	7	0.3 - 0.4	9152	7	7135	6
0.3 - 0.5	10870	4	10561	5	0.3 - 0.5	8010	6	7630	6
0.5 - 0.8	19021	8	18459	8	0.5 - 0.8	17787	14	19801	16
> 0.8	18625	8	18950	8	> 0.8	34485	28	36966	31
Sum	247668	100	228476	100	Sum	124590	100	120652	100

Q2	32				Q2	29			
	Current		After			Current		After	
0 - 0.05	2448	1	2965	2	0 - 0.05	33105	15	26005	13
0.05 - 0.1	7352	4	6686	4	0.05 - 0.1	24265	11	21824	11
0.1 - 0.2	33526	19	28602	16	0.1 - 0.2	37453	17	38309	19
0.2 - 0.3	28104	16	29753	17	0.2 - 0.3	31473	14	29886	14
0.3 - 0.4	20531	12	21251	12	0.3 - 0.4	24671	11	24242	12
0.3 - 0.5	30456	17	30535	18	0.3 - 0.5	24213	11	23922	12
0.5 - 0.8	37021	21	36775	21	0.5 - 0.8	28265	13	27932	14
> 0.8	16495	9	16835	10	> 0.8	14527	7	14497	7
Sum	175933	100	173402	100	Sum	217972	100	206617	100

Q2	28				Q2	27			
	Current		After			Current		After	
0 - 0.05	4797	4	882	1	0 - 0.05	4769	5	3210	3
0.05 - 0.1	6169	5	3907	4	0.05 - 0.1	4613	5	2687	3
0.1 - 0.2	15148	12	19635	18	0.1 - 0.2	6146	6	6947	7
0.2 - 0.3	20744	17	30119	27	0.2 - 0.3	6927	7	7032	7
0.3 - 0.4	42030	34	33318	30	0.3 - 0.4	12586	12	23410	24
0.3 - 0.5	13775	11	11602	10	0.3 - 0.5	22805	22	18782	20
0.5 - 0.8	13404	11	8022	7	0.5 - 0.8	35975	35	28215	29
> 0.8	6154	5	3700	3	> 0.8	7674	8	5707	6
Sum	122221	100	111185	100	Sum	101495	100	95990	100

Q2	24				Q2	23			
	Current		After			Current		After	
0 - 0.05	11981	8	9886	7	0 - 0.05	11511	5	9926	4
0.05 - 0.1	13120	9	13344	10	0.05 - 0.1	22485	9	22629	10
0.1 - 0.2	20100	14	18321	14	0.1 - 0.2	46647	19	63006	27
0.2 - 0.3	27741	20	25384	19	0.2 - 0.3	80643	33	93547	40
0.3 - 0.4	30239	21	29685	22	0.3 - 0.4	44653	18	20915	9
0.3 - 0.5	13979	10	15705	12	0.3 - 0.5	10726	4	5548	2
0.5 - 0.8	19196	14	17714	13	0.5 - 0.8	11927	5	7241	3
> 0.8	5441	4	5564	4	> 0.8	14942	6	12681	5
Sum	141797	100	135603	100	Sum	243534	100	235493	100

Q2	22				Q2	21			
	Current		After			Current		After	
0 - 0.05	16921	6	12746	5	0 - 0.05	8897	6	10767	7
0.05 - 0.1	25882	10	22975	9	0.05 - 0.1	11899	8	9672	6
0.1 - 0.2	71122	27	81562	33	0.1 - 0.2	22570	15	21108	14
0.2 - 0.3	66010	25	60225	24	0.2 - 0.3	25879	17	25982	17
0.3 - 0.4	45494	17	40034	16	0.3 - 0.4	22756	15	22710	15
0.3 - 0.5	25235	9	20048	8	0.3 - 0.5	16883	11	15776	10
0.5 - 0.8	14003	5	11147	4	0.5 - 0.8	37642	24	36154	24
> 0.8	2236	1	2102	1	> 0.8	8971	6	9166	6
Sum	266903	100	250839	100	Sum	155497	100	151335	100

Q2	9				Q2	6			
	Current		After			Current		After	
0 - 0.05	20829	8	11947	5	0 - 0.05	8020	5	6620	4
0.05 - 0.1	38857	15	29083	12	0.05 - 0.1	10047	6	8566	6
0.1 - 0.2	43392	16	46002	18	0.1 - 0.2	13575	9	13661	9
0.2 - 0.3	33282	13	35791	14	0.2 - 0.3	10221	6	8507	6
0.3 - 0.4	31942	12	28307	11	0.3 - 0.4	8990	6	7960	5
0.3 - 0.5	20506	8	22365	9	0.3 - 0.5	6493	4	7391	5
0.5 - 0.8	28541	11	28490	11	0.5 - 0.8	22703	14	18909	12
> 0.8	46816	18	47108	19	> 0.8	77226	49	80326	53
Sum	264165	100	249093	100	Sum	157275	100	151940	100

Q3	32				Q3	29			
	Current		After			Current		After	
0 - 0.1	3218	2	2034	1	0 - 0.1	31459	14	30690	14
0.1 - 0.3	32935	18	32105	18	0.1 - 0.3	71437	31	70875	31
0.3 - 0.5	43830	24	44741	25	0.3 - 0.5	47951	21	47147	21
0.5 - 0.8	63970	36	64258	36	0.5 - 0.8	50678	22	50322	22
0.8 - 1	15827	9	15597	9	0.8 - 1	11532	5	11437	5
> 1	19872	11	19824	11	> 1	16664	7	16525	7
Sum	179652	100	178559	100	Sum	229721	100	226996	100

Q3	28				Q3	27			
	Current		After			Current		After	
0 - 0.1	7202	6	4292	4	0 - 0.1	6569	6	4040	4
0.1 - 0.3	20164	16	21364	18	0.1 - 0.3	9157	9	11361	11
0.3 - 0.5	49144	39	48801	41	0.3 - 0.5	10677	10	13052	13
0.5 - 0.8	40052	32	35496	30	0.5 - 0.8	51994	50	55368	54
0.8 - 1	3981	3	3942	3	0.8 - 1	16749	16	11335	11
> 1	6488	5	4942	4	> 1	9607	9	6556	6
Sum	127031	100	118837	100	Sum	104753	100	101712	100

Q3	24				Q3	23			
	Current		After			Current		After	
0 - 0.1	13783	9	13154	9	0 - 0.1	17509	7	19617	8
0.1 - 0.3	30303	21	30048	21	0.1 - 0.3	74594	29	87263	34
0.3 - 0.5	52126	36	50129	35	0.3 - 0.5	117902	46	111742	44
0.5 - 0.8	33503	23	34172	24	0.5 - 0.8	24089	9	15982	6
0.8 - 1	10410	7	9878	7	0.8 - 1	6171	2	4250	2
> 1	5997	4	5892	4	> 1	18554	7	16154	6
Sum	146122	100	143273	100	Sum	258819	100	255008	100

Q3	22				Q3	21			
	Current		After			Current		After	
0 - 0.1	14725	5	20138	7	0 - 0.1	10760	7	9405	6
0.1 - 0.3	98725	36	96496	36	0.1 - 0.3	27106	17	27749	18
0.3 - 0.5	104081	38	103710	39	0.3 - 0.5	43325	27	41686	26
0.5 - 0.8	49811	18	42219	16	0.5 - 0.8	52728	33	52424	33
0.8 - 1	3951	1	4171	2	0.8 - 1	16527	10	16797	11
> 1	2585	1	2417	1	> 1	9931	6	9714	6
Sum	273878	100	269151	100	Sum	160377	100	157775	100

Q3	9				Q3	6			
	Current		After			Current		After	
0 - 0.1	18304	7	19553	8	0 - 0.1	8448	5	9274	5
0.1 - 0.3	76221	28	63713	25	0.1 - 0.3	23965	13	23494	14
0.3 - 0.5	63245	23	63907	25	0.3 - 0.5	15502	9	14073	8
0.5 - 0.8	45708	17	44098	17	0.5 - 0.8	23246	13	20202	12
0.8 - 1	13881	5	13798	5	0.8 - 1	14954	8	13187	8
> 1	55304	20	54741	21	> 1	93833	52	92590	54
Sum	272663	100	259810	100	Sum	179948	100	172820	100

Depth distributions

Q1	32				Q1	29			
	Current		After			Current		After	
0 - 0.05	11515	7	20324	13	0 - 0.05	18319	10	19375	12
0.05 - 0.1	20085	12	20708	13	0.05 - 0.1	29502	16	28049	17
0.1 - 0.2	47281	28	45522	29	0.1 - 0.2	46279	25	44693	27
0.2 - 0.3	39961	24	33133	21	0.2 - 0.3	26097	14	22284	13
0.3 - 0.5	38143	23	33563	22	0.3 - 0.5	26777	14	22544	14
> 0.5	9803	6	2189	1	> 0.5	39888	21	28611	17
Sum	166788	100	155439	100	Sum	186862	100	165556	100

Q1	28				Q1	27			
	Current		After			Current		After	
0 - 0.05	11692	10	10444	10	0 - 0.05	5791	6	8468	10
0.05 - 0.1	13700	12	13572	14	0.05 - 0.1	11645	12	12716	15
0.1 - 0.2	30152	27	31388	31	0.1 - 0.2	18127	19	18959	22
0.2 - 0.3	10287	9	21513	22	0.2 - 0.3	7171	7	13507	16
0.3 - 0.5	11013	10	20793	21	0.3 - 0.5	19667	20	22652	26
> 0.5	36871	32	1961	2	> 0.5	34556	36	10133	12
Sum	113715	100	99671	100	Sum	96957	100	86435	100

Q1	24				Q1	23			
	Current		After			Current		After	
0 - 0.05	5754	4	6356	5	0 - 0.05	22900	11	19177	10
0.05 - 0.1	3446	3	4432	4	0.05 - 0.1	25994	12	23764	12
0.1 - 0.2	8783	6	12644	11	0.1 - 0.2	35541	16	40310	20
0.2 - 0.3	12953	10	16533	14	0.2 - 0.3	47102	22	53736	27
0.3 - 0.5	25025	18	37479	32	0.3 - 0.5	56577	26	53727	27
> 0.5	79575	59	40302	34	> 0.5	27780	13	9807	5
Sum	135536	100	117746	100	Sum	215894	100	200521	100

Q1	22				Q1	21			
	Current		After			Current		After	
0 - 0.05	24061	10	18828	9	0 - 0.05	16431	11	17423	13
0.05 - 0.1	17702	7	12854	6	0.05 - 0.1	18725	13	15701	12
0.1 - 0.2	30942	12	31195	14	0.1 - 0.2	15968	11	13751	10
0.2 - 0.3	40032	16	66095	31	0.2 - 0.3	10326	7	11942	9
0.3 - 0.5	101692	41	75762	35	0.3 - 0.5	20697	14	16620	12
> 0.5	33299	13	11117	5	> 0.5	60893	43	57804	43
Sum	247728	100	215851	100	Sum	143040	100	133241	100

Q1	9				Q1	6			
	Current		After			Current		After	
0 - 0.05	7749	3	14443	6	0 - 0.05	23608	19	25613	22
0.05 - 0.1	9026	4	18671	8	0.05 - 0.1	15469	13	15249	13
0.1 - 0.2	11570	5	36437	16	0.1 - 0.2	18136	15	16508	14
0.2 - 0.3	14225	6	32185	14	0.2 - 0.3	12502	10	12382	10
0.3 - 0.5	58843	23	44793	19	0.3 - 0.5	17026	14	15098	13
> 0.5	151698	60	86452	37	> 0.5	35813	29	33690	28
Sum	253111	100	232981	100	Sum	122554	100	118540	100

Q2	32				Q2	29			
	Current		After			Current		After	
0 - 0.1	7731	4	17583	10	0 - 0.1	41448	19	37928	18
0.1 - 0.2	31569	18	38524	22	0.1 - 0.2	54539	25	57229	28
0.2 - 0.3	46113	26	42561	25	0.2 - 0.3	40907	19	35084	17
0.3 - 0.4	39190	22	34357	20	0.3 - 0.4	20144	9	22842	11
0.4 - 0.5	31445	18	25258	15	0.4 - 0.5	14023	6	12129	6
> 0.5	19635	11	15015	9	> 0.5	48220	22	42284	20
Sum	175683	100	173298	100	Sum	219281	100	207496	100

Q2	28				Q2	27			
	Current		After			Current		After	
0 - 0.1	18131	15	16453	15	0 - 0.1	7972	8	10555	11
0.1 - 0.2	24014	20	23043	21	0.1 - 0.2	19936	20	22173	23
0.2 - 0.3	25107	21	27264	25	0.2 - 0.3	15572	15	14236	15
0.3 - 0.4	8662	7	18074	16	0.3 - 0.4	7702	8	13081	14
0.4 - 0.5	6943	6	18462	17	0.4 - 0.5	6380	6	5626	6
> 0.5	39197	32	7781	7	> 0.5	44353	44	30857	32
Sum	122054	100	111077	100	Sum	101915	100	96528	100

Q2	24				Q2	23			
	Current		After			Current		After	
0 - 0.1	8879	6	9440	7	0 - 0.1	28922	12	26783	11
0.1 - 0.2	9833	7	9378	7	0.1 - 0.2	26602	11	25736	11
0.2 - 0.3	9499	7	10204	8	0.2 - 0.3	35886	15	36415	15
0.3 - 0.4	10701	8	11457	8	0.3 - 0.4	42488	17	44419	19
0.4 - 0.5	13011	9	15002	11	0.4 - 0.5	54427	22	58045	24
> 0.5	89595	63	80049	59	> 0.5	55039	23	45718	19
Sum	141518	100	135530	100	Sum	243364	100	237116	100

Q2	22				Q2	21			
	Current		After			Current		After	
0 - 0.1	20290	8	28733	11	0 - 0.1	22588	15	22583	15
0.1 - 0.2	43259	16	35826	14	0.1 - 0.2	27476	18	29123	19
0.2 - 0.3	29890	11	32372	13	0.2 - 0.3	14237	9	12236	8
0.3 - 0.4	40317	15	59138	23	0.3 - 0.4	11526	7	12948	9
0.4 - 0.5	65133	24	55236	22	0.4 - 0.5	11271	7	10547	7
> 0.5	67777	25	41236	16	> 0.5	67167	44	63404	42
Sum	266666	100	252541	100	Sum	154265	100	150841	100

Q2	9				Q2	6			
	Current		After			Current		After	
0 - 0.1	17981	7	20377	8	0 - 0.1	52817	34	50172	34
0.1 - 0.2	13659	5	22342	9	0.1 - 0.2	25871	17	26799	18
0.2 - 0.3	12052	5	36420	15	0.2 - 0.3	15569	10	14819	10
0.3 - 0.4	17613	7	38646	16	0.3 - 0.4	11413	7	10887	7
0.4 - 0.5	40598	15	22314	9	0.4 - 0.5	9070	6	8592	6
> 0.5	162584	61	109210	44	> 0.5	39125	25	37802	25
Sum	264487	100	249309	100	Sum	153865	100	149071	100

Q3	32				Q3	29			
	Current		After			Current		After	
0 - 0.1	4021	2	5525	3	0 - 0.1	23905	10	29244	13
0.1 - 0.2	11215	6	19680	11	0.1 - 0.2	35902	16	35726	16
0.2 - 0.3	33981	19	36378	20	0.2 - 0.3	54986	24	57455	25
0.3 - 0.4	41826	23	39774	22	0.3 - 0.4	36617	16	34834	15
0.4 - 0.5	39137	22	35321	20	0.4 - 0.5	20059	9	16827	7
> 0.5	49408	28	41843	23	> 0.5	57689	25	53115	23
Sum	179588	100	178521	100	Sum	229158	100	227201	100

Q3	28				Q3	27			
	Current		After			Current		After	
0 - 0.1	12618	6	12312	10	0 - 0.1	5183	5	6019	6
0.1 - 0.2	19249	8	18541	16	0.1 - 0.2	10581	10	13166	13
0.2 - 0.3	23135	10	22200	19	0.2 - 0.3	21385	20	21394	21
0.3 - 0.4	21558	9	23200	20	0.3 - 0.4	12405	12	10768	11
0.4 - 0.5	7098	3	13911	12	0.4 - 0.5	6880	7	8096	8
> 0.5	43276	19	28775	24	> 0.5	48306	46	42466	42
Sum	227201	56	118939	100	Sum	104740	100	101909	100

Q3	24				Q3	23			
	Current		After			Current		After	
0 - 0.1	7653	5	8335	6	0 - 0.1	23420	9	23000	9
0.1 - 0.2	9586	7	9562	7	0.1 - 0.2	20833	8	20032	8
0.2 - 0.3	9072	6	9219	6	0.2 - 0.3	19465	8	19305	8
0.3 - 0.4	9683	7	10505	7	0.3 - 0.4	25012	10	26550	10
0.4 - 0.5	11645	8	11622	8	0.4 - 0.5	38243	15	37298	15
> 0.5	98274	67	94091	66	> 0.5	131627	51	129117	51
Sum	145913	100	143334	100	Sum	258600	100	255302	100

Q3	22				Q3	21			
	Current		After			Current		After	
0 - 0.1	10487	4	14683	5	0 - 0.1	11206	7	10935	7
0.1 - 0.2	22426	8	26563	10	0.1 - 0.2	25487	16	24715	16
0.2 - 0.3	41779	15	39728	15	0.2 - 0.3	24102	15	25782	16
0.3 - 0.4	30759	11	37721	14	0.3 - 0.4	11800	7	11926	8
0.4 - 0.5	46560	17	50649	19	0.4 - 0.5	13448	8	13568	9
> 0.5	121617	44	99720	37	> 0.5	73881	46	70355	45
Sum	273628	100	269064	100	Sum	159924	100	157281	100

Q3	9				Q3	6			
	Current		After			Current		After	
0 - 0.1	15959	6	17325	7	0 - 0.1	54254	31	51785	31
0.1 - 0.2	18174	7	20171	8	0.1 - 0.2	36582	21	36079	21
0.2 - 0.3	12563	5	23669	9	0.2 - 0.3	19406	11	17846	11
0.3 - 0.4	14798	5	34965	13	0.3 - 0.4	13705	8	12133	7
0.4 - 0.5	25792	9	35236	14	0.4 - 0.5	10057	6	10006	6
> 0.5	185254	68	127781	49	> 0.5	42372	24	41855	25
Sum	272540	100	259147	100	Sum	176376	100	169704	100

APPENDIX H – CROSS-SECTION PROFILES

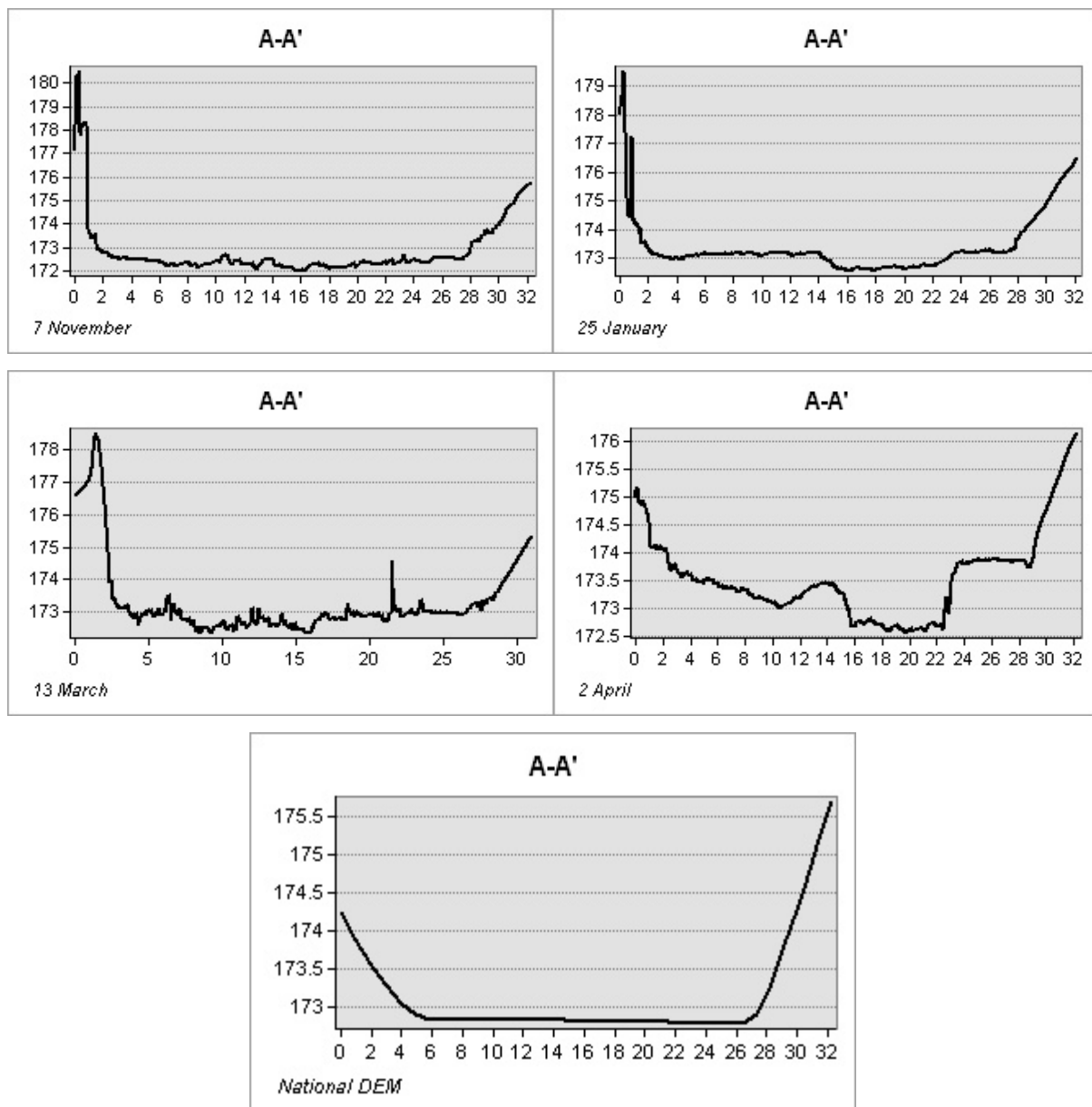


Figure 84: Profile graphs for cross-section A-A' extracted from Sokna DEMs and reference DTM, showing elevation and distance from left bank.

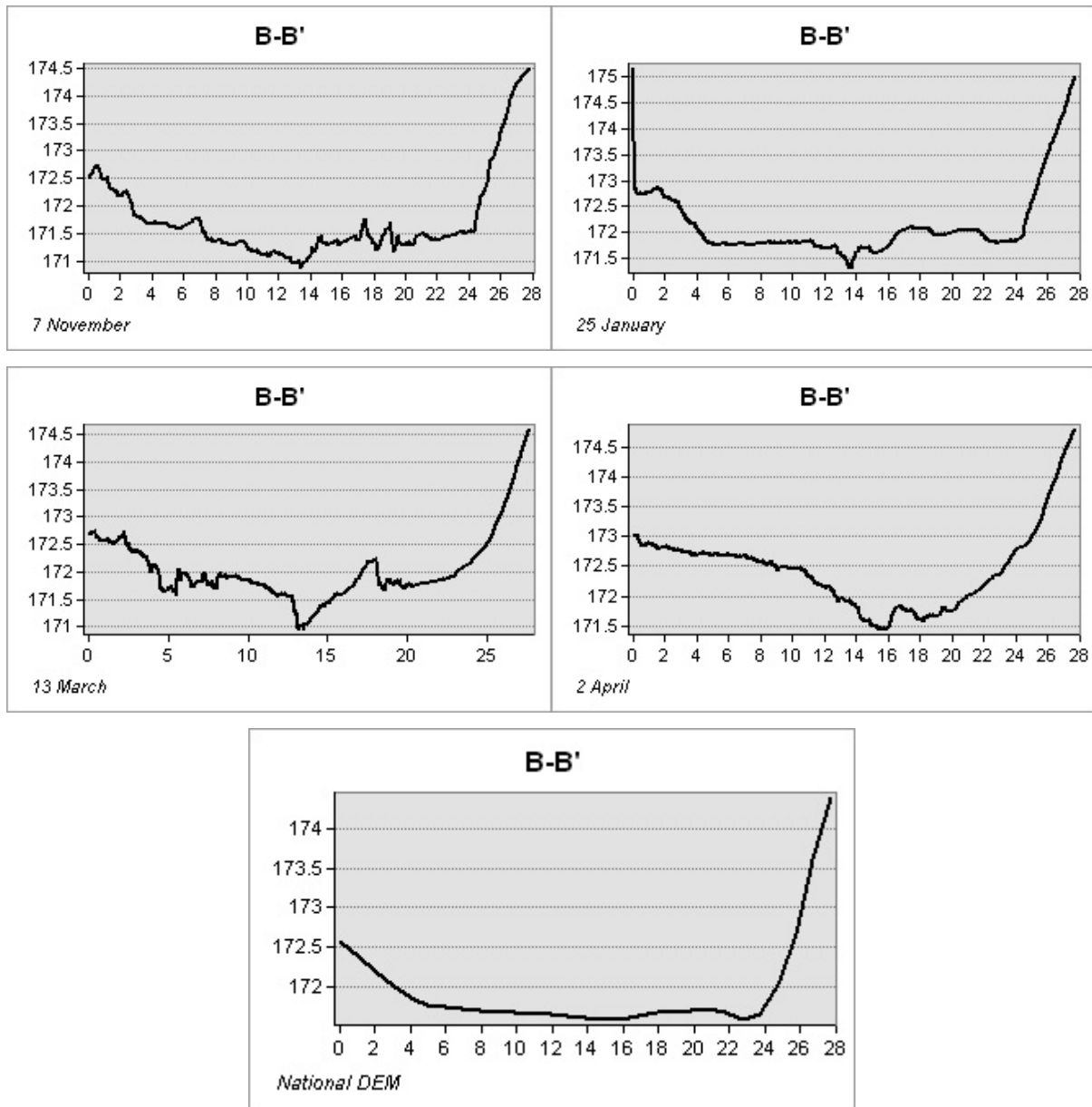


Figure 85: Profile graphs for cross-section B-B' extracted from Sokna DEMs and reference DTM, showing elevation and distance from left bank.

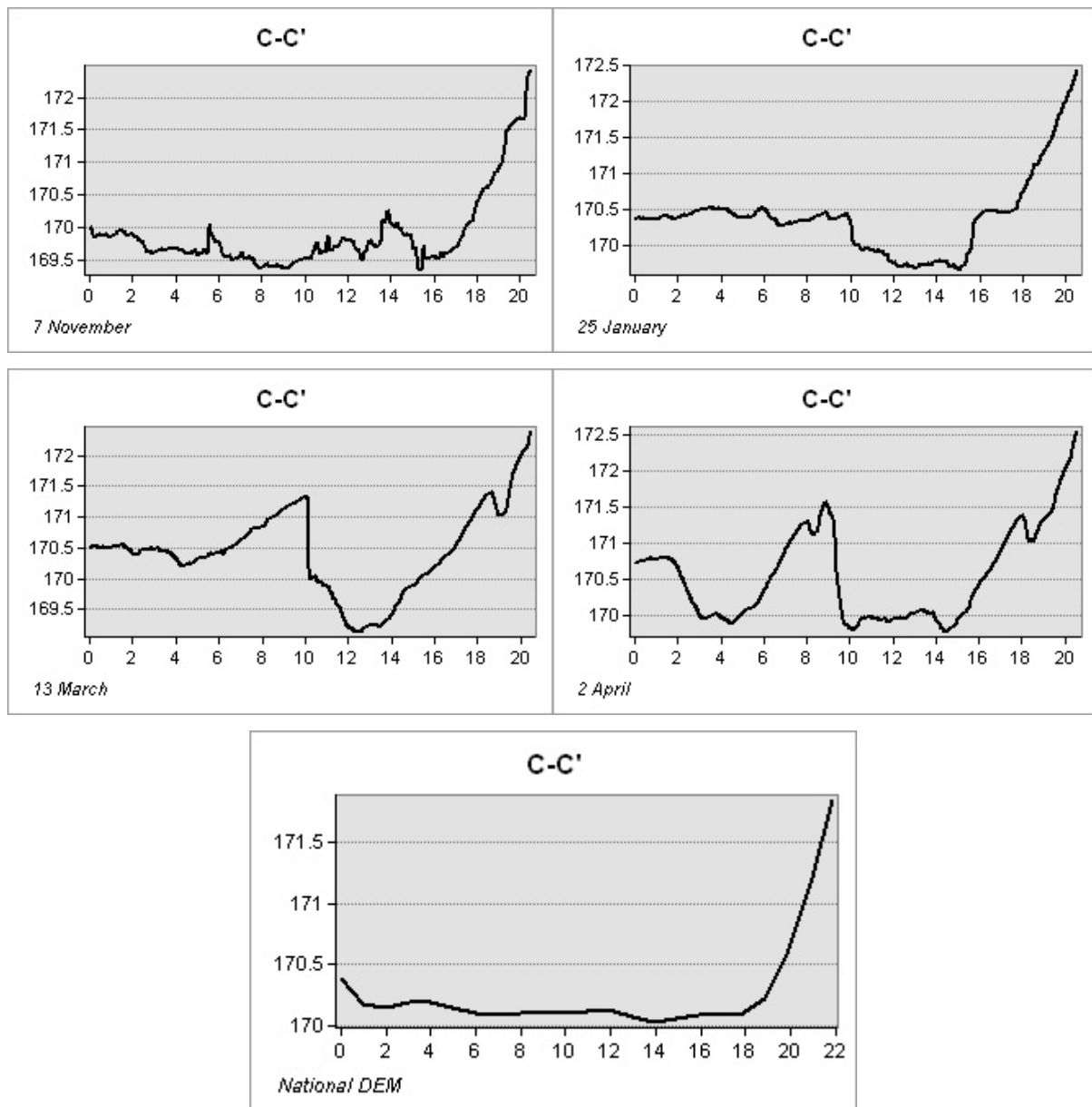


Figure 86: Profile graphs for cross-section C-C' extracted from Sokna DEMs and reference DTM, showing elevation and distance from left bank.

APPENDIX H - File structure in attachment folder

	ArcGIS	
		Boundaries
		Artificial Channel – Polygon boundary for clipping DEM/ortho
		Sokna – Polygon boundary for clipping DEM/ortho
		Weirs – Polygon boundary for clipping results map for each weir
		Coverage – Channel area boundary for extracting LAS points and results file
		Elvekant 2018 – Polylines and polygon of river boundary supplied by Terratec
		GCP – Control points in Nea
		HEC-RAS_Results
		Depth – Clipped result rasters for depth and water-covered area calculation
		Velocity – Clipped result rasters for velocity
		Raster – DEM created from LAS datasets
		River Ice
		MinusRasters – Minus raster for Sokna
		Profiles – Extracted profiles from cross-sections in Sokna DEMs
		Terrain_mod
		Breaklines – Breaklines used as surface constraints when creating DEM
		Extract LAS – Extracted LAS points for editing terrain on each weir
		Vertical_Accuracy – Shapefile with check points and extracted LiDAR elevations
	Drone	
		Agisoft PhotoScan
		Nea – DEM, orthomosaic and GCPs
		Høydedata
		data – Høydedata DTM model
		metadata – Høydedata clip boundary (shapefile)
		Images – Contains images from the UAV survey in Nea on 11 September
		Sokna
		0204 Sokna - DEM, orthomosaic and GCPs
		Images - Contains images from the UAV survey on 2 April
		0711 Sokna - DEM, orthomosaic and GCPs

			Images - Contains images from the UAV survey on 7 November
			1303 Sokna - DEM, orthomosaic and GCPs
			Images - Contains images from the UAV survey on 13 March
			2501 Sokna - DEM, orthomosaic and GCPs
			Images - Contains images from the UAV survey 25 January
			Høydedata
			data - Høydedata DTM model
			metadata - Høydedata clip boundary (shapefile)
			HEC-RAS
			Geometry – River geometries (1D polylines and 2D flow area) and break lines
			Manning's_n_Regions – Base n values (shapefile) and Manning's regions raster
			Map_Results – Result maps (depth and velocity) for simulations in Nea
			Project – Project files from hydraulic modelling
			Terrain
			LiDAR_water_surface – Water surface from LiDAR data
			Terrain – Terrain model used in simulations for 'current situation'
			Terrain_with_measures – Terrain with modification for 'after measures'
			UAV – Terrain from UAV survey data
			Weirs – Shapefile containing proposed measures from 'Sweco tiltaksplan'

